Dynamics of quantum materials at the nanoscale

Aaron J. Sternbach

Submitted in partial fulfilment of the
requirements for the degree of
Doctor of Philosophy
in the Graduate School of Arts and Sciences

COLUMBIA UNIVERSITY

2020

© 2020

Aaron J. Sternbach

All Rights Reserved

Abstract

Dynamics of quantum materials at the nanoscale

Aaron J. Sternbach

Programing the properties of quantum materials on demand is a central goal of condensed matter physics with the potential to usher in a new technological era. Photoexcitation has proven to be an exceptionally capable means of resonant and non-resonant control over matter offering coveted routes to selectively control the electronic, lattice, interband or valley optical and excitonic properties of quantum materials. One major limitation of probing the rich class of phenomena enabled by photoexcitation is the diffraction limit. The properties of quantum materials are often sensitive to the microscopic details of the environment at phase transition boundaries: which naturally leads drastic inhomogeneity at the nanoscale. In other cases, the media may transiently support high-momentum "nano-light" or host topologically protected conductive channels that are localized to one-dimensional physical edges. All of these phenomena demand a probe with the spatial resolution that is commensurate with the emergent behavior.

To address these demands the author contributed to the development of time-resolved scattering near-field optical microscopy (Tr-SNOM). Utilizing the principles developed as part of this thesis amplified laser technology was combined with a commercial near-field optical microscope to produce a state-of-the-art time-resolved nanoscope. The custom apparatus operates with twenty nanometer spatial resolution with unprecedented spectral coverage spanning visible to mid-infrared all with (30-300) femtosecond temporal resolution. The experimental apparatus was, first, applied to investigate the photo-induced insulator-to-metal transition in Vanadium Dioxide. We observe nanoscale inhomogeneity of the transient conductivity. Our data reveals that

local nanoscopic variations of the strain exist in our particular VO_2 thin film at equilibrium. Regions of compressive strain are, furthermore, found to correlate with regions where a high degree of transient conductivity is attained. Our systematic study of the local fluence dependence and dynamics reveal that the fluence threshold, F_c, for the monoclinic-insulator to rutile-metal transition is inhomogeneous in real-space. A second growth process is identified, even at excitations fluences well below F_c, which operates on a longer timescale with an inhomogeneous rise time, τ^{-1}. Together F_c and τ^{-1} govern the inhomogeneous nano-texturing of the transient conductivity. Secondly, we uncover that crystals of van-der Waals (vdW) semiconductors behave as optical waveguides with broadly tunable properties at femto-second time scales. We detect giant optical phase shifts of waveguided photons under strong photo-excitation devoid of any unwanted added losses in the vdW crystal, WSe_2. Our results firmly implicate bound excitons in the observed behavior. Our transient spatio-temporal maps reveal two concomitant effects: i) photo-generation of electron-hole plasma that drives the WSe_2 crystal towards a Mott transition where excitons dissociate and ii) a coherent interaction between the waveguide material and pump light, known as the optical Stark effect, that alters the phase velocity of guided photons on the femtosecond timescale.

Table of Contents

List of Figures

List of Tables

Acknowledgments

I would first like to acknowledge Professor Dmitri N. Basov for fearless leadership as well as generous, unwavering, support. His guidance was pivotal in overcoming numerous challenging obstacles during the development of this thesis. All material presented herein, furthermore, greatly benefited from his role as an educator on the development and communication of scientific discoveries and ideas. His careful and constructive comments were consistently thoughtful, directly helpful and also delivered on ultrafast timescales. His contributions to this thesis work are so great that the outcome without his role is, frankly, unimaginable.

It is a pleasure to give thanks to Professor Richard D. Averitt. As a collaborator, he directly supported the first tests we conducted of coupling amplified laser technology to near-field microscopes. As a mentor, educator and scientific leader I am indebted to him and grateful for having the opportunity to work with him.

I am appreciative of all that I've learnt from many incredible graduate students and early career scientists throughout my pHD. Within this inexhaustive list I would like to sincerely thank Professor Mengkun Liu for his role as a mentor and collaborator. I am grateful to Dr. Martin Wagner for paving the way toward time-resolved near-field optics. Dr. Wagner developed and provided the first pioneering demonstrations using Tr-SNOM and generously passed on his valuable insight. Conversations with Dr. James Hinton were critically important to understand and overcome background artifacts in Tr-SNOM measurements. Dr. Peter Kissin provided invaluable assistance in coupling amplified laser technologies to near-field microscopes. I am, furthermore, grateful to past and present members of the Basov group for creating a wonderful and intellectually stimulating atmosphere.

I am grateful to my family for their support throughout this period of my life. My father and mother, Robert Sternbach and Jayne Rygh, as well as my sister and brother in-law, Rebekah and Ben Rubenstein, have given me essential support in many ways throughout the doctoral processes. I am tremendously thankful to be blessed with such a wonderful family.

Finally, I would like to express my gratitude to my girlfriend, Carina Taveras, for providing a bedrock of support, partnership and friendship. Time and again her strength of character, generosity and love have allowed us to harvest renewing moments. From San Diego to New York our relationship has deepened my heart giving new meaning to the work in this thesis and to our lives in general. I am forever grateful.

Chapter 1: Artifact free time-resolved near-field optical microscopy

1.1 Introduction

Ultrafast optical techniques provide access to processes that occur with awesome rapidity, enabling novel routes to control and interrogate the complex energy landscapes of materials at the focus of modern condensed matter physics (*1, 2*). Ultrafast techniques have provided insights into coherent motions at atomic length scales (*3*), excitation or interrogation of selective electronic, lattice, spin or magnetic modes (*4-6*), and domain growth (*7*). In materials where multiple degrees of freedom compete ultrafast studies have allowed researchers to identify the degrees of freedom associated with emergent phenomena (*8-10*). Additionally, ultra-short light pulses have granted access to hidden states of matter (*11, 12*), creating novel opportunities for material discovery and control.

In the case of quantum materials with strong electronic correlations spatial complexity across phase transition boundaries demands that measurements be performed with nanometric spatial resolution (*13*). This spatially-resolved approach is needed to map phase inhomogeneities which are thought to play a fundamental role in emergent behavior of a broad class of quantum materials including, but not limited to: colossal magneto-resistance manganites (*14*), Cu and Fe-based High-Tc superconductors (*15, 16*) and transition metal oxides (*17-19*). Merging ultra-fast techniques with nano-meter spatial resolution both brings the unique merits of ultrafast measurements to the nanoscale and enables the exploration of connections between spatial and temporal responses at extreme small time and length scales (*20-23*). It is therefore imperative to develop advanced tools for time-resolved investigation at the nanoscale.

Scattering type near-field optical microscopy (s-SNOM) is well suited for optical spectroscopy and imaging at 10-20 nm length scales. The spatial resolution afforded by this

method is independent of the wavelength of radiation used (*24*). A number of works, where nano-Fourier Transform Infrared (FTIR) spectroscopy (*25-29*) and electro-optic sampling (EoS) (*28*) were used have provided a robust demonstration of the potential to couple ultrafast lasers to s-SNOMs to successfully circumvent the diffraction limit and gain access to time-resolved information at the nanoscale. Recent results have also shown the strong potential to perform rapid time-resolved nano-imaging with s-SNOM (*30, 31*), which enables a detailed exploration of the role of inhomogeneities across quantum phase transitions in complex materials. All these results have demonstrated that ultrafast s-SNOM is a powerful technique with a bright future (*25-33*). We also remark that spatially and temporally resolved measurements utilizing Scanning Tunneling Microscopy (STM) have been presented (*22, 23*).

One potential difficulty in s-SNOM measurements is that a large contribution from background radiation accompanies the desired near-field signals. Decades of experience with s-SNOMs gained by the nano-optics community have identified experimental practices that allow one to suppress the background and thereby acquire genuine, artifact-free near-field data. One potent approach for eliminating the impact of background radiation is the pseudoheterodyne detection (pHD) method (*34*). Within the pHD method, the nano-optical signal is assumed to possess a single near-field amplitude, s, and near-field phase, ψ. The quantities s and ψ may be determined rapidly enabling users of near-field microscopes to acquire two-dimensional images of genuine nano-optical contrast with millions of pixels over realistic timescales. We adapted the pHD method to pulsed laser sources, which are inherently broadband. As each spectral component within the broadband light source may possess a frequency dependent amplitude and phase time-resolved nano-imaging demands a re-examination of the pHD experimental approach. In this chapter, we demonstrate that the pHD method is compatible with pulsed laser sources (*35*) with

experimentally feasible modifications to the pHD technique. Based on extensive analysis and modeling we conclude that pHD acquisition is imperative to obtain genuine nano-optical contrast, at least in specific cases detailed in Ref. (*35*) and within this Chapter. We then present the results for a prototypical insulator-to-metal transition system VO_2, gathered with Tr-pHD with a probe wavelength near 1.5 μm and a pump wavelength near 780 nm. These data are free from the ill influence of multiplicative background radiation and set the stage for spatio-temporal exploration of quantum materials at the nanoscale.

1.2 Overview of time-resolved near-field techniques

The centerpiece is an Atomic Force Microscope (AFM) with the tip of the cantilever illuminated with infrared lasers. The metallic AFM probe is polarized by incident light, and together with its mirror image in the sample, generates an evanescent electric field that is confined to the radius of curvature of the tip (10-20 nm); a feat that stems from the near field coupling between the tip and the sample. The AFM tip is then re-polarized by the tip-sample interaction and radiation is scattered into the far-field (*24, 36*). This radiation, which contains background radiation as well as radiation produced by the near-field interaction, is then sent to a detector. The backscattered radiation from the AFM is usually superimposed with light from a reference arm in order to form an interferometric receiver. Interferometry can be used to eliminate the multiplicative contribution of diffraction limited background radiation and provide phase information - as will be detailed below (*34, 37, 38*). Since the voltage generated by common detectors, u, is proportional to the light intensity rather than its electric field, we consider the square of the sum of all electric fields:

$$u \propto |\tilde{E}_{ref} + \tilde{E}_{BG} + \tilde{E}_{NF}|^2 \qquad (1)$$

Where $\tilde{E}_{ref}, \tilde{E}_{BG}, \text{and } \tilde{E}_{NF}$ are the electric field phasors, respectively, of the reference arm, the background contribution as well as radiation scattered from the near-field. To experimentally eliminate terms, which do not contain near-field information, the well-established tapping technique (*39*) is commonly used. Within this approach, all terms which are not proportional to $\tilde{E}_{NF}$ can be made negligible (Appendix A). Thus, when the tapping technique is used the detected intensity contains only the terms:

$$u_m \propto \tilde{E}_{ref}^* \cdot \tilde{E}_{NF} + \tilde{E}_{BG}^* \cdot \tilde{E}_{NF} + \tilde{E}_{NF}^* \cdot \tilde{E}_{NF} + \text{ C.C.} \quad (2)$$

Typically, the amplitude of the electric field phasors from the background and reference arm are orders of magnitude larger than that from the near field. Thus, the last term in Eq. (2), $\tilde{E}_{NF}^* \cdot \tilde{E}_{NF}$, and its complex conjugate, are negligible and will not be considered in the remainder of this paper. If no reference arm is used, only one term is measured (Appendix C), which is generally referred to as the self-homodyne detection (sHD) method:

$$s^{sHD} \propto 2\left|\tilde{E}_{BG}\right|\left|\tilde{E}_{NF}\right| cos(\Delta\psi_{BG}) \quad (3)$$

Data acquired within the sHD method are proportionate to the amplitude of the background electric field and coupled non-linearly to the background phase. These contributions introduce the so called "multiplicative background" contribution to the sHD signal (Chapter 1.3, Appendix C). It is immediately clear from an examination of Eq. (3) that more advanced methods are required to eliminate the contribution of background radiation. We provide a qualitative discussion, as well as quantitative estimates, of the influence of background radiation in Appendix A and C.

If the reference arm is added, we are left with:

$$s^{HD} \propto 2\left|\tilde{E}_{ref}\right|\left|\tilde{E}_{NF}\right| cos(\Delta\psi_{ref}) + 2\left|\tilde{E}_{BG}\right|\left|\tilde{E}_{NF}\right| cos(\Delta\psi_{BG}) \quad (4)$$

which is often described as the homodyne detection (HD) method. The HD signal is background-free provided the amplitude of the reference field is much stronger than that of the background

field, $\left|\tilde{E}_{ref}\right| \gg |\tilde{E}_{BG}|$ (*40*). To totally eliminate the multiplicative background contribution, the so-called pseudoheterodyne detection method (pHD) (Chapters 1.5, and 1.6) has been devised, which leaves only the term (*34*):

$$s^{pHD} \propto 2\left|\tilde{E}_{ref}\right|\left|\tilde{E}_{NF}\right|cos(\Delta\psi_{ref}) \qquad (5)$$

Furthermore, as we will detail in Chapter 1.5 it is possible to extract both the amplitude and phase of radiation from the near field in the pHD method. By raster scanning the sample while keeping the positions of the AFM and optics fixed, one is able to extract signal from sHD, HD, or pHD on a pixel-to-pixel basis and construct an image.

In order to gain access to time-resolved information we use pulsed laser sources, Fig. 1(a). Radiation from one channel is sent to the AFM to probe the sample's momentary state in the near-field, purple in Fig. 1(a). A second illumination channel is used to pump (or perturb) the sample at a well-controlled time delay, Δt_{ps}, preceding the probing event; the role of the pump is to transiently alter the state of the sample, red in Fig. 1(a). We utilize two digital boxcars (*41*) to measure the pump-induced change of the near-field signal (Chapter 1.4; Appendix B), by collecting simultaneously the signals s_R^X, just before, and s_P^X, at Δt_{ps} after the arrival of pump pulses. We then plot the difference $\Delta s^X = (s_P^X - s_R^X)/s_R^X$ which is non-zero only if the pump transiently modifies the response of a sample at a given pixel. In our notation, the upper script assigns the method of time resolved detection, i.e. pHD for pseudo-heterodyne detection, sHD for self-homodyne detection, and HD for homodyne detection.

1.3 Time-resolved near-field studies of vanadium dioxide

In this work we investigated thin films of vanadium dioxide (VO_2): a correlated electron material that undergoes an insulator-to-metal (IMT) transition above room temperature. The highly oriented VO_2 films on $[001]_R$ TiO_2 substrate, as well as polycrystalline samples on Al_2O_3

substrates, were fabricated by the pulsed-laser deposition method; details of thin film fabrication and characterization have been reported elsewhere (*17, 42*). Static near-field imaging works have shown that VO_2 experiences a percolative phase transition with co-existing insulating and metallic states amidst the IMT (*17, 19, 42*). The transition temperature of VO_2 films can be tuned by epitaxial strain (*43*). In general, compressive (tensile) strain along c_R yields T_{IMT} lower (higher) than in bulk (*42-44*). Bulk crystals and unstrained polycrystalline films on sapphire substrates usually have an IMT close to T_{IMT} =340 K. Films on $[001]_R$ TiO_2 substrate are compressively strained along c_R, leading to a T_{IMT} < 340 K (*42*). Topographic corrugations, or "buckles", locally relieve the strain in samples grown on TiO_2 $[001]_R$. This creates a gradual increase in T_{IMT} in mesoscopic region in the proximity to the center of the buckles. The mid-infrared optical response of the highly inhomogeneous IMT in VO_2 films grown on Al_2O_3 has been previously characterized with static s-SNOM (*17*). The character of emergent domains can be classified as being in the random field Ising universality class, at least in a narrow temperature range surrounding the IMT (*45*). Data obtained by ultrafast (*8, 9, 46*) and nanoscale (*17*) methods have also provided insights into the long-standing debate regarding the roles of electronic or structural effects in the IMT, possibly revealing the existence of a monoclinic metallic state (*47*). The pioneering studies on nanoscale dynamics in VO_2 have recently been published (*29, 30*).

In the present work we have investigated VO_2 thin films using s-SNOM that we have adapted for transient pump-probe experiments. In all measurements presented in this manuscript near-infrared radiation with 1.55 μm center wavelength and 15 nm bandwidth were used as the probe at the repetition rate of 600 kHz. For the pumping channel we used 1 mW of 780 nm radiation at a repetition rate of 300 kHz. Figs. 1(b), and (c) summarize our key experimental results. Here we plot data collected for VO_2 film on TiO_2 $[001]_R$ substrate. In Fig. 1(b) we plot the Tr-sHD

signal, $\Delta S^{sHD} = (S_P^{sHD} - S_R^{sHD})/S_R^{sHD}$ at a time delay of Δt_{ps} = 300 ps, which is much longer than the approximately 100 fs pulse duration of the pump and probe pulses. This late time delay was chosen as the peak pump induced change in reflectivity observed in (*7*), by Hilton et al., was not fully formed until $\Delta t_{ps} \cong$ 300 ps. In Fig 1(c) we plot the Tr-pHD signal, $\Delta S^{pHD} = (S_P^{pHD} - S_R^{pHD})/S_R^{pHD}$ at the same time delay. With Tr-sHD a clear contrast is observed along buckles in our film, Fig. 1(b) whereas this is not the case in data taken on a similar region of the VO_2 thin film using Tr-pHD under identical pumping conditions Fig. 1(c). We emphasize that no pump-induced features above our noise floor are observed in the data in Fig. 1(c). A detailed analysis of results generated in the Tr-sHD method, Appendix C and Ref. (*35*), shows that the response displayed in Fig. 1(b) is in approximate quantitative agreement with an artificial response generated from the background radiation. The results of Figs. 1(b) and (c) demand a critical evaluation of the data-acquisition protocols for time-resolved near-field measurements.

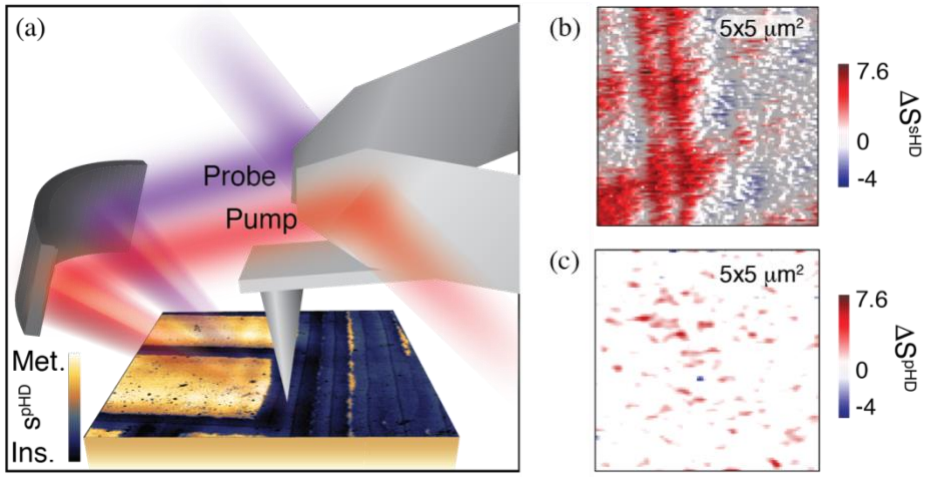

Fig. 1. Infrared time-resolved nano-imaging experiment and results. a) Diagram showing the experimental apparatus. The ultrafast probe beam (purple) is focused onto the apex of an AFM probe at a precise time delay following a perturbation caused with a second ultrafast pump beam (red). Static infrared image, which was collected with the Tr-pHD method using the 5th harmonic of the tip-tapping frequency with a pulsed laser source. This image was obtained on a

representative 10x10 μm² region. This image reveals metallic regions (gold) due to the compressive strain of the substrate as well as insulating regions (blue), where the film is strain relieved. b) Tr-sHD results obtained on the VO_2/TiO2 [001] sample in a 5x5 μm² region at the pump probe time delay Δt_{ps}=300 ps. c) Tr-pHD results obtained on the VO_2/TiO2 [001] sample in a 5x5 μm² region at the same time delay as in panel (b).

1.4 Methods for time-resolved near-field detection

We now proceed to develop a detailed comparison between the aforementioned data-acquisition protocols. Within the sHD method, Fig. 2(a), one utilizes a 50/50 beam splitter to collect back-scattering radiation from the AFM probe (Neaspec GmbH.) and guide this radiation to a detector. The AFM probe is tapped at a frequency Ω in the immediate proximity of the sample, which creates observable peaks at mΩ (with m = 1, 2, 3, etc.) when the detected signal is plotted against frequency, Fig. 2(d). The HD method Fig. 2(b) requires the addition of a reference arm configured in an asymmetric Michelson interferometer scheme. The path length difference between the interferometer and the backscattered radiation from the AFM probe is set to zero such that both pulse trains interfere constructively, which enhances the signal at mΩ, Fig. 2(e). The pHD method requires the path-length difference between the reference arm and sample to be modulated at a second frequency, M, Fig. 2(c). In pHD, the signal contained in the peaks at mΩ is partly transferred to sidebands separated by the tip tapping frequency, at mΩ +/– NM, (where N=1, 2, etc.) Fig. 2(f). The suppression of far-field background is strongly affected by the choice of imaging method, as qualitatively outlined in Chapter 1.2.

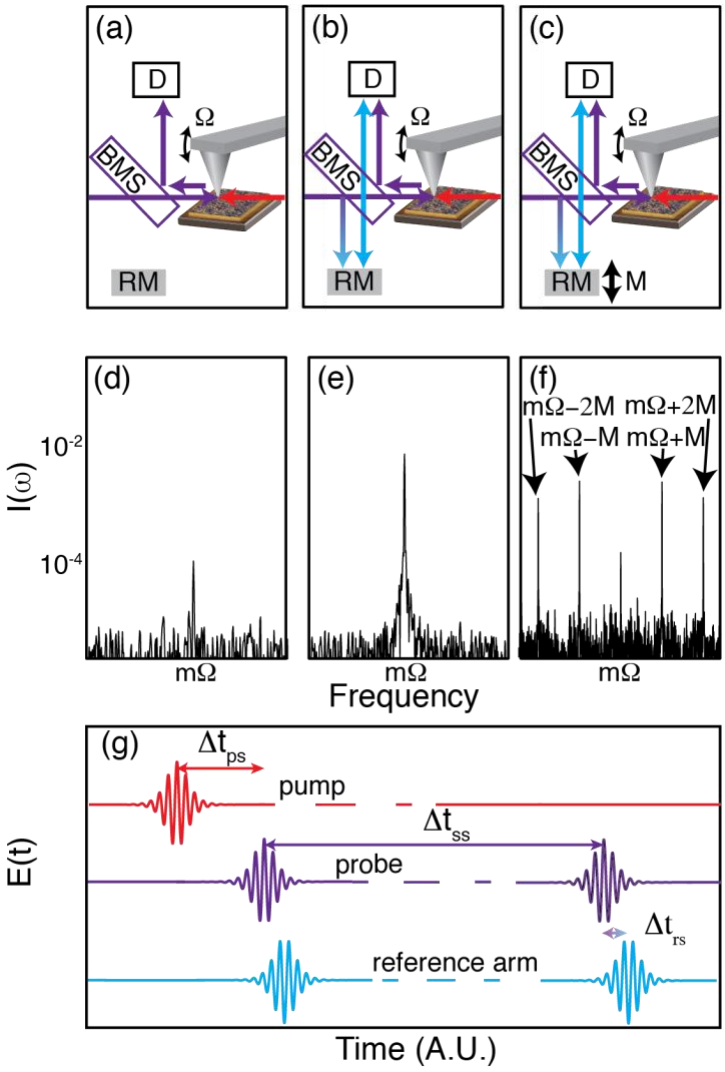

Fig. 2. Schematic of detection methods. a-c) Various detection methods with the radiation from the probe (purple), reference arm (blue) and pump (red) shown. BMS = 50/50 Beamsplitter; RM = Reference Mirror; D = Detector. a) sHD method, backscattered light from the AFM is steered into the detector. b) HD method where a reference arm is added. c) pHD method where the reference arm position is modulated at a frequency M. d-f) Signals acquired using the detection methods in a-c. d) sHD signal, which shows peaks at high harmonics of the tip tapping frequency mΩ. e) HD signal, which shows that the magnitude of the peaks at mΩ are enhanced. f) pHD signal, which shows that, the peak at mΩ has returned to its sHD value. Additional peaks appear at the sum and or difference frequencies between the high harmonics of the tip tapping frequency and harmonics of the reference arm mΩ +/-NM. g) Schematic of the pulses involved and relevant time scales. In the schematic we show the individual pump (red), probe (purple) and reference (blue) pulses on the femtosecond timescale. A much longer time delay, Δt_{ss} – which is the inverse of the repetition rate of the laser system – is indicated by the dashed line. The dashed line separates the first (ON) event, where both the pump and probe pulses arrive at the sample and a second (OFF) event where only the probe pulse arrives at the sample. This process is

periodically repeated, and data are collected by separately integrating the detected voltage from many ON and OFF events. In the case of HD and pHD methods radiation in the reference arm (blue) temporally overlaps with the probe radiation. In the case of the pHD method, the time delay between reference and probe light, Δt_{rs} is modulated sinusoidally at a frequency M.

In Fig. 2(g) we show a schematic representation of the pulses involved and indicate the relevant time scales. To attain the highest possible signal-to-noise of the transient component of the near-field signal we adapted a boxcar-based approach (*41*) to time-resolved s-SNOM measurements. In this approach one utilizes a *pair* of probe pulses. The first (ON) probe pulse follows the pumping event at time delay Δt_{ps}, marked by the red arrow in Fig. 2(g). This pulse provides signal associated with the pump-induced state of the sample at a time delay Δt_{ps}. An electro-optic, or acousto-optic, modulator is used to eliminate the following pump pulse: an OFF event in our notation. The OFF probe pulse, therefore, arrives at a much later time delay $\Delta t_{ps} + \Delta t_{ss}$ after the pumping event. Provided the sample has recovered its unperturbed state at $\Delta t_{ps} + \Delta t_{ss}$, the OFF signal contains information about the sample's, unperturbed, steady state. The intensities from both ON and OFF probe pulses are measured in a photoreceiver, whose response time is faster than the wait time between probe pulses, Δt_{ss} (Appendix B), and the output is electronically integrated with a digital Boxcar (Zurich UHF-BOX). This process is repeated periodically, and the integrated intensity values are registered as discrete data points at half of the repetition rate of the laser system. Standard lock-in demodulation of the boxcar outputs feeds the tapping harmonics of both ON and OFF probe pulses, provided that the repetition rate is sufficiently fast to satisfy the Nyquist criterion (Appendix B). The difference in the voltages demodulated from the ON and OFF pulses yields the information of reversible pump-induced changes to the sample.

Interferometric detection, where a pulsed laser is used, implies that the reference pulses temporally overlap with those from the sample on the detector. In Tr-HD, this is accomplished by

using a micrometer stage to minimize the temporal mismatch between the tip-sample and reference arms, Δt_{rs} in Fig. 2(g), which places their interference at a constructive maximum. In Tr-pHD, the temporal-mismatch between probe and reference arms, Δt_{rs}, is first minimized and then modulated sinusoidally at a frequency M (*34*). By detecting the intensity at sidebands of the near-field signal mΩ +/- NM the Tr-pHD signal collects interference terms between the near-field and reference arm (Eq. (3)), thereby eliminating the multiplicative background contribution.

1.5 Pseudoheterodyne detection for artifact-free time-resolved near-field imaging

In a static setting, pHD has been reliably used in a wide array of nano-infrared experiments over the past decade (*17-19, 34, 48*). To determine if the pHD method is compatible with pulsed laser sources and time resolved measurements, we proceed to discuss the quantitative details of the transient pseudoheterodyne method (Tr-pHD).

The first main benefit of the Tr-pHD method is that the influence of background radiation is eliminated, as shown in Chapter 1.2. The second main benefit of Tr-pHD is that the amplitude and phase of the scattered field from the tip-sample interaction can be simultaneously extracted, analogous for CW laser sources, as shown in Chapter 1.5 (*34*). The finite temporal duration of an ultrafast laser, however, implies that there is a finite spectral bandwidth associated with the pulse train. In the case of broadband laser sources each frequency component of the detected signal is characterized with its own amplitude and phase. It is therefore prudent to examine the extraction of the pHD amplitudes and phases in the case of broadband pulsed laser sources.

In order to evaluate what signals are recorded by a lock-in amplifier, we consider the detected intensity. Note that the full expression for the detected intensity, when a pulsed laser source is used, is comprised of three periodic events. These are (1) the tip-tapping motion, (2) the reference arm phase modulation, (3) the arrival of laser pulses. We showed in Ref. (*35*) that the

periodic train of laser pulses may be neglected in the demodulation of Tr-pHD signals. Therefore, we simply need to evaluate the appropriate Fourier expansion coefficients for the reference arm and tip-sample interaction (*34*). The Fourier expansion coefficient of the electric-field scattered from the tip-sample is $c_m = |\tilde{\xi}_m(\omega)|\, e^{i\psi_m(\omega)}$, where we emphasize the dependence of the electric field phasor on optical frequency ω (*28*). To get the Fourier coefficient of the reference arm in the frequency domain we note that a sinusoidal variation in Δt_{rs}, Fig. 2(g) implies that the spectral phase is modulated as $\omega_0 a_{mod} \cos(\mathrm{M}t)$ according to the Fourier shift theorem, where a_{mod} is the tip modulation amplitude:

$$\tilde{\xi}_r(\omega) = \left|\tilde{\xi}_r(\omega)\right| e^{i\left(\omega a_{mod}\cos(\mathrm{M}t)+\psi_{ref}(\omega)\right)}$$

$$= \sum_{N=-\infty}^{\infty} \left|\tilde{\xi}_r(\omega)\right| J_N(\omega a_{mod}) e^{i(\psi_{ref}(\omega)+\frac{N\pi}{2})} e^{i(N\mathrm{M}t)} \quad (6)$$

We used the Jacobi-Anger expansion in the second half of Eq. (6) to expand the reference arm electric field in terms of harmonics of the reference mirror modulation frequency. The Fourier expansion coefficient of the reference arm may be read directly from Eq. (6) as $c_N = \left|\tilde{\xi}_r(\omega)\right| J_N(\omega a_{mod}) e^{i(\psi_{ref}(\omega)+\frac{N\pi}{2})}$. Finally, as justified in Ref. (*35*), see Appendix B, when the detected voltage is demodulated at frequency mΩ +/ NM the output is proportionate to the expansion coefficients, $u_{m,N} \propto c_N^* c_m + c_m^* c_N$.

In the case of a continuous wave (C.W.) laser, we evaluate $u_{m,N}$ at a single frequency, ω_0:

$$u_{m,N} \propto \left|\tilde{\xi}_{NF}(\omega_0)\right|\left|\tilde{\xi}_{ref}(\omega_0)\right| J_N(\omega_0 a_{mod}) \cos\left(\Delta\psi_{ref}(\omega_0) - \frac{N\pi}{2}\right) \quad (7)$$

Eq. (7) is identical to the formula derived by Ocelic et al., for the detected voltage demodulated at frequency mΩ +/ NM in (*34*). Equation (7) can be further simplified when the first and second order Bessel functions are equal, i.e. when $J_1(\omega_0 a_{mod}) = J_2(\omega_0 a_{mod})$, which happens with $\omega_0 a_{mod} =$

2.63. A condition, which is satisfied by setting the reference mirror's physical oscillation amplitude to $\Delta l = c a_{mod}/4\pi\omega_0$. The amplitude of the near-field signal is then recovered by taking:

$$s_m \propto \sqrt{u_{m,1}^2 + u_{m,2}^2} \quad (8)$$

Likewise, the phase can be recovered with:

$$\varphi_m \propto tan^{-1}(u_{m,2}/u_{m,1}) \quad (9)$$

where $tan^{-1}(x)$ is the inverse tangent of an argument x. This procedure provides a reliable method for extracting the near-field amplitude and phase in a static setting.

We now proceed to analyze the pHD method for signal recovery in measurements employing a broadband pulsed laser. The condition that $J_1(\omega a_{mod}) = J_2(\omega a_{mod})$ cannot be simultaneously satisfied for all ω due to the finite bandwidth of the pulse train. To determine the voltage recovered with a broadband source, one must average over the frequency content of the laser, which is weighted by the frequency dependent response function of the detector element $\mathcal{R}(\omega)$ for a particular choice of a_{mod} (*28*):

$$u_{m,N} \propto \int \mathcal{R}(\omega)|\xi_{NF}(\omega)|\left|\xi_{ref}(\omega)\right|J_N(\omega a_{mod}) \cos\left(\Delta\psi_{ref}(\omega) - \frac{N\pi}{2}\right) d\omega \quad (10)$$

A cursory inspection of Eq. (10) reveals that the finite bandwidth of the laser source introduces several complications. Near-field information collected is necessarily averaged over the bandwidth of the laser pulse, which is altered by the spectral responsivity of the detector, $\mathcal{R}(\omega)$ and further weighted by the frequency dependent electric field, $\xi_{NF}(\omega)$. The detected response is also weighted by the Bessel functions $J_N(\omega a_{mod})$ which is a specific consequence of the pHD method.

We will now analyze the uncertainty of both amplitude and phase measurements within the pHD method by considering the worst-case scenario error. To do this, we calculated the pHD amplitude measured with a broadband source, Eq. (10), normalized to the monochromatic value:

$$s_m(\Delta\varphi_{ref})/s_{cw} = \frac{[(\int \xi(\omega) J_1(\omega a_{mod}) \sin(\Delta\psi_{ref}) d\omega)^2 + (\int \xi(\omega) J_2(\omega a_{mod}) \cos(\Delta\psi_{ref}) d\omega)^2]^{1/2}}{J_1(2.63\ rad) \int \xi(\omega) d\omega} \quad (11)$$

In our calculations, shown in Fig. 3 we make several simplifying assumptions that yield a worst-case scenario estimate of the error. We consider a case that the spectral field, $\xi(\omega)$, is a box function in the frequency domain, shown in Fig. 3(a), whose inverse Fourier transform has a pulsed nature (inset). We also neglect second order, and higher, spectral modifications to the phase so that $\Delta\psi_{ref}$ is a constant. In Fig. 3(b) we plot the normalized pHD amplitude Eq. (11), which is measured by a pulsed laser source, as a function of the laser bandwidth to center wavelength or relative bandwidth, $\Delta\omega/\omega_c$. We note that there are two shortcomings when pHD is used with a pulsed laser source. These are: (1) the amplitude that is recovered with a broadband laser source is less than what would be recovered with a monochromatic laser source; (2) the pHD amplitude recovered from a pulsed laser *does* depend on relative difference between the near-field phase of the sample and that from the reference arm, $\Delta\psi_{ref}$. However, we observe that both of the aforementioned shortcomings are drastically reduced provided narrowband laser sources are used, as is the case with most experiments.

We proceed to quantify the extent to which the bandwidth of the pulse train may contaminate a measurement of the near-field amplitude. In Fig. 3(b) we display $s_m(0)/s_{cw}$ (black) and $s_m(\pi/2)/s_{cw}$ (red). We highlight in the inset that for a relative bandwidth, $\Delta\omega/\omega_c < 0.1$ the recovered amplitude is within a few percent of the value that would be recovered for a monochromatic laser source, for all $\Delta\psi_{ref}$. This systematic error is comparable to the smallest signals that are observable in state-of-the-art near-field experiments. For $\Delta\omega/\omega_c < 0.05$ the error is less than 0.5% and will not be observable in most near-field measurements. We therefore conclude that the error remains below typical noise levels in near-field experiments when narrowband laser sources are used.

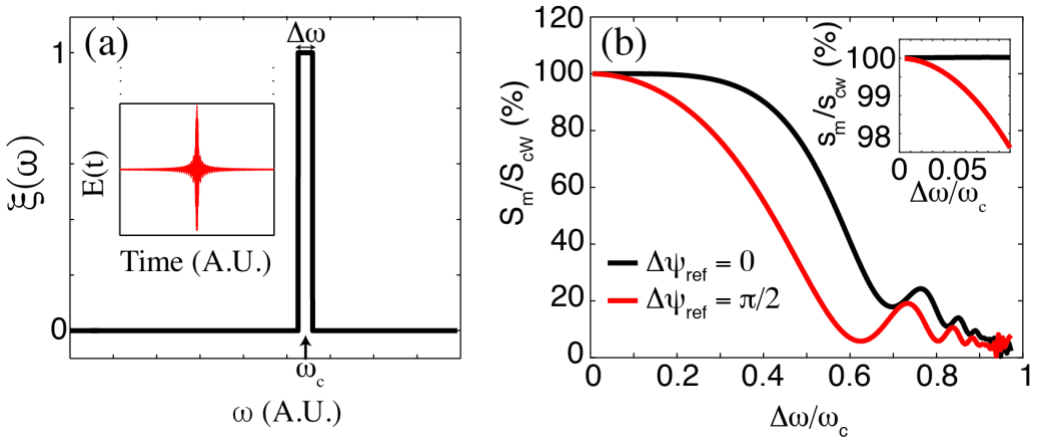

Fig. 3. Modeling amplitude errors within the Tr-pHD method. a) Spectral field used in our calculation, $\xi(\omega)$, vs frequency, ω. The Fourier transform of this field is displayed in the inset. b) Near-field amplitude collected with a pulsed laser normalized to the value that is anticipated for a monochromatic source, s_m/s_{cw}. We plot this quantity against the relative bandwidth of the laser source, $\Delta\omega/\omega_c$, as shown in panel a. We include this calculation for two values of the near-field phase relative to that of the reference arm, $\Delta\psi_{ref}=0$ (black) and $\Delta\psi_{ref}=\pi/2$ (red). A zoom in of the narrow bandwidth region is shown in the inset.

The results presented in Fig. 3 show that the near-field amplitude and phase can be reliably recovered with pHD when a narrowband pulsed laser source is used. By incorporating a second illumination channel to pump the sample background-free time-resolved measurements of the near-field amplitude and phase may be carried out, red signal in Figs. 1(a), 2(g). When the boxcar approach is used to extract the Tr-pHD amplitude all common phase changes between the ON and OFF pulses are also canceled. These effects include, but are not limited to, drift of the reference arm phase relative to that from the sample, as well as static variations in the near-field phase, Chapter 1.4; Appendix B; Fig. 2(g). Thus, the only changes observed in the Tr-pHD amplitude will stem from pump-induced changes to amplitude and phase of genuine time-resolved near-field features. Therefore, Tr-pHD procedure provides a reliable method for extracting artifact free time-resolved near-field amplitude and phase.

1.6 Pseudoheterodyne detection for artifact-free time-resolved near-field imaging

In the previous sections we discussed advantages of the Tr-pHD method. In Fig. 1 we have shown that while we detected a finite Tr-sHD signal in the VO_2/TiO_2[001] films, we were un-able to reproduce these results using Tr-pHD. We note that long timescales for recovery from the metallic state to the insulating state is characteristic of VO_2 films grown on substrates where the thermal conductivity is close to or less than that of the film itself (*49*). These substrates include SiO_2 (*31*), and TiO_2 (*19*). The recovery timescale can extend to hundreds of μs in films grown on these substrates, which supports the view that cumulative heating may be the dominant pump-induced effect at our repetition rate of 300 kHz and may account for the observation of zero pump-induced near-field signal when the probe arrives hundreds of picoseconds after the pumping laser. To overcome this difficulty, we examined VO_2 films on substrates with thermal conductivity significantly higher than that of VO_2, where the recovery time is much less than 1.5 μs. These latter substrates include Al_2O_3, MgO, and Au.

In Fig. 4 we display the results obtained using Tr-pHD for a VO_2/uAl_2O_3 film. In Fig. 4(a) we plot the AFM topography. Grains are clearly observed in this image, which are typical of polycrystalline films (*17, 19, 42, 50*). In Fig. 4(b) we plot the static pHD data, where we observe slight variations in near-field signal at grain boundaries. In Fig. 4(c) we plot the Tr-pHD signal, which is the normalized relative difference of the pHD signals taken from the pump-induced, S_P^{pHD}, and static, S_R^{pHD}, states, $\Delta S^{pHD} = (S_P^{pHD} - S_R^{pHD})/S_R^{pHD}$. We observe a ~2% homogeneous increase in the Tr-pHD signal at approximately pump-probe overlap, $\Delta t_{ps} = 0$. Our pump fluence is below the threshold required to fully excite the IMT. This low-fluence regime is expected to show rapid (sub-ps) decay dynamics according to Refs. (*30, 51*) and our results are consistent with these earlier reports.

We attribute the pump-induced change in near-field signal at $\Delta t_{ps} = 0$ to the injection of free carriers into the conduction band. The pump-induced change to the near-field amplitude, which were collected with Tr-pHD, shows a completely homogeneous response at this time delay, within our noise floor. The difference in our findings from those presented in Ref. (*30*) can stem from a number of factors including: the different wavelength of the probe we utilize, the differences between crystalline nano-beams utilized in Ref. (*30*) and granular films in Fig. 4 or the different data acquisition method used.

Interestingly, while optical contrast is observed at grain boundaries in the static near-field image, we do not observe features at these locations in the image which displays the measured pump-induced difference in near-field signal. We speculate that the observation of optical contrast in the static image stems from a geometric enhancement of the near-field signal when the AFM probe is inside of the grain boundaries. The geometric enhancement is common between the pumped and reference images that are acquired, and this signal enhancement cancels in the difference signal shown in Fig. 4(c) in lieu of a genuine variation in the itinerant carrier density at these locations. We note that the noise level, which is < 0.5% RMS is well below the observed pump induced change of 2% that is shown in Fig. 4(c). The pump induced contrast is lower than in Ref. (*30*), which stems from the difference in probe wavelength used in our work. A detailed exploration of the insulator-to-metal phase transition in a similar Vanadium Dioxide thin film with mid-infrared radiation and higher pump fluence is presented in Chapter 2. The data presented in Fig. 4, which were collected with the Tr-pHD method, show time-resolved near-field images collected with the s-SNOM technique that are guaranteed to be artifact free.

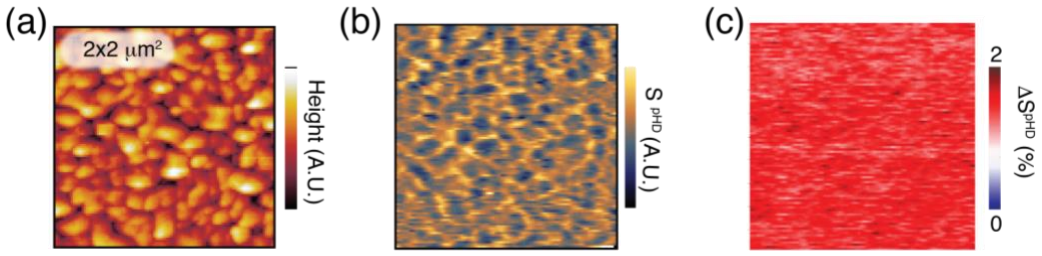

Fig. 4. Artifact-free near-field data with a pulsed laser source. a) AFM data, which measures the topography, or local height, of the film in a 2x2 μm2 region. b) pHD data with a pulsed laser source corresponding to the topography in panel a. c) Tr-pHD data that was collected simultaneously with Figs 4(a) and (b).

1.7 Outlook and conclusions

In the header of Fig. 5 we briefly outline selected materials and phenomena that may be explored with pulsed laser sources in time-resolved and spectroscopic near-field measurements. At the longest wavelengths, THz s-SNOM is ideally suited to control and interrogate electronic properties of complex materials (*4, 52*), Josephson plasmon resonances in layered superconductors (*53*), hyperbolic polaritons in topological insulators (*54*), spin precession in ferromagnets (*55*) and anti-ferromagnets (*56*), as well as vibrational (*57*) and rotational (*58*) motions in a wide range of systems. The mid-IR spectral range is sensitive to the plasmonic modes in graphene (*26, 27, 48, 59, 60*), hyperbolicity in Hexagonal Boron Nitride (*61*), phonon resonances (*36, 42*) as well as the electronic properties of many materials (*17-19, 42*). The pulse duration of mid-IR radiation is typically 40-200 fs, which is sufficient to gain access to timescales where electron-phonon, and electron-spin coupling have not yet brought the electronic system into thermal equilibrium (*51*). In the visible range several interesting spectral features such as excitonic modes in transition metal dichalcogenides (*62, 63*), plasmonic modes in metals and topological insulators (*64*), as well as resonances related to interband transitions in insulators, across charge transfer and Mott-Hubbard

gaps can be observed. The pulse duration of visible radiation, which can be in the range of 4-40 fs, also enables indirect access to resonant modes in the infrared spectral range such as coherent phonons and Raman active modes (*65*, *66*). Additionally, ultra-short light pulses can be used for sub-cycle interrogation of processes excited with carrier envelope phase stable mid-IR (*67*) and THz pulses (*56*). We stress that the efficient background suppression afforded by Tr-pHD with pulsed laser sources may find use in a wide array of spectroscopic measurements in addition to time-resolved control and interrogation of matter at the nanoscale.

In Fig. 5 we also display the calculated near-field signals and additive background contribution in these spectral ranges. These results show that as the demodulation order of the tip-tapping harmonic is increased the background contribution tends toward zero more quickly than the near-field signal over the entire spectral range plotted. We emphasize that taking higher harmonics in the tapping technique does not eradicate multiplicative background artifacts, as discussed in Chapter 1.2 and Appendix C. Advanced techniques, such as Tr-pHD, are required to generate data that are immune from background complications. We note that pulsed laser sources are uniquely qualified for the task of generating radiation across the ultra-broad spectral range displayed in Fig. 5 with a single light source. The extremely high peak power densities, which are commonplace in pulsed laser sources, are ideal for exciting non-linear processes thereby enabling generation radiation spanning from the EUV-THz. Thus, in addition to the time-resolved studies, which are at the focus of our analysis, Tr-pHD with pulsed sources may find great utility in ultra-broadband, static, characterization of samples as well. Coupling pulsed sources to an s-SNOM enables novel opportunities for steady-state and time-resolved characterization of samples over an ultra-broad spectral range.

In the visible range achieving an excessive near field to background ratio requires that minimal tapping amplitudes and very high harmonics are used, which in turn implies that there is a significant sacrifice to the attainable dynamic range in pristine nanoscale measurements. Additionally, while the ultrashort pulse durations are attainable these imply a significant relative bandwidth, which in turn leads to error in the extracted pHD amplitudes as the authors discussed in the context of Fig. 3. More exotic techniques that do not rely on the tapping technique, and Tr-pHD, have been demonstrated where all of the detected radiation stems from the near-field interaction (*68, 69*). These techniques have the capacity to preserve high S/N ratios, as well as ultra-short pulse durations of broadband visible radiation, without compromising the high levels of background suppression that are required for proper near-field detection. The techniques in Refs. (*68, 69*) may, therefore, eventually provide a significant enhancement to the performance of Tr-SNOM experiments in the visible spectral range. In the mid-IR range the second or third harmonic provides nearly background free data. Interestingly, in the THz range even demodulation to linear order may provide adequate background suppression in many cases (*52*). Under these conditions Tr-pHD can be used for reliable artifact-free time-resolved near-field imaging.

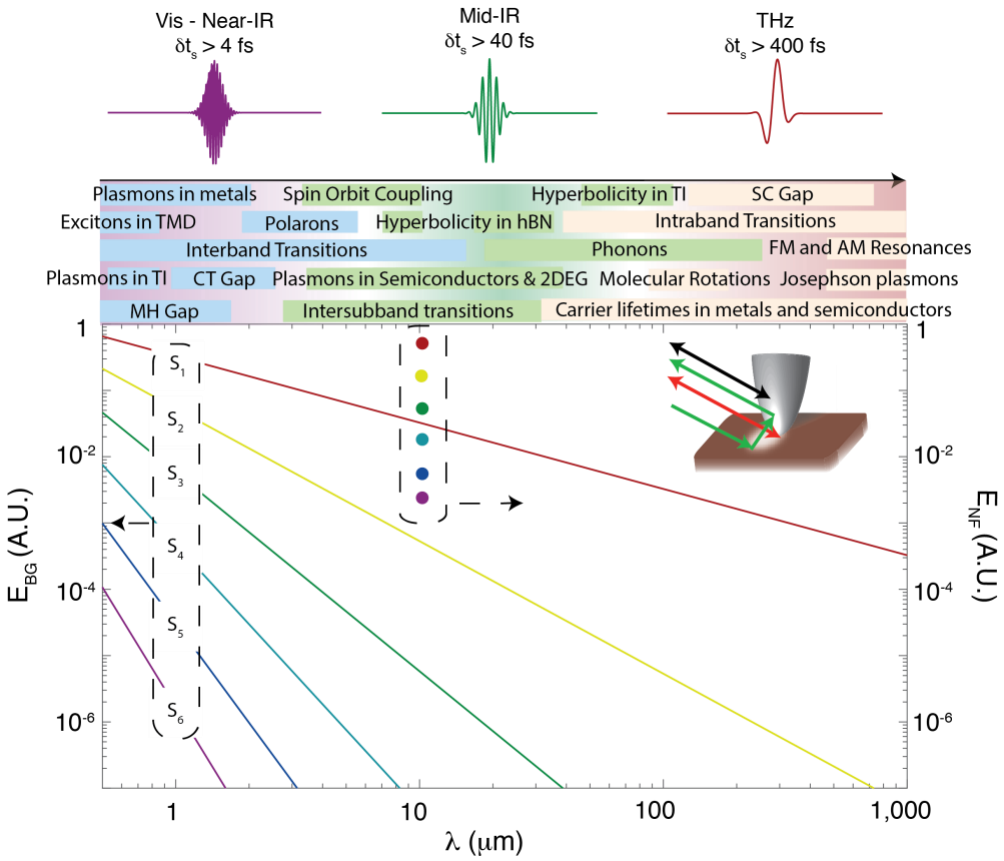

Fig. 5. Numerical values of the near-field and background contributions in s-SNOM measurements and the spectroscopic observables that may be explored with Tr-pHD. In Vis - Near-IR spectral regions the temporal duration of laser pulses δt_s is typically greater than 4 fs. In Mid-IR typical values of δt_s are greater than 40 fs. In THz region one usually deals with δt_s greater than 400 fs. Various spectroscopic observables are highlighted. TI = Topological Insulator; SC = Superconducting; TMD = Transition Metal Dichalcogenides; hBN = Hexagonal Boron nitride; FM = Ferromagnetic; AM = Anti-Ferromagnetic; CT = Charge Transfer; MH = Mott-Hubbard; 2DEG = 2D-Electron Gas. The main panel shows the magnitude of the background electric field phasor (solid lines) calculated as described in Appendix A for harmonics of the tip-tapping frequency s_1 (red), s_2 (yellow), s_3 (green), s_4 (light blue), s_5 (dark blue), s_6 (purple). We also show the calculated magnitude of the electric field phasor from the near-field (dots at 10 μm) in the identical color scheme. In the inset we show a schematic representation of scattering processes that yield the background electric fields plotted here and discussed in Appendix A, with radiation from the near-field indicated by the red arrow, radiation that is directly scattered from the tip-shaft indicated by the black arrow and radiation that is scattered off of the sample, and then by the tip-shaft indicated by the green arrow. The near-field contribution to the signal is found to significantly outweigh the background contribution for

high harmonics of the tapping frequency throughout the entire spectral range plotted.

In conclusion, we have critically evaluated various detection protocols for time-resolved near-field measurements. Our modeling and experiments on VO_2 films show that the pHD method of acquiring transient pump-probe data is guaranteed to eradicate complications arising from multiplicative background. Furthermore, we demonstrated that for narrowband pulsed laser sources ($\Delta\omega/\omega_c < 10\%$) pHD may be used in the same fashion as continuous wave laser sources - with the caveat that the pHD amplitude and phase recovered will be integrated over the bandwidth of the pulsed laser source. The limitations of, as well as novel time-resolved and spectroscopic possibilities using, Tr-pHD were detailed. Finally, we presented time-resolved nano-imaging data for VO_2/TiO_2 and VO_2/Al_2O_3 films collected with the Tr-pHD method. The totality of data and analysis presented in this work indicates that Tr-pHD is a powerful tool for static and time-resolved nano-imaging and spectroscopy across a broad spectral range.

Chapter 2: Nanotexture of the transient Insulator-to-Metal transformation in vanadium dioxide

In quantum materials giant responses result from small perturbations – a property which renders quantum materials as tremendously appealing as they are challenging to understand. Near phase transition boundaries small local variations of the equilibrium properties can produce multiple distinct phases within segregated regions of real space. It is, thus, believed that the gaps within our understanding of quantum materials can, in many cases, be associated with real space complexity (*13*). Furthermore, photoexcitation endows researchers with unprecedented control to traverse the complex energy landscapes of quantum materials accessing phases that may, but need not, have equilibrium analogues on-demand (*70*). The development of advanced experimental probes with real-space resolution commensurate with the native length scales of phase-separation, and with temporal resolution that is sufficient to monitor dynamics following photo-excitation events, is of paramount importance.

2.1 Motivation and experimental setup

In this chapter, we report our study of dynamics of the photo-induced insulator-to-metal (IMT) phase transition in Vanadium Dioxide (VO_2). We utilized the technique of time-resolved scattering near-field optical microscopy (Tr-SNOM) to access nano-optical contrast on the natural length-scale where insulating and metallic phases co-exist in real space (*17, 19, 42, 44, 71*). In our experiments, the metalized tip of an atomic force microscope (AFM) is illuminated with p-polarized pulsed mid-infrared radiation (600 $cm^{-1} < \omega <$ 1100 cm^{-1}). The evanescent field is confined to the tip apex with radius of curvature, a. The extreme confinement provides access to optical contrast with a=20 nm spatial resolution independent of the wavelength of probe radiation (methods, SOM). By triggering the IMT with an abrupt photo-excitation event and interrogating

the sample with a second co-focused mid-infrared probe at a well-controlled time delay (*35*), we explore femtosecond (fs) dynamics. Our works expands on the pioneering efforts to investigate transient phase separation at the nanoscale in the photo induced IMT (*7, 20, 30, 31, 46*).

While earlier works provided evidence that the IMT was inhomogeneous in real space the mechanism that produced inhomogeneity remained elusive. Our findings confirm that the transient IMT is inhomogeneous. The experimental evidence presented in this section, using the multimodal approach grounded in time-resolved nano-spectroscopy and nano-imaging provides additional insight. Our results indicate there is an inhomogeneous strain environment in our particular VO_2 thin film at equilibrium at the nanoscale. The nano-textured strain environment, furthermore, shows real-space correlation with the transient conductivity. Our systematic study of fluence dependence of the spatially resolved dynamics establish local values for the fluence threshold for $M_I \rightarrow R_M$ transition, F_c. A second growth process is identified at pump fluences well below F_c, with an inhomogeneous rise time, τ^{-1}. The parameters F_c and τ^{-1} are found to govern the inhomogeneous nano-texturing of the transient conductivity.

2.2 Dynamics of the insulator-to-metal transition at the nanoscale

Two-dimensional nano-optical images of the transient scattering near-field amplitude, S, collected at with a probe frequency of $\omega = 1000\ cm^{-1}$ are represented by the false color map in Fig. 1. Our transient images expose the progression of the IMT in real space as a function of time. The near-field amplitude gradually evolves from a value characteristic of the insulator to a much higher value that is associated with a photo-driven increase of the local conductivity. At pump-probe overlap (t_0) the near-field amplitude increases at all locations, inhomogeneity of the photo-induced change of S, ΔS, is hardly apparent at this time delay. Following partial recovery of S on the

picosecond timescale (t_1) a prominent increase of the near-field amplitude, S, progresses on a timescale of several hundred picoseconds (t_2). Our transient nano-images expose remarkable spatially segregated transient conductivity, Fig. 6.

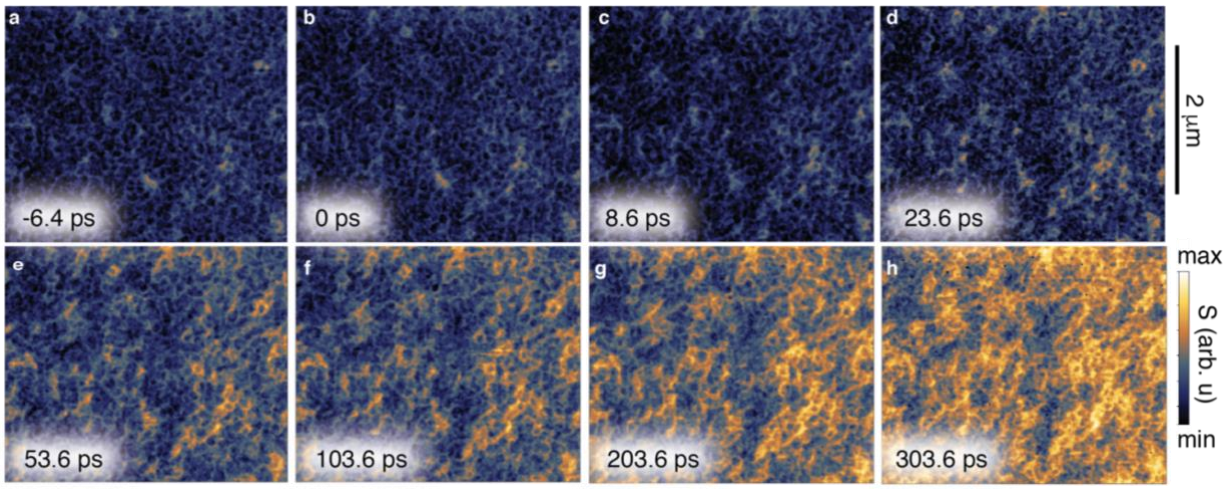

Fig. 6: Time resolved nano-imaging of the photo-induced insulator to metal transition in vanadium dioxide. The sequence of co-located images shows the scattering near-field amplitude, S, recorded at a probe frequency of ω = 1000 cm^{-1} after photo-exciting the crystal with a 5 mW pump beam. The sample was held fixed at the base temperature of T=330K and a pump with above band-gap frequency (ω_{pump} = 9,700 cm^{-1}) was utilized for all data displayed in this chapter unless otherwise indicated. The displayed images were recorded at as a series of pump-probe time delays, a, -6.4 ps, b, 0 ps, c, 8.6 ps, d, 24 ps, e, 54 ps, f, 104 ps, g, 204 ps, h, 304 ps. A 2 μm scale bar is provided on the right-hand side of the figure for reference.

2.3 Static Characterization of the VO_2 thin film

We proceed to characterize our VO_2 thin film at equilibrium. First, we focus on the near-field amplitude measured at room temperature. At the probe frequency of ω = 909 cm^{-1} two-dimensional images of the near-field amplitude are completely featureless, Fig. 7a (*17*). At the slightly lower probe frequency of ω = 715 cm^{-1} real-space variation of the near-field amplitude exposes heterogeneity, Fig. 7b. Nano-infrared spectra acquired at selected locations are displayed in Fig. 7c (methods). At all locations, we observe the same general trend in the near-field spectra that is consistent with the IR active response of monoclinic phonons (*42*, *72*, *73*). To extract quantitative

information about local variations in the IR phonon response we model the optical permittivity of VO_2 with a series of Lorentzian oscillators (Chapter 2.7). Using the lightning rod formalism (*36*), we compute spectra of the scattering near-field amplitude, with the Lorentz model for the dielectric response of VO_2 as the input, and extract the parameters reported in Table 1, Fig. 7c.

Our analysis reveals real-space variation in the resonant energy of a monoclinic phonon, in the range of 601-617 cm^{-1}. Expanding on our earlier work, where we correlated shifts of the monoclinic phonon frequencies with known strain introduced by various substrates, (*42*) we hypothesize that the shift in the phonon-frequency arises from variations in the local strain. Within our hypothesis, compressive strain yields red-shifts of the phonon-frequency tensile strain yields blue-shifts. Our interpretation is, furthermore, in agreement with the observation that domains of metal are preferentially nucleated from regions where the phonon frequency is smaller, supporting the notion that these regions possess high compressive strain, see Fig. 10 (*42, 43, 74*).

Table 1: Parameters for the equilibrium dielectric function of VO_2:

	k=1; L=1	k=1; L=2	k=2; L=1	k=2; L=2	k=3; L=1	k=3; L=2
$E_{k,L}$ (cm^{-1})	617	601	701	701	734	734
$\gamma_{k,L}$ (cm^{-1})	37	32	121	105	102	89
$f_{k,L}$ (cm^{-2})	576	576	128	128	100	100

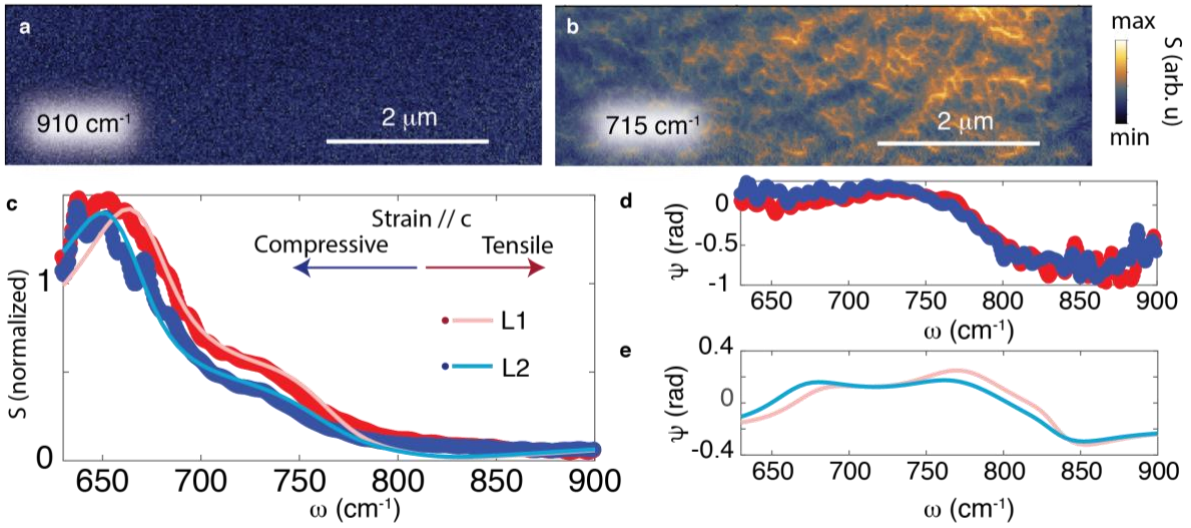

Fig. 7: a and b, Room temperature nano-infrared images of the VO_2 thin film at equilibrium. The probe frequencies a, 910 cm^{-1}, and b, 715 cm^{-1}, were used in this study. The scale bars are 2 μm in length. c, spectra of the near-field amplitude recorded at two different locations, L1 and L2. The solid lines are calculations using a Lorentz model for the dielectric function with the Lightning Rod formalism. The parameters used to model the dielectric function are reported in Table 1. d, Spectra of the nano-optical phase from the same dataset displayed in panel c. e, Lightning rod model calculation of nano-optical phase, ψ, with the parameters reported in Table 1.

2.4 Nano-texturing of the transient conductivity

We return to the transient, photo excited, IMT. To highlight generic trends that were reproducibly observed in wide array of data we focus on transient changes of the near-field amplitude at two locations at the extremes of compressive and tensile strain that we observed within our film in Fig. 8 a and b. First, we focus on the dynamics recorded with a pump fluence that is below the threshold for the $M_I \rightarrow R_M$ transition, F_c, Fig. 8a. Following an increase of ΔS at t_0, completely recovery of the near-field amplitude is observed at t_1. On the timescale of hundreds of picoseconds, t_2, an increase of the near-field amplitude is observed without any apparent fluence threshold. Dynamics of ΔS recorded after increasing pump fluence to just above the threshold of the $M_I \rightarrow R_M$ transition are displayed in Fig. 8b. Above the fluence threshold a finite value of ΔS persists at t_1 with a magnitude that is dependent on the real-space location of our measurement. The amplitude

increases further on the t_2 timescale at a rate, τ^{-1}, that depends on the real space location of the measurement, as we discuss in Chapter 2.5.

Next, we analyze spatial correlations between transient and static images of the VO_2 thin film. Nano-optical contrast, $-\psi$, which characterizes the local strain of our film (Fig. 8c) is compared with the transient near-field amplitude collected at time-delay of 203.6 ps, $S(t_2)$ (Fig. 8d). Adding the latter two images in the RGB representation allows us to visualize spatial correlations, Fig. 8e. To formally quantify correlations between these images we computed $\eta(x)$, Fig. 8f (methods). Our analysis shows that $S(t_2)$ is anti-corelated with $-\psi$ revealing that it is more probable to transiently attain higher metallicity in regions with larger compressive strain.

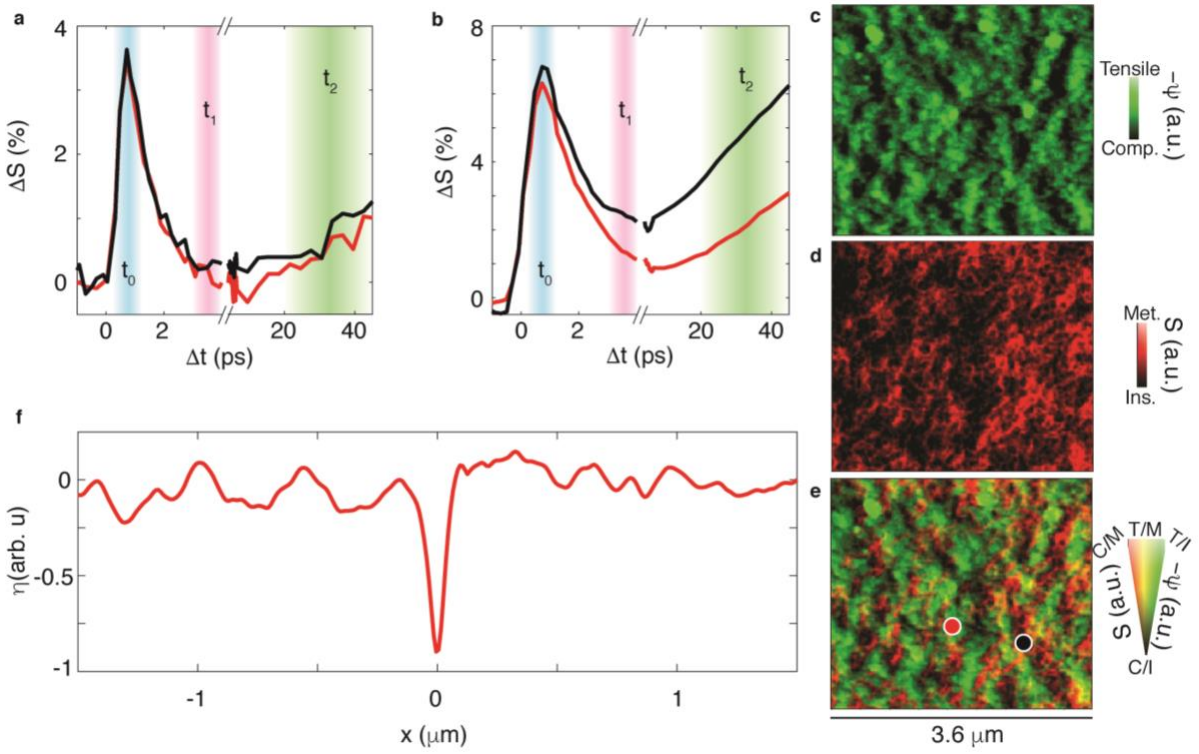

Fig. 8: Nanoscale spatially resolved dynamics of the IMT. a, Delay traces acquired at the probe frequency ω = 1000 cm^{-1} with a pump power of 2 mW, which is below the threshold of the monoclinic insulator to rutile metal phase transition. We display the pump-induced change of the near-field amplitude, ΔS, acquired at two locations of extreme compressive and

tensile strain (black and red curves respectively) with the locations indicated by the black and red dots in panel e. b, Identical to panel a, except we display data acquired with a 4.5 mW pump, which is slightly above the threshold required to initiate the monoclinic insulator to rutile metal phase transition. c-e, Co-located nano-optical images, which display: c, The phase contrast at equilibrium, -ψ, which shows regions of tensile strain (green) and compressive strain (black; abbreviated Comp. for brevity). d, Near-field amplitude at the pump probe time delay of Δt=203.6 ps (identical to Fig 1g). Within our color scheme a high degree of transient metallicity is represented with red (labeled Met. for brevity) while regions that retain lower transient conductivity regions are black (labeled Ins. for brevity). e, The images shown in panels c and d are added within the RGB scheme. Highly metallic and compressively strained regions (C/M) are red, highly insulating and tensile strained regions are green (T/I), highly metallic and tensile strained regions are yellow (T/M) and highly insulating and compressively strained regions (C/I) are black. While black, green and red are apparent the mixed color yellow is rarely observed. Thus, -ψ and S are highly anti-correlated in real space. All co-located images are 3.6 μm in length, as indicated by the scale bar. f, The absolute value of the correlation function, η(x), between the images of -ψ and S shown in panels c and d, that are displaced by a distance x.

2.5 Fluence dependent transient nano-imaging experiment

We proceed to the inquiry of fluence dependence of the spatially resolved dynamics. The position of the AFM probe was manually corrected for spatial drift at intervals of fifteen minutes to maintain a constant probe position, within +/- 40 nm, which was essential for this study. The dynamics of ΔS are well described by a bi-exponential fit at all locations and fluences, Fig. 9a. At time t_1 the near-field amplitude has changed by a fractional amount, S_{t1}, relative to the value of S recorded in equilibrium. A finite increase value of S_{t1} is only observed above a critical fluence threshold, F_c. The extracted value of F_c, however, depends on the location of our measurement, Fig. 9b. The further increase of S observed on the t_2 timescale rises with an exponential time constant, τ^{-1} (Chapter 2.7). The second, slow, growth process on the t_2 timescale is observed for excitation fluences well below F_c without any apparent fluence threshold. Heterogeneity of the rise time, τ^{-1}, observed on the t_2 timescale is furthermore apparent, Fig. 9c.

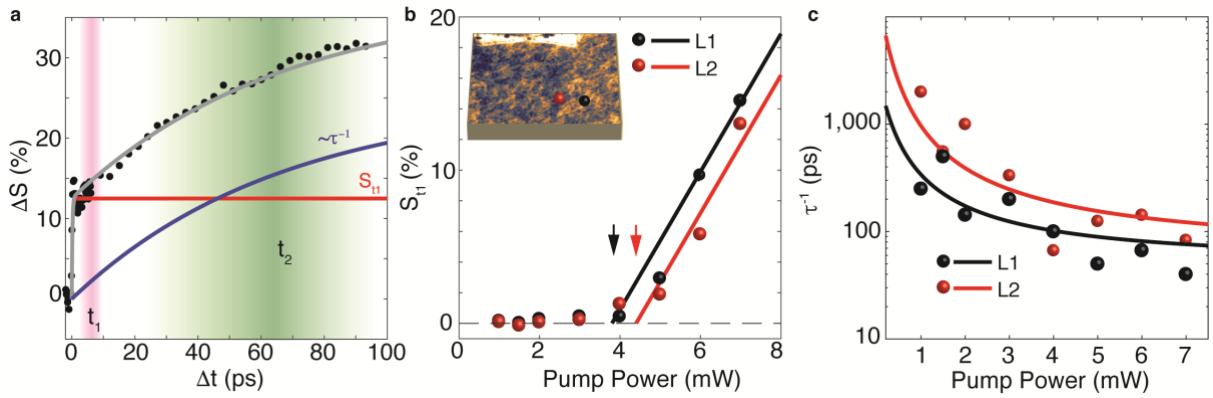

Fig. 9: Multiple pathways for the insulator to metal phase transition. a, dynamics of the change in near-field amplitude vs the pump probe time-delay are analyzed with a bi-exponential fit (Chapter 2.7). The near-field amplitude abruptly increases by a fractional amount S_{t1} with a time constant ~300 fs. On a much longer timescale with an exponential rise time, τ_{-1}, of tens to hundreds of picoseconds the near-field amplitude continues to grow. b, The value of S_{t1} measured at two locations, indicated by the red and black dots, is plotted against the applied pump power. The local values of the fluence threshold, F_c, are indicated with black and red arrows and reported in Table 2. c, Fluence dependance of the rise time, τ^{-1}. The black and red dots are data recorded at locations L1 and L2 (indicated in the inset of panel b) respectively while the solid black and red lines are calculated with Eq. (12) using the activation energies E_A of 200 and 250 meV respectively. The electron temperature was calculated in a free-electron heat capacity model as described in Ref. (*75*).

2.6 Summary of results

We summarize our findings in Table 2. The local transition temperature for the IMT was observed in the range of 338-348 K with a global transition temperature, $T_{c,global}$ = 342K. The phase diagram of VO_2 has been accurately determined on single crystals (*43*). Comparison with the latter phase digram implies that regions with $T_{c,local}$=338 K=$T_{c,global}$ - 4K posess a compressive strain of approximately -2x10^{-3}. At the opposite exterme regions with $T_{c,local}$=348 K=$T_{c,global}$ + 6K, likewise, possess a tensile strain of approximately 1x10^{-3}. The local variation of static nano-optical contrast observed at room temperature were in good agreement with a local resonance shift of the monoclinic phonon. The extracted phonon frequencies vary within a range of at least $\delta\omega$=16 cm^{-1} within our thin film (Tables 1 and 2).

Fluence dependance of the local dynamics (Fig. 9) exposes real-space variations of the parameters F_c and τ^{-1}. The fluence, F_c, characterizes a threshold above which a persistant change of S is observed to stabilize within four picoseconds after the photo-excitation event. Variation of the extracted value of F_c was observed within the range of 3.8 to 4.3 mW, which corresponds to an estimated fluence of 2.3 and 2.6 mJ/cm^2 respectively. The threshold behaviour is characteristic of the first-order behaviour of the $M_I \rightarrow R_M$ transition. Recalling that there is a strain-dependant variation of the local T_c, we can estimate the energy density that should be required to induce the $M_I \rightarrow R_M$ phase transition as $\Delta Q = \Delta H(x) + \int_{T_i}^{T_c(x)} C_p dT$ (*51*). Within the latter expresion, C_p is the lattice heat capacity. Thus, the thermal energy required to elevate the sample temperature to T_c must be added to the latent heat, $\Delta H(x) = T_c(x)\Delta S_{RM}$, to produce the $M_I \rightarrow R_M$ phase transition, where $\Delta S_{RM} = 3\ cal/(mol \cdot K)$ is the change in entropy from monoclinic insulator to rutile metal phase (*76, 77*). From the latter estimate we determine that ΔQ of 2.5 and 2.8 mJ/cm^2 must be added to the system to produce the $M_I \rightarrow R_M$ phase transition at locations of the extreme compressive and tensile strains reported in Table 2, respectively. The good agreeement between our estimate of ΔQ and the expermentally determined values of F_c supports the interpretation that F_c is the fluence threshold required to produce the $M_I \rightarrow R_M$ phase transition (*51, 78*). By patterning a nano-antenna on the surface of the thin film we were able to enhance the pump fluence above F_c only within a localized region of real space. The data presented in Fig. 11, therefore, directly reveal growth of a transient Rutile domain in real space and time.

The increase of ΔS on the t_2 timescale was observed at fluences well below F_c without any apparent fluence threshold and, therefore, cannot be caused by the $M_I \rightarrow R_M$ phase transition. One possible interpretation of our data, proposed in Refs. (*8, 75*), is that the t_2 dyanmics are associated

with an iso-structural monoclinic insulator to monoclinic metal ($M_I \rightarrow M_M$) phase transition. We note that several observations of the monoclinic metal phase at equilibrium have been recently published (*19, 79, 80*). Within the latter interpretation the fluence dependace of τ^{-1} may be described with the Eyring-Polanyi equation from transition state theory (*75, 81*):

$$\ln\left(\frac{h\tau^{-1}}{k_B T_e}\right) = -\frac{E_A}{k_B T_e} + \ln(A) \quad (12)$$

According to Eq. (12) heterogeneity of τ^{-1} could be accounted for by a real-space variation of the activaton energy, E_A, for the $M_I \rightarrow M_M$ transition. Together, heterogeneity of F_c and τ^{-1} govern the nanotexturing of the transient conductivity observed in our VO_2 thin film.

Table 2: Parameters extracted from the time-resolved nano-imaging experiment. Note that L1 and L2 denote regions of our VO_2 thin film where the extreme values of the reported parameters were observed i.e. the values were not determined at identical locations for all measurements. Local variations of transition temperature, T_c, were determined by nano-IR imaging and compared to the phase diagram in Ref. (*43*) to determine the strain variation throughout the thin film. The local values of the phonon frequency reported in Table 1 are compared to the average phonon-frequency of $\omega = 607$ cm^{-1} reported in Ref. (*73*) to determine the local variation of the phonon frequency, $\delta\omega$. Finally, the local values of the fluence threshold, F_c, were determined from the experimental data presented in Fig. 9.

Table 2: Inhomogeneous parameters within our vanadium dioxide thin film

	T_c (K)	Strain	$\delta\omega$ (cm^{-1})	F_c (mJ/cm^2)
L1	338	-2x10^{-3}	-6 [Ref]	2.3
L2	348	1x10^{-3}	+10 [Ref]	2.6

2.7 Experimental methods

For nano-optical imaging experiments, we used a scattering-type scanning near-field optical microscope (s-SNOM, Neaspec). The atomic force microscope (AFM) operates in tapping-mode with a frequency of about 70 kHz and an amplitude of approximately 70 nm. The time-resolved psuedoheterodyne technique is used to extract the amplitude (S) and phase (ψ) of the near-field signal in imaging experiments (*35*) while time-resolved nano-FTIR is used to extract spectra of S and ψ. The additive background contribution was strongly attenuated by considering only information modulated at the second or third harmonic of the tapping frequency of the AFM tip. The pump and probe channels derived from a 20 W; 1030 nm Yb:kGW amplified laser source operating at 750 kHz (Pharos, Light Conversion). The intense laser pulse was converted to two separate, pump and probe channels of radiation utilizing a difference frequency generation (DFG) scheme for the probe and picking off a fraction of the fundamental, 1030 nm, beam as the pump. The pulses were delivered to the Neasepc microscope with a well-controlled time delay, Δt, between their arrival controlled by a mechanical delay stage. For all data displayed in this chapter the center wavelength of the pump was fixed at 820 nm. The sample was held at the base temperature of T=330K and a pump with above band-gap frequency (ω_{pump}=9,700 cm^{-1}) was utilized for all data in this chapter, unless specifically indicated otherwise.

The dielectric response of VO_2 at equilibrium is modeled with a series of Lorentzian Oscillators:

$$\varepsilon_L \cong \varepsilon_{stat} + \sum_{k=1}^{N} \frac{f_{k,L}}{(E_{k,L})^2 - E^2 - iE\gamma_{k,L}} \quad (13)$$

The subscript L is used to indicate the location of measurement. The offset ε_{stat} = 4.5 was used and all other parameters are reported in Table 1.

To quantify correlations between two-dimensional images Y and Z we define the parameter η:

$$\eta = \frac{\sum_{i,j}(Z_{ij}-\bar{Z})(Y_{ij}-\bar{Y})}{\sqrt{(\sum_{i,j}(Z_{ij}-\bar{Z})^2)(\sum_{i,j}(Y_{ij}-\bar{Y})^2)}} \quad (14)$$

Where the images Y and Z are co-located. When the image Y is displaced by a distance x relative to the image Z, we form the function $\eta(x)$, which quantifies the distance over which correlations are lost.

The dynamics of the pump-induced change of the near-field amplitude are well described by a bi-exponential function:

$$\Delta S(\Delta t) = S_{t1}\left(1 - \exp\left(-\tau_{fast}^{-1}\Delta t\right)\right) + S_{t2}(1 - \exp(-\tau^{-1}\Delta t)) \quad (15)$$

In Eq. (15) the first exponential has a fixed rise time of $\tau_{fast\text{-}1}$=300 fs. We emphasize that the latter rise time is limited by the pump-probe convolution and, therefore, reflects our temporal resolution rather than the genuine rise time of the $M_I \rightarrow R_M$ phase transition. To extract the rise time of the second exponential, $\tau_{\text{-}1}$, we considered only data for $\Delta t > 1$ps. On the latter timescale the first term provides an offset which was subtracted before fitting.

2.8 Extended data

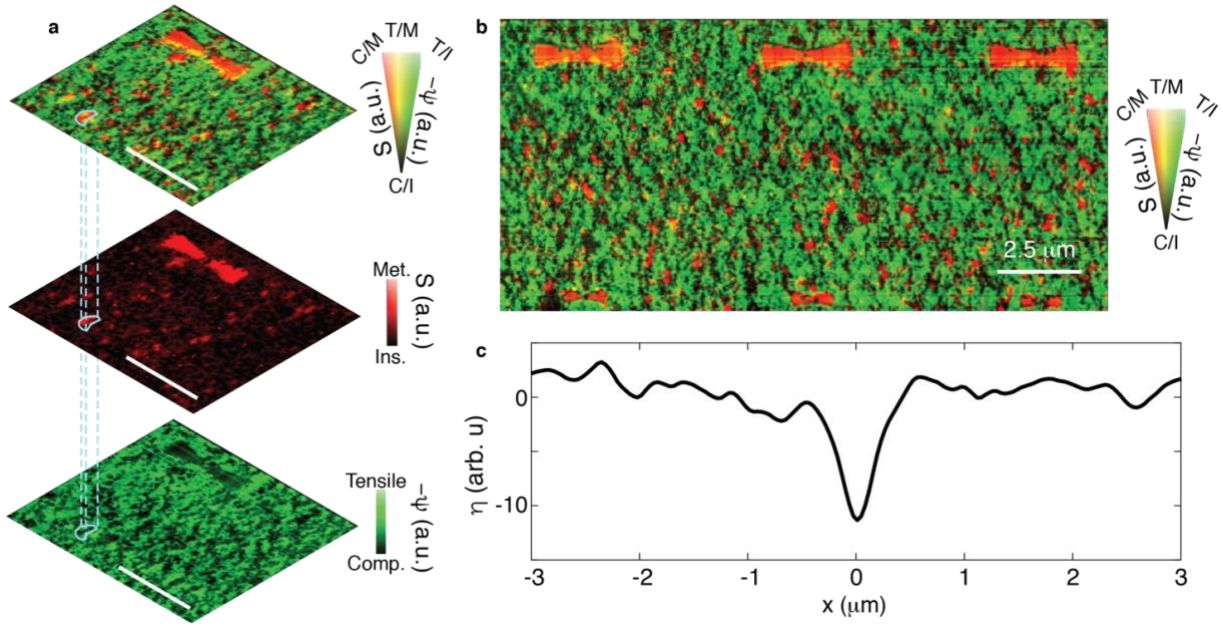

Fig. 10: a, From bottom to top: (bottom) near-field phase recorded at ω = 660 cm^{-1} at T = 335K, below the IMT transition temperature at all locations. Contrast between regions with tensile and compressive strain are represented with green and black respectively. (Middle) The near-field amplitude recorded at ω = 1000 cm^{-1} at T = 338K, where the IMT transition temperature is locally surpassed, shows contrast between metallic islands and the surrounding insulating regions represented in red and black respectively. (Top) The latter two images are added in the RGB scheme to visualize spatial correlations between images. Highly metallic and compressively strained regions (C/M) are red, highly insulating and tensile strained regions are green (T/I), highly metallic and tensile strained regions are yellow (T/M) and highly insulating and compressively strained regions (C/I) are black. The prominence of pure black as well as green and red colors, with few identifiable yellow regions, shows the strong anti-correlation between the co-located datasets. b, A large area image of the near-field phase and amplitude added in the RBG scheme. c, the degree of correlation between -ψ and S is quantified by the parameter η(x), a function of the displacement, x, between the images (methods). A strong anti-correlation peak at zero displacement is apparent. The scalebars in panels a and b are 2.5 μm in length.

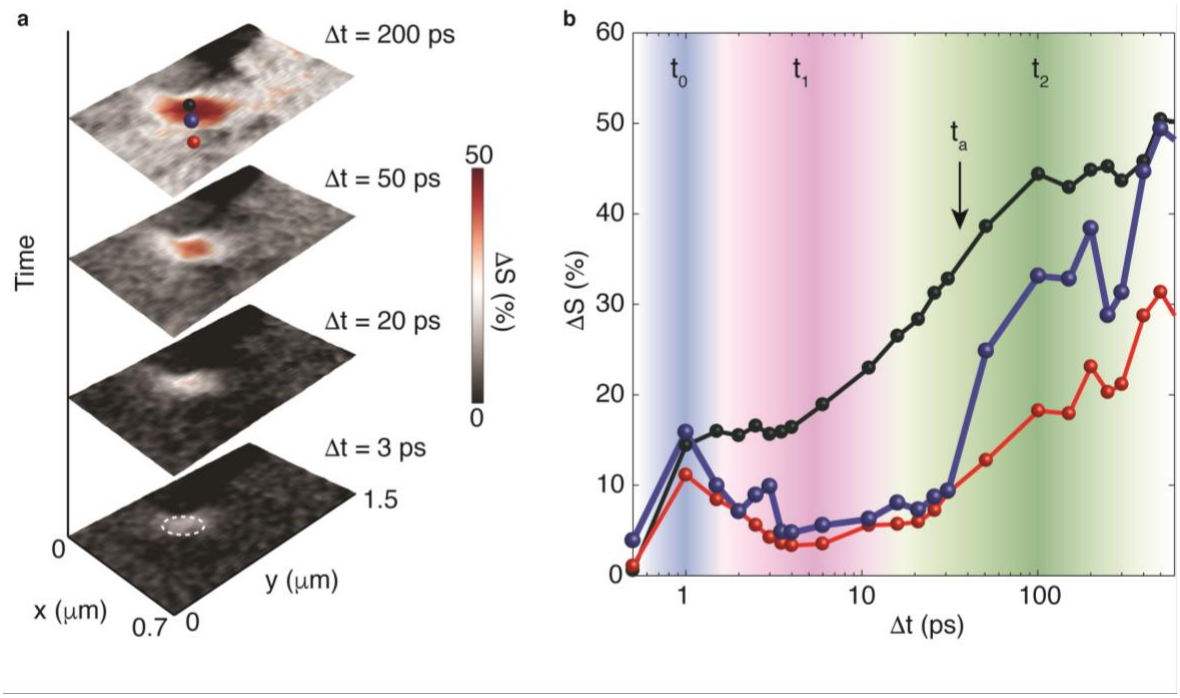

Fig. 11: Growth of a metallic domain. a, A series of images of the pump-induced change of near-field amplitude, ΔS, at several time delays, Δt, in the vicinity of a gold antenna. From bottom to top: data were collected at a series of pump-probe time delays, Δt=3 ps, Δt=20 ps, Δt=50 ps and Δt=200 ps. The antenna locally enhances the pump intensity bringing the energy density above the fluence threshold for the monoclinic-insulator to rutile-metal ($M_I \rightarrow R_M$) phase transition only within the dashed white circle, indicated at Δt=3ps. Thus, only VO_2 within the white circle is able to instantly undergo the $M_I \rightarrow R_M$ phase transition immediately following the photo-excitation event. As time progresses the Rutile domain grows in real-space. b, the change in near-field amplitude is plotted against the time delay between the pump and the probe at selected locations of real space indicated by the dots in panel a at Δt = 200 ps. The black curve is data taken within the white circle where the $M_I \rightarrow R_M$ transition occurs immediately. The red curve shows data taken within the interior of the film far away from the launcher. The blue curve is data taken approximately x_a = 100 nm away from the edge of the white circle. The rutile metal reaches the distance x_a at the time t_a. The enhanced conductivity of the rutile metal causes the abrupt increase of ΔS at t_a which is clearly observed in the blue curve of panel b.

Chapter 3: Ultrafast exciton dynamics in WSe_2 optical waveguides

Van-der Waals (vdW) atomically layered crystals act as optical waveguides over a broad range of the electromagnetic spectrum ranging from tera-Hertz to visible (*60, 63, 82-84*). Unlike common Si-based waveguide media, vdW materials are inherently tunable and permit radical changes of their optical properties using non-thermal stimuli including electrostatic gating (*85*) and photo-excitation (*83, 86-90*). Here, we demonstrate the tunability of waveguides for near infrared radiation by controlling the optical properties of a prototypical vdW semiconductor, WSe_2, with femtosecond (fs) light pulses. Using time-resolved scanning near-field optical microscopy (tr-SNOM) we visualized the electric field profiles of guided photons in real space and time. We observed light-driven changes of the optical phase, reaching π over ~5 μm of propagation length that are attained on fs time scales. The observed optical phase modulation is caused by large photo-induced changes of the index of refraction, exceeding $\Delta n=2.5\%$ of the equilibrium value. Our transient nano-imaging experiments and first-principles calculations implicate excitons in the observed light-induced dynamics and establish fundamental limits to tunability in vdW waveguides.

3.1 Exciton dynamics in a vdW waveguide

vdW crystals are emerging as an ultra-manipulatable platform for a variety of physical properties (*70, 91-93*) including guided photons (*60, 83*). It is customary to characterize waveguiding at equilibrium with the complex wavevector, $q_r=q_{1,r}+iq_{2,r}$. The real component of the wavevector, $q_{1,r}$, provides a measure of the phase velocity which is dependent on the index of refraction, n, of the medium; the imaginary component of the wavevector, $q_{2,r}$, characterizes the attenuation of guided photons. In this work we demonstrate the ability to control waveguide properties of a prototypical vdW crystal, WSe_2, on the fs time scale (Fig. 12a,b). The electrodynamics of vdW

semiconductors in the near-infrared and visible range are governed by excitons (*63, 94, 95*). Excitonic resonances yield absorptive and refractive spectral features that are likewise encoded in the complex wavevector q_r (*63*). Our data (Fig. 12-15) expose the rich transient response of WSe_2 and demonstrate the ability to dynamically tune waveguided radiation by manipulating the A-exciton resonance. Unprecedented fs dynamics of refraction, in close spectral proximity to the A-exciton, are observed and attributed to a coherent optical Stark shift (*87-89*). We detected massive optical phase modulation in WSe_2 (Δn_{WSe2} = 0.11 at E=1.45 eV) unaccompanied by changes of optical loss within the error bar of our measurement (Fig. 12c-e). Similar behavior was observed in WS_2 (Δn_{WS2} = 0.23 at E=1.45 eV) demonstrating that these effects are generic in vdW semiconductors (Fig. 25). The drastic changes of the complex wavevector of guided photons evident in our data in Figs.12-14 were neither detected or anticipated in earlier works (*83*). Our study establishes that excitons enhance optical modulation in vdW semiconducting waveguides.

To experimentally access and control waveguided photons in vdW crystals we utilize state-of-the-art time-resolved scattering near-field optical microscopy (tr-SNOM) (*28, 29, 31, 35, 83, 96*), Fig 12a. Here, the metalized tip of an atomic force microscope (AFM) is illuminated with p-polarized light. The evanescent field is confined at the tip apex with radius of curvature, *a*. The extreme confinement provides access to optical contrast with a = 20 nm spatial resolution, and momenta of $q \sim 1/a$, independent of the wavelength of probe radiation (*24, 36*). Monitoring the amplitude of the near-field scattering signal, S_r, (Chapter 3.2) along the surface of the crystal we observe a characteristic periodic pattern (Fig. 12b) (*63, 82, 97*). A representative line profile in the direction normal to the crystal edge (Fig. 12c-e) highlights periodic oscillations. These imaging data are consistent with the following scenario. The AFM tip launches a waveguide mode, which travels

in the bulk of the layered crystals. When the waveguide mode reaches the edge of the crystal after traveling the distance x from the AFM probe, the mode scatters to free space and reaches the detector. By measuring the near-field amplitude as a function of x, we visualize the electric field profile of the waveguide mode (Chapter 3.3) (*98*). Non-equilibrium data are obtained by illuminating the crystal with an s-polarized pump beam, with nearly homogeneous intensity across the scanned region (Chapters 3.3 and 3.8). In the photo-excited case, the complex momenta of the waveguided mode are altered. In this work, we focus on the response of WSe_2 because its A-exciton resonance lies in the frequency region that can be readily accessed with our tr-SNOM allowing us to fully characterize dynamics of excitons under intense optical pumping of this particular vdW waveguide.

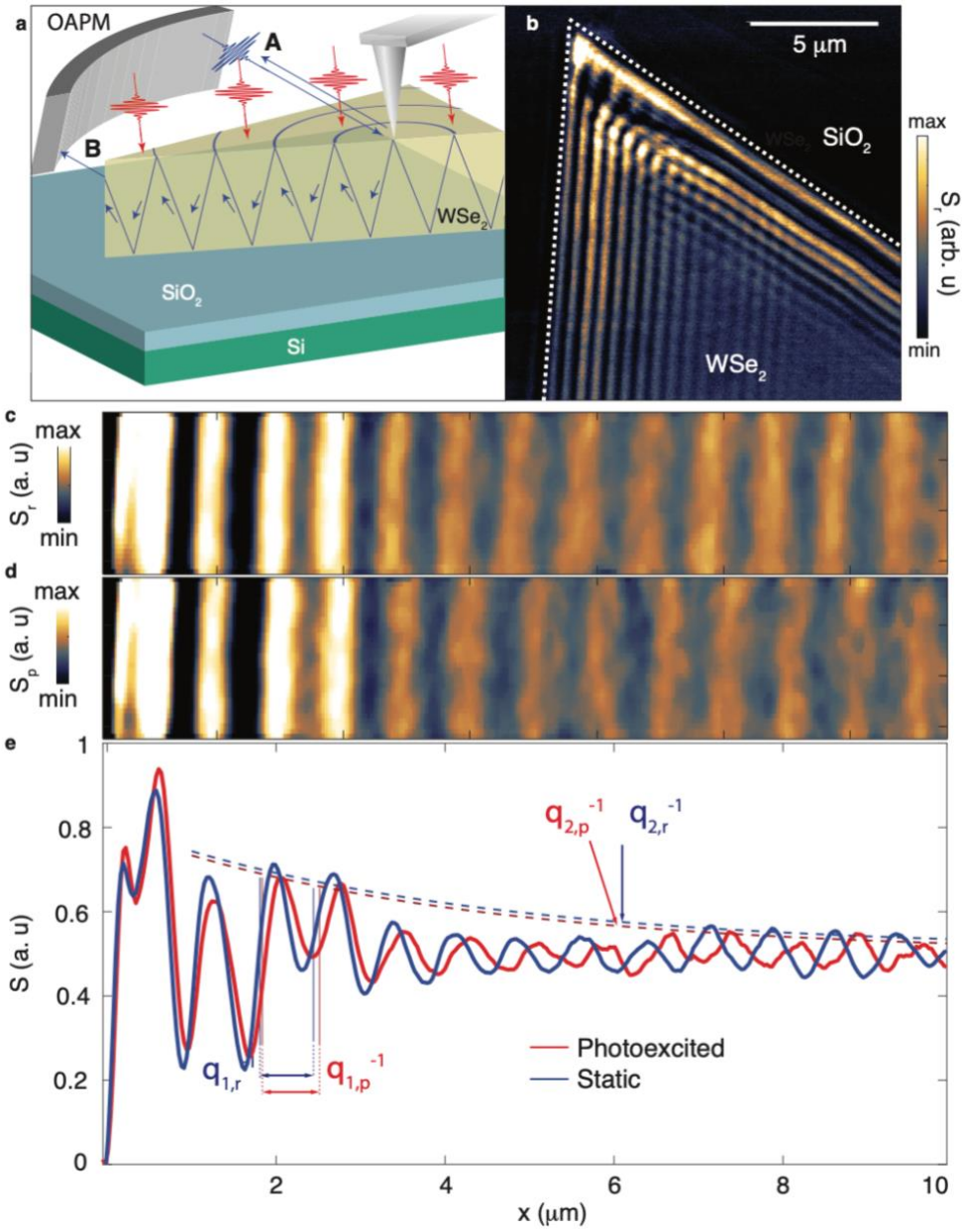

Fig. 12: Time resolved infrared nano-imaging experiments on WSe_2. a, Nano-imaging experiments are performed in a tr-SNOM set-up by shining probe radiation (purple) onto the apex of the AFM tip. Radiation back scattered from the tip-apex (beam A) is collected by an off-axis parabolic mirror (OAPM) and sent to the detector. Simultaneously with back scattering of beam A, waveguided photons are launched and travel in the WSe_2 crystal (yellow triangular slab) to the sample edge where they are scattered to free space (beam B). A second pump channel (red) homogeneously perturbs the sample and alters the propagation of waveguided photons. b, Image of the near-field amplitude, S_r, at the WSe_2/SiO_2 interface. The edge of the WSe_2 flake was determined from the topography and is indicated by the white dashed line. c, Image of the near-field amplitude, S_r, collected along the direction normal to the edge of a WSe_2 crystal at equilibrium conditions. Periodic oscillations visualize

the propagating waveguide mode. d, Image of the near-field amplitude, S_P, acquired with the sample in its photoexcited state at the time delay of Δt=1 ps. A pump with energy 1.58 eV and power 2.5 mW was applied to photo-excite the crystal. e, Averaging the 2D data of panels c, and d yields line cuts of the scattering amplitude recorded under equilibrium (blue) and photoexcited (red) conditions, respectively. The experimental traces were offset vertically for clarity. The periodicity of the oscillations is characterized by wavevectors $q_{1,r}$ and $q_{1,P}$ under equilibrium and photo-excited conditions, indicated by the blue and red horizontal arrows, respectively. The decay length of the waveguide mode is characterized by $q_{2,r}$ and $q_{2,P}$ under equilibrium and photo-excited conditions, indicated by the blue and red dashed lines, respectively. Panels b-e were collected with the probe energy, E=1.45 eV on a WSe_2 crystal with approximately 130 nm thickness.

We begin with the electrodynamics of WSe_2 at equilibrium. In Fig. 13a we display line profiles of the near-field amplitude collected with several probe energies, E. The experimental profiles exhibit oscillations (Fig. 13a) characterized by the complex wavevector, $q_r = q_{1,r}+iq_{2,r}$; the subscript r indicates that q_r is a "reference" recorded at equilibrium. The Fourier Transform (FT) of the line profiles, which were corrected for the angle of incidence (Chapter 3.4), reveal peaks located at $q_{1,r}$ (Fig. 13b). The energy-momentum (E-$q_{1,r}$) dispersion of the waveguide mode is plotted in Fig. 13d. The group velocity, $v_g(E) = \frac{1}{2\pi h}\frac{dE}{dq_{1,r}}$, is clearly dependent on the probe photon energy. The energy dependence of $v_g(E)$ is particularly evident in the vicinity of 1.61 eV where the electromagnetic response is dominated by the A-exciton (Fig. 13c,d). The dispersion of the waveguide mode is uniquely determined by the complex dielectric function, $\varepsilon=\varepsilon_1+i\varepsilon_2$, of the material (Fig. 13c) and is accurately represented with a series of Lorentz oscillators (Chapter 3.2) (*62*, *63*). The dispersion relationship calculated with the Lorentz model reproduces the experimental results supporting the excitonic interpretation of the dispersion anomaly.

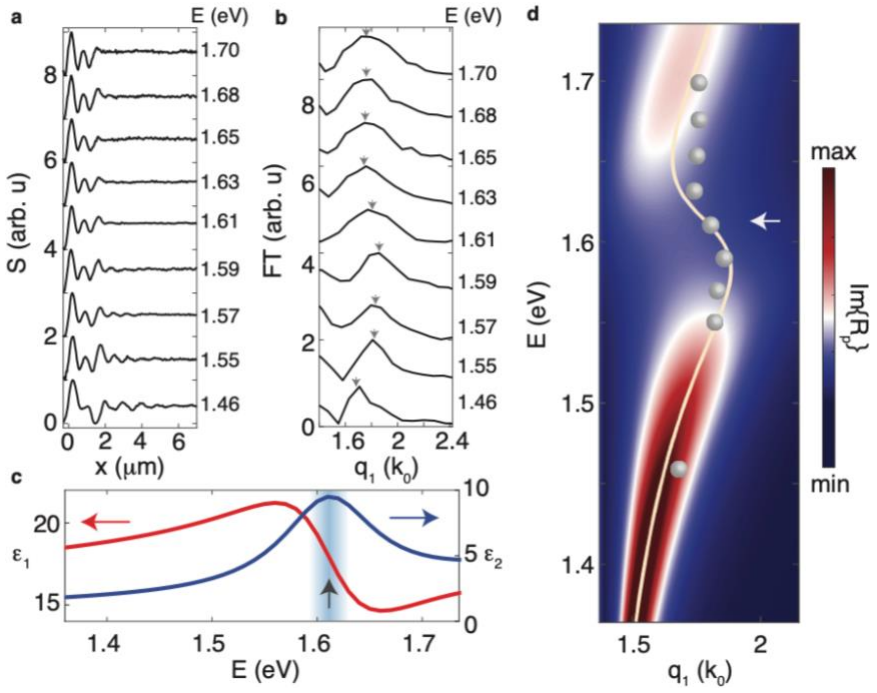

Fig. 13: Equilibrium electrodynamics of the WSe_2 crystal from nano-imaging. a, Near-field scattering amplitude at several probe energies plotted as a function of the real space coordinate relative to the edge of the 90 nm thick WSe_2 crystal. b, Fourier transforms of the data (panel a) are shown in units of k_0, the wavevector of light in free-space. The arrows indicate the real part of the dominant wavevector, $q_{1,r}$ (see Chapters 3.3-3.6). The data presented in panels a and b are offset vertically for clarity. c, The dielectric function of bulk WSe_2 (ε_1 shown in red, ε_2 shown in blue) obtained from the Lorentzian oscillators with parameters summarized in Table 4. The A-exciton energy, E_x, is indicated with a black arrow. d, The energy versus momentum dispersion of the waveguide mode corresponding to the dielectric function in panel c. The dispersion is represented with the imaginary component of the p-polarized reflection coefficient (false color map) along with the analytical solution (white line; Chapters 3.5 and 3.6). The experimental results for $q_{1,r}$ vs. E extracted from the data of panels a and b are displayed with gray dots. The energy E_x is indicated with a white arrow.

We now introduce a pump beam, as schematically shown in Fig. 12a, to interrogate light-induced effects of WSe_2 and their transient dynamics. The photon energy of the pump is chosen to be red-detuned by 50 +/- 8 meV from the A-exciton (Chapter 3.2). We fix the energy of the probe, at a 5 meV red-detuning relative to the center frequency of the A-exciton. We explore dynamics of the complex wavevector, $q_p=q_{1,p}+iq_{2,p}$; where the subscript p indicates that q_p is obtained the "photo-

excited" state (Chapter 3.2). Photoinduced effects are captured by the differential wavevector $\delta q_i = q_{i,p} - q_{i,r}$ where the subscript i=1,2 refers to the real and imaginary components of the wavevector respectively. Our analysis reveals an abrupt drop of q_2 ($\delta q_2 < 0$) and an equally prompt recovery all occurring within the first picosecond after the photoexcitation event (Fig. 14a). In other words, red-detuned photoexcitation transiently suppresses absorption and waveguide losses in the vicinity of the excitonic resonance. Suppressed dissipation within the duration of the pump pulse is a hallmark of coherent dynamics. In addition, incoherent photo-induced effects occurring over a timescale of several picoseconds ($\Delta t > 1$ ps) are also evident in the evolution of q_1 in Fig. 14b.

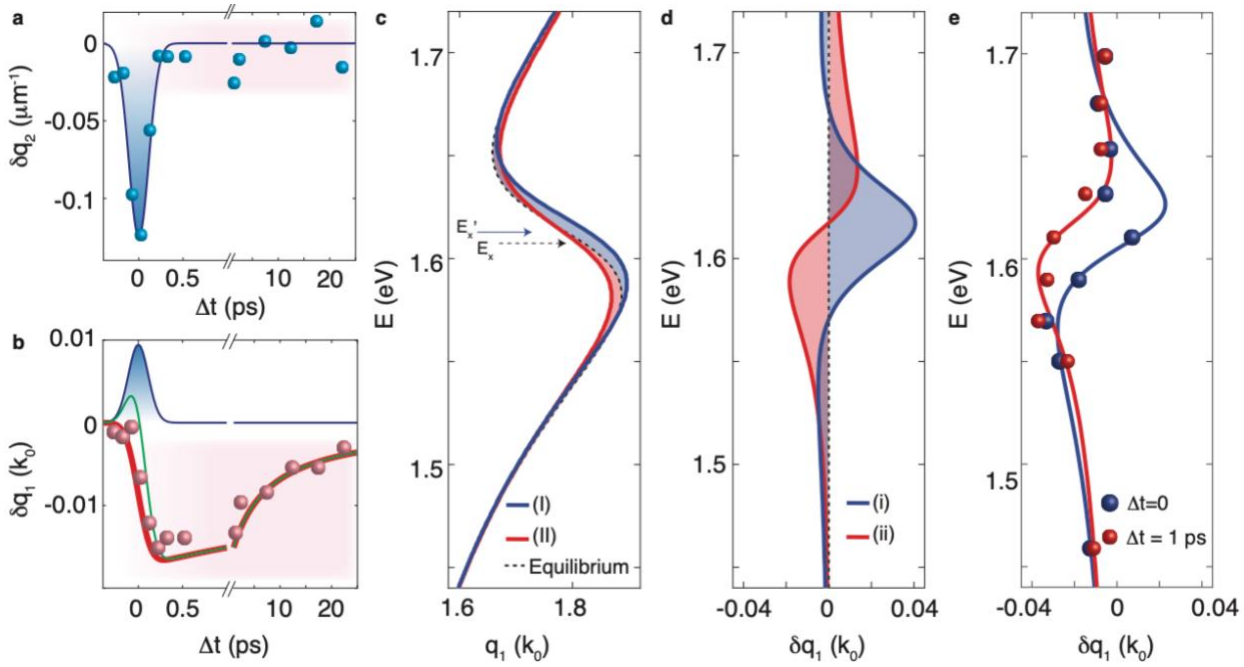

Fig. 14: Differential dispersion of the waveguide mode under non-equilibrium conditions. a, Values of δq_2 are displayed as a function of the pump-probe time delay, Δt. These data were collected with the probe energy E=1.61 eV on a 90 nm slab of WSe_2 photo-excited with a pump energy E=1.56 eV and pump power of 1.5 mW (see Fig. 19). The solid blue line is the gaussian function which indicates the pump-probe convolution (blue shaded region). b, Values of δq_1 are shown with red dots and are based on the same dataset used in panel a. The solid red line is calculated from an Auger model (see Chapter 3.11), while the blue solid line indicates the pump-probe convolution. The green line is the sum of the latter two functions. c, Lorentz model calculations of the dispersion relationship in equilibrium and non-equilibrium conditions (Chapter 3.10). The calculations show the equilibrium dispersion relationship (dashed black line) in the vicinity of the A-exciton, initially

at energy E_x, which is indicated with a black dashed arrow. A non-equilibrium blueshift of the A-exciton (*87*) to an energy E_x'=Ex+5 meV, indicated with a blue arrow, produces trend (I) (blue line). Bleaching of the A-exciton, defined as a decrease in the oscillator strength and/or increase in the spectral breadth produces trend (II) (red line). d, The differential dispersion is obtained from the calculations in panel c where $\delta q_1 = q_{1,p} - q_{1,r}$. The differential dispersion of the blue-shifted A-exciton (*87*) produces the trend (i) (blue line). The differential dispersion of the bleached A-exciton produces the trend (ii) (red line). e, The experimentally determined differential dispersion relationships are shown at two-time delays $\Delta t=0$ (blue dots) and $\Delta t = 1$ ps (red dots). The pump energy used for the data displayed in panel e is E=1.56 eV and pump power is 3 mW. The red and blue lines are Lorentz model calculations that show the best fits to our data with the parameters reported in Table 3. Bleaching of the A-exciton, trend (ii), is prominent in $\Delta t = 1$ ps data (red line), while a blue-shift of the A-exciton, trend (i), plays a dominant role in $\Delta t=0$ data (blue line). A linear decrease of $q_1(E)$, produced by the decrease of ε_{*stat}, is also included in the Lorentz model calculations at both time delays (Table 3).

We proceed with the inquiry into the non-equilibrium waveguide dispersion by varying the probe photon energy at fixed pump-probe time delay (Fig. 14c-e). We witness anomalies in the dispersion of δq_1 occurring on the fs timescale when the probe energy is in the vicinity of the A-exciton (Fig. 14e). In order to disentangle various transient mechanisms, we have chosen to describe the differential wavevector data with a model of the dielectric function constructed from a series of Lorentzian oscillators. The validity of this approach is attested by an accurate account of the equilibrium spectra of WSe_2 (Figs. 13, 22). To extract the transient dielectric function, we weakly perturbed the oscillators parameters (methods) and obtained a good agreement with the data. The above analysis reveals that features in the differential dispersion near the A-exciton are caused by two concomitant effects: i) a 5 meV blueshift of the A-exciton observed only at $\Delta t=0$; and ii) bleaching of the A-exciton, defined as spectral broadening, and/or a decrease in the oscillator strength observed at both $\Delta t=1$ps and $\Delta t=0$ (see Fig. 14d). Since trend (i) recovers within one picosecond the transient blueshift of the A-exciton resonance is consistent with a coherent light-induced process (*99*). Trend (ii) occurs on a much longer timescale and is, therefore, attributed to incoherent exciton dynamics. The dispersion analysis presented in Fig. 14 implicates the A-exciton in the observed photo-induced transformations. An overall decrease of the static

dielectric function, ε^*_{stat}, which stems from contributions of high-energy excitons outside of our frequency range and also from the response of a photo-excited electron-hole plasma (EHP) is also identified.

The coherent 5 meV blueshift of the A-exciton admits the interpretation within the framework of the optical Stark effect. The Stark scenario implies that eigenstates of the system are transiently modified under red-detuned photo-excitation. The Floquet formalism is a customary tool for describing the eigenstates of out-of-equilibrium time-periodic quantum systems (*87-89, 99, 100*). The latter formalism predicts a coherent blueshift of the excitonic resonance, in accord with spectral features we observe in Fig. 14e with zero time-delay between the pump and probe pulses (Table 3; Chapter 3.2). The eigenstates of the hybrid light-matter system were, therefore, found to govern the complex wavevector of the packet of probe photons.

We assign the incoherent response (ii) to Coulomb screening of the A-exciton due to a photo-induced EHP. Our interpretation is independently supported by the observation of a transient plasma edge in the mid-infrared spectral range under similar photo-excitation conditions (Fig. 23). The extracted density of itinerant carriers is near the threshold for the Mott transition. At the Mott threshold, the EHP screens the Coulomb interaction that binds excitons, which causes excitons to dissociate. As the EHP density approaches the Mott threshold, elastic scattering of excitons leads to spectral broadening of the excitonic transitions while screening of the Coulomb interaction suppresses the excitons' oscillator strengths (*85, 86, 90, 101, 102*). Both of these effects are manifest in trend (ii) above. The same physical mechanisms that produce trend (ii) are likely to influence high-energy excitons outside of our frequency range, which would impact the static

dielectric function, ε^*_{stat}. We comment that photoexcitation is likely to cause both Joule and electronic heating of the WSe_2 crystal, which results in spectral broadening of the A-exciton resonance (*103*). Heating, therefore, may partially contribute to our observation of trend (ii), but is unrelated to trend (i) occurring on much faster time scales.

Our transient images allow us to assess fundamental limits to excitonic vdW optical modulators. The magnitude of $\Delta n_{WSe_2}(E=1.45\ eV)$ reaches 0.11 in our experiments, which exceeds 2.5% of the value of the index at equilibrium (Fig. 12). The latter value of Δn may be used as an input to a common estimate of the modulator length required to attain π radians of phase shift, L_π (*104*). This estimate yields a value as short as $L_\pi = \lambda/(2|\Delta n|) = 4\ \mu m$, in agreement with the phase shift observed in raw images in Fig. 12. The data of Fig. 14 may be recast as the spectra of differential refractive index, $\Delta n(E)$, which are displayed in Fig. 15a. To assess the potential to exploit excitons in optical modulation applications we computed the excitonic contribution to the index of refraction, n_{EX}, from first-principles density functional calculations (see Chapters 3.2 and 3.10). Our first principles results provide an upper bound of refractive changes that would be attained provided all excitons in WSe_2 were to dissociate, $-\Delta n_X = n_{EX} = 0.6$, which is 13% of the value of the index at equilibrium (Fig. 15b). In this latter regime, L_π is further shortened down to the wavelength of free-space radiation. Apart from $|\Delta n|$, losses within the waveguide are of paramount importance for devices. Remarkably, additional losses are unobservable in our pump-probe data even under the strongest photo-excitation conditions. In fact, losses can be suppressed by photoexcitation as witnessed by the negative sign of δq_2 (see Fig. 14a), albeit over a restricted frequency region in the vicinity of the A-exciton (Fig. 15b). Notably, the magnitude of Δn_X is maximized near excitonic transitions, in the range of several eV, where added losses from itinerant carriers are exceedingly

small in WSe_2. These photo-induced changes establish unique virtues of optically-induced modulation in vdW semiconductors that are rooted in manipulation of excitons (*91, 104*). Provided that equilibrium loss governed by the excitonic linewidth is further reduced in WSe_2 and other vdW semiconductors, these systems can offer practical modulation solutions. Such a reduction of equilibrium loss is likely given observations of ultra-narrow exciton linewidths in high purity transition-metal-dichalcogenides (*105*) at liquid nitrogen temperatures. Finally, we stress that an encouraging degree of modulation is attained at fs time scales meeting the most stringent demands of ultra-fast optical circuits.

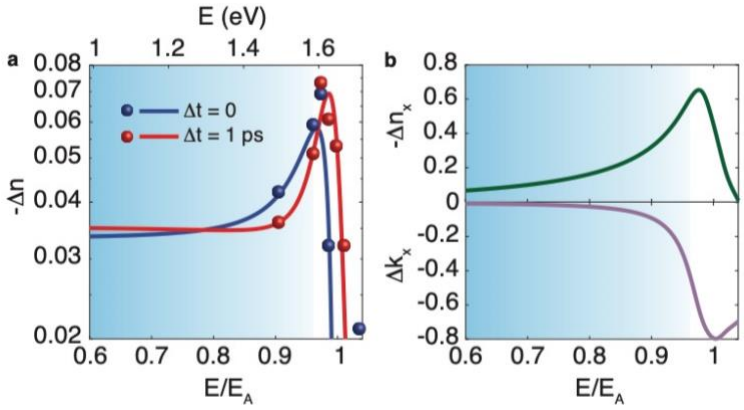

Fig. 15: Fundamental limits to excitonic optical modulators based on WSe_2. a, Experimentally determined change in the refractive index of a WSe_2 waveguide, Δn, under fixed pumping conditions (dots) and Lorentz model calculations with identical parameters to those displayed in Fig. 14e (solid lines). Data and Lorentz model calculations at the time delay of Δt = 0 and Δt = 1 ps are shown in blue and red respectively. b, The upper limit of the real and imaginary components of the refractive index attainable from changes of the excitonic response of WSe_2 waveguides at room temperature obtained from first principles theory (green and purple curves respectively; see Chapter. 3.10). The transparency window of WSe_2 is indicated by the blue shaded region in panels a and b.

Table 3: Parameters of the Lorentz model for the dielectric function of WSe_2

	f_1 (eV_2)	γ_1 (meV)	E_1 (eV)	ε^*_{stat}	$\delta\varepsilon_{stat}$	δN	δE (meV)
Equilibrium	1.2	106	1.612	17.5+2i	0	0	0
Δt=1 ps	1.2	106	1.612	17.5+2i	0.3	0.067	-0.5
Δt=0 ps	1.2	106	1.612	17.5+2i	0.28	0.065	5

3.2 Experimental methods

For nano-optical imaging experiments, we used a scattering-type scanning near-field optical microscope (s-SNOM, Neaspec). The atomic force microscope (AFM) operates in tapping-mode with a frequency of about 70 kHz and an amplitude of approximately 50 nm. The time-resolved Pseudoheterodyne technique is used to extract the amplitude (s) and phase (ψ) of the near-field signal (*35*) . In this chapter we discussed the amplitude, s. The additive background contribution was strongly attenuated by considering only information modulated at the third harmonic of the tapping frequency of the AFM tip. The pump and probe channels were derived from a 20 W, 1030 nm Yb:kGW amplified laser source operating at 750 kHz (Pharos, Light Conversion). The intense laser pulse was converted to two separate, pump and probe channels of visible radiation by employing two optical parametric amplifiers (OPAs). The broadband pulses were sent through bandpass filters (15 meV FWHM) before they were delivered to the Neasepc microscope. For all data presented in Chapter 3.1 the center energy of the pump was fixed at approximately 1.56 eV.

We collect the self-referenced and time-resolved near-field amplitude (*35*). Specifically, we acquire the near-field amplitude in the reference (S_r) as well as in the photo-excited state (S_p) simultaneously at each pixel using homebuilt software. The differential change in the near-field amplitude is calculated as $\Delta s=(S_p-S_r)/\langle S_r \rangle$ where $\langle S_r \rangle$ is the mean value of the reference near-field amplitude in the interior of WSe_2. The quantity Δs is used to extract differential changes in the complex wavevector as we describe in the Supplementary Materials. The samples studied here are WSe_2 planar waveguides. The high quality WSe_2 crystals were synthesized by self-flux method, then mechanically exfoliated onto an SiO_2/Si substrate (*106*).

A Lorentz model is used to approximately describe the dielectric function of WSe_2:

$$\varepsilon \cong \varepsilon^*_{stat} - \delta\varepsilon_{stat} + \frac{f_1(1-\delta\mathrm{N}\cdot\mathrm{C})}{(E_1+\delta\mathrm{E})^2-E^2-iE\gamma_1(1+\delta\mathrm{N}\cdot(1-\mathrm{C}))} \qquad (16)$$

In this expression the parameters f_1, γ_1, E_1 represent, respectively, the oscillator strength, spectral breadth and center frequency of the A-exciton respectively at equilibrium. The parameter ε^*_{stat} represents the static dielectric function, which absorbs contributions from high-energy (B, C, D, etc.) excitons as well as contributions from interband optical transitions (see Chapter 3.10). The remaining parameters represent changes to the dielectric function in the non-equilibrium situation. The parameter $\delta\varepsilon_{stat}$ represents a change in the static dielectric function. The parameter δE represents a shift of the center frequency of the A-excitons while δN represents a change in the oscillator strength and/or spectral breadth. Finally, C determines the relative value of the change in oscillator strength vs. a change of the spectral breadth. An arbitrary choice of this parameter on the interval [0,1] provides an adequate fit to our experimental data. Values for these parameters, that are extracted from the measurements reported in Fig. 14 and 15, are given in Table 3.

3.3 Modeling the near-field amplitude

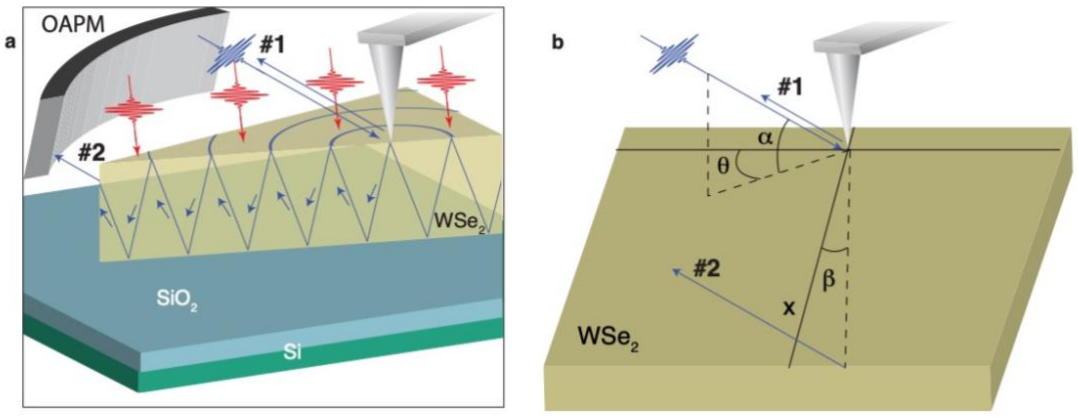

Fig. 16: a, Schematic of the experiment. Silver tip represents the AFM with a radius of ~20 nm at the apex. Yellow triangular slab denotes the WSe_2 crystal. Red and purple pulses indicate the pump and probe radiation, respectively. b, Geometry of the experiment. The incoming probe light is indicated with the purple pulse. Two possible beam paths for the scattered light, labeled #1 and #2 are indicated with purple arrows.

It is instructive to, first, consider the case that a monochromatic continuous wavelength (CW) light source with frequency, $\omega = \omega_0$, interacts with the tip/sample system (*48*). Subtleties imposed by broadband sources, which are necessarily employed in time-resolved experiments, are discussed in Chapter 3.12. In our experiments we illuminate a large area surrounding the AFM tip with pump and probe radiation (Fig. 16). Optical contrasts from the near-field are isolated from background radiation using the time-resolved psuedoheterodyne technique (*35*). At equilibrium the laser beam #1, with electric field $E_{1,r}$, is backscattered from the AFM tip. Simultaneously, a photonic waveguide mode is launched with the complex wavevector, $q_r = q_{1,r} + iq_{2,r}$ (see Chapter 3.5) and travels within the WSe_2 crystal (*63, 82, 97*). The beam following path #2 is scattered from the edge of the WSe_2 crystal. Both of the scattered beams, #1 and #2, reach our detector. We consider the electric field at the position x relative to the location of the AFM tip:

$$E_{k,r}(x,t) = C_{k,r}(x)\exp\left[-q_{2,r}x\right]\exp\left[i\left(q_{1,r}x - \omega_0 t\right)\right] \qquad (17)$$

The subscript k is used to indicate the beam path, k = 1, or 2. Beam path #1 (k = 1) is scattered from the AFM probe at x = 0. The waveguide mode, which travels along beam path #2 (k = 2), is also scattered to the detector after traveling a distance x. The near-field amplitude that is detected in our experiments can be written as (*63*):

$$S_r(x) \propto abs[E_{2,r}(x) + E_{1,r}(0)] \text{ (x>0)} \qquad (18)$$

The waveguide mode propagates away from the AFM probe and decays as $C_{2,r}(x) = C_2/\sqrt{x}$. We assume that the amplitude of the waveguide mode is small, $C_{2,r} \ll C_{1,r}$. Indeed, the efficiency of

launching the waveguide modes is low and the intensity decays with increasing distance (*107*). Then it is straightforward to expand Eq. (18) as:

$$S_r \cong \frac{C_2}{\sqrt{x}} \exp\left[-q_{2,r}x\right] \cos\left(q_{1,r}x + \varphi\right) + C_{1,r} \quad (19)$$

In our experiments, photoexcitation is utilized to perturb the properties of a WSe_2 crystal. The pump beam has an elliptical cross-section with the calculated semi-minor and semi-major axes of 9 μm and 16 μm respectively. Thus, the pump intensity is nearly homogeneous over the sub-10 μm fields of view investigated in our work. The pump beam is, furthermore, chosen to have horizontal polarization, which couples weakly to the AFM probe resulting in minimal distortion of the electric field at the tip apex (*28*). In our modeling we assume that the coefficient for the amplitude, $C_{2,r} = C_{2,p} = C_2$, and phase factor, φ are unchanged by photo-excitation, while the wavevector is modified:

$$S_p \cong \frac{C_2}{\sqrt{x}} \exp\left[-q_{2,p}x\right] \cos\left(q_{1,p}x + \varphi\right) + C_{1,p} \quad (20)$$

The pump-induced change in near-field amplitude is readily calculated:

$$\Delta S = S_p - S_r = \frac{C_2}{\sqrt{x}} \left(\exp\left[-q_{2,p}x\right] \cos\left(q_{1,p}x + \varphi\right) - \exp\left[-q_{2,r}x\right] \cos\left(q_{1,r}x + \varphi\right)\right) - \delta c \quad (21)$$

where the change in near-field amplitude in the interior of the sample is given by $\delta c = C_{1,p} - C_{1,r}$. We re-write the complex wavevector under photo-excitation as $q_{i,p} = q_{i,r} + \delta q_i$ to highlight the

pump-induced change to the complex wavevector, δq_i. The subscript i is used to indicate the real or imaginary component of the complex wavevector, i = 1, or 2 respectively. In the specific case that the pump-induced change to the complex wavevector is small, $\delta q_i X \ll 1$ we may expand Eq. (21). Where X is the largest distance from the edge of WSe_2 where we investigate the waveguide mode. X ranges from 2-10 μm in our work. If this signal is normalized such that C_2=1 it can be easily verified that to the leading order:

$$\Delta S + \delta c \cong \sqrt{x}\exp\left[-q_{2,r}x\right]\left(\delta q_1 \sin\left(q_{1,r}x+\varphi\right) - \delta q_2 \cos\left(q_{1,r}x+\varphi\right)\right)$$
$$= \sqrt{x}\exp\left[-q_{2,r}x\right]\sqrt{\delta q_1^2+\delta q_2^2}\cos\left(q_{1,r}x+\varphi+y\right) \qquad (22)$$

with

$$y = tan^{-1}\left(\frac{\delta q_1}{\delta q_2}\right) \qquad (23)$$

We emphasize that φ, $q_{1,r}$, and $q_{2,r}$ can be determined from the measurement of S_r in equilibrium. Two unknown quantities remain to describe the line profiles of ΔS: the amplitude of the oscillations, $A \propto \sqrt{\delta q_1^2+\delta q_2^2}$, and the relative phase difference, $y = tan^{-1}\left(\frac{\delta q_1}{\delta q_2}\right)$. These two experimentally determined quantities, amplitude and phase, may be used to determine the two desired components of the differential wavevector, δq_1 and δq_2. Therefore, in our approach we have the full set of information needed to quantify pump-induced changes to the complex wavevector from raw data of ΔS, bypassing a Fourier Transform analysis. Importantly

measurements of S_r and ΔS are carried out simultaneously (*35*) minimizing the error in our procedure.

3.4 Angular corrections of the wavevector

Fig. 16 shows the propagating waveguide mode that is detected by near-field imaging. Fringes are observed with a wavelength of λ_{obs} due to the interference of the electric fields E_1 and E_2, produced by beam paths #1 and #2 in Fig. 16b (Chapter 3.3). The in-coming laser beam is focused to the apex of the tip with incident angles α and θ with respect to horizontal plane and sample edge respectively. Laser beam #1 is back-scattered directly by the tip and registered on the detector. The tip also launches a waveguide mode which travels to the sample edge and scattered out as beam #2. Momentum conservation along the sample edge requires that the traveling direction of the waveguide mode makes an angle β with respect to normal direction of sample edge, which satisfies the following momentum conservation equation:

$$\frac{2\pi}{\lambda_p}\sin(\beta) = \frac{2\pi}{\lambda_0}\cos(\alpha)\cos(\theta) \qquad (24)$$

$$\beta = \sin^{-1}\left(\frac{\lambda_p}{\lambda_0}\cos(\alpha)\cos(\theta)\right) \qquad (25)$$

where λ_p and λ_0 are the wavelengths of the waveguide mode and free-space light respectively. In our set-up the angle α is fixed at approximately 30°. The two beams accumulate a relative phase difference, $\Delta\phi$, as the waveguide mode travels in WSe_2. The difference in the emission position of the scattered light satisfies:

$$\Delta\phi = \frac{2\pi}{\lambda_p}\frac{x}{\cos(\beta)} - \frac{2\pi}{\lambda_0}\cos\left(\frac{\pi}{2} - \theta - \beta\right)\frac{x}{\cos(\beta)}\cos(\alpha) \quad (26)$$

where x is the distance between the tip and sample edge. Thus, $\Delta\phi = \frac{2\pi}{\lambda_{obs}} x$ and

$$\lambda_{obs} = \lambda_p \left(\frac{1}{\cos(\beta)} - \frac{\lambda_p}{\lambda_0} \frac{\cos(\alpha)\sin(\beta+\theta)}{\cos(\beta)} \right)^{-1} \qquad (27)$$

is the wavelength observed in a near-field imaging experiment. In the perpendicular configuration $\theta = 90°$ and $\beta = 0$. The observed oscillation wavelength is given by, $\lambda_{obs} = \lambda_p \left(1 - \frac{\lambda_p}{\lambda_0}\cos(\alpha)\right)^{-1}$. Thus, our formulas reduce to a form that is in good agreement with previous reports (*63*). We recognize that the observed wavevector $q_{obs} = 1/\lambda_{obs}$ must be corrected for angle of incidence using Eq. (27) to extract the angular corrected wavevector of the waveguide mode $q_{1,l} = 2\pi/\lambda_p$. The subscript l = r, or p indicates the reference and photo-excited wavevector respectively.

We now present data taken to experimentally test the model of angular correction described above. In Fig. 17a we show the near-field scattering amplitude as a function of the real space co-ordinate, x, relative to the edge of the flake at x = 0. The measurement is repeated on the same flake for a series of different angles of incidence. The Fourier transforms of these data are shown in Fig. 17b. A maximum at $\lambda_{obs\text{-}1}$, is observed in the Fourier transform. The observed wavevectors of the TM_0 mode are marked with the black arrows. The observed wavelength is plotted against the angle, θ, in Fig. 17c. The solid line is produced with Eq. (27) using λ_p=470 nm, which is the angular corrected wavelength of the waveguide mode. Good agreement with Eq. (27) is established with the data presented in Fig. 17.

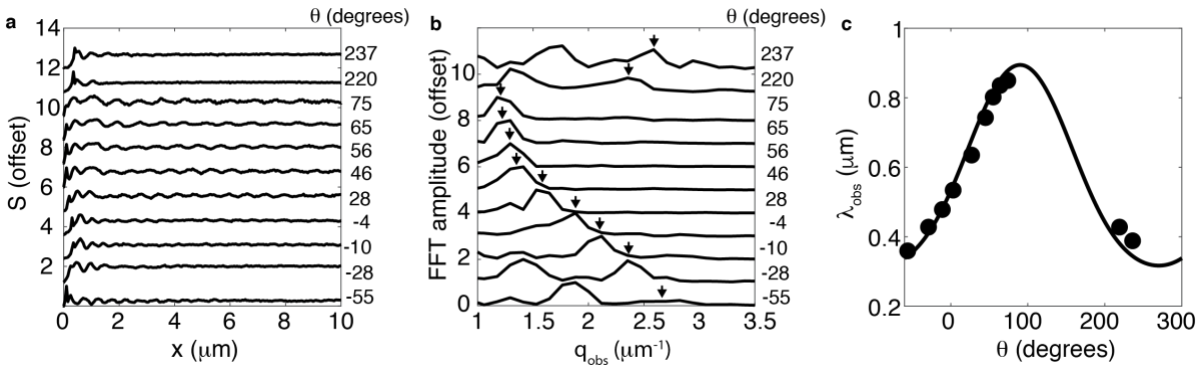

Fig. 17: Angle dependence of the polaritonic wavevector. a, Raw data taken on a 90 nm WS_2 flake on Al_2O_3 substrate with the probe energy of E=1.46 eV after rotating the sample at a series of angles, θ. b, Fourier transforms of the data in panel a. The arrows indicate the real component of the observed q-vector, q_{obs}. c, The observed wavelength of the waveguide mode extracted from the Fourier transform analysis is shown at a series of probe angles. The solid line is a fit using Eq. (27).

For the configuration used in the main text, $\theta \cong 55 +/- 5°$. In our modeling we applied Eq. (27) directly to extract the wavevector, $q_{1,l}$=2π/λ_p, from the raw data where the subscript l = r, or p indicates if the data were collected at equilibrium or under photo-excited conditions, respectively. In the main text the Fourier transforms of the raw data (Fig. 17b) are displayed in angular corrected units where we mapped the value of q_{obs} to $q_{1,l}$ at each point of frequency space using Eq. (27). The latter, angle-corrected wavevector, is displayed and compared with calculation throughout the main text and supporting information. The imaginary component of the wavevector, presented in Fig. 14a, was not corrected for angle of incidence.

3.5 Relationship between q-vectors and the dielectric function

In this Section we establish the quantitative relationship between the q-vector of the waveguide mode and the dielectric function of the sample/substrate system. To calculate the dispersion relationship of the waveguide mode we utilize Eq. (28), which was derived in Ref. (*82*). Here we quote the result that TM modes satisfy the transcendental equation:

$$\sqrt{\frac{\varepsilon_{ab}}{\varepsilon_c}}\sqrt{\varepsilon_c k_0^2 - q^2}d = tan^{-1}\left(\frac{\sqrt{q^2-\varepsilon_{sub}k_0^2}\varepsilon_{ab}}{\sqrt{\frac{\varepsilon_{ab}}{\varepsilon_c}}\sqrt{\varepsilon_c k_0^2-q^2}\varepsilon_{sub}}\right) + tan^{-1}\left(\frac{\sqrt{q^2-k_0^2}\varepsilon_{ab}}{\sqrt{\frac{\varepsilon_{ab}}{\varepsilon_c}}\sqrt{\varepsilon_c k_0^2-q^2}}\right) + n\pi \qquad (28)$$

where $\varepsilon_{ab} = \varepsilon_1 + i\varepsilon_2$ is the complex dielectric function in the plane of the WSe_2 crystal, while ε_c is the complex dielectric function in the c-axis of WSe_2. The wavevector of the infrared radiation in free space is k_0, and the sample thickness is d. The sample is surrounded by air and a substrate with dielectric function ε_{sub}.

In our experiments we consider the case of small light-driven perturbations altering the material properties. In the case that $\varepsilon_{ab} \to \varepsilon_{ab} - \delta\varepsilon_{ab}$, the wavevector will satisfy Eq. (28) with $q \to q - \delta q$. It is straightforward to show that:

$$\delta q \cong \kappa \cdot \delta\varepsilon \qquad (29)$$

in the limit $\delta\varepsilon \ll \varepsilon$. Thus, small perturbations of the wavevector reveal an approximate linear relationship with the dielectric function. The coefficient, κ, depends on the probe energy, sample thickness, equilibrium dielectric constant of the sample and environment. We numerically calculate the value of κ with the aid of Eq. (28) to determine changes in the dielectric function of WSe_2 from our measurements of the complex wavevector.

3.6 Equilibrium spectroscopy

We proceed to discuss data and calculations of the energy-momentum (E vs q) dispersion relationship at equilibrium. The raw data of our experiment (Fig. 18a) are Fourier transformed to produce traces in Fig. 18b. The maxima of each peak in the Fourier transform (FT) correspond to

the observed wavevector, $q_{obs} = \lambda_{obs-1}$ (Chapter 3.5) of a waveguide mode (red and black dots). Two peaks are observed in FT traces. We extract the real part of the wavevector, $q_{1,r}$, from the peak positions of the FT while the imaginary component of the wavevector, $q_{2,r}$, is proportionate to the full width half maximum of the peak (*63*). The experimentally determined wavevectors are corrected for the angle of incidence, as described in Chapter 3.4, and plotted in Fig. 18. The low frequency mode (red dots) is in reasonable agreement with the trivial "air mode" with wavelength equal to that of radiation propagating in free space with $\lambda_p=\lambda_0$, consistent with previous reports (*82*). We emphasize that the observed wavelength of the air mode is given by $\lambda_0 \left(\frac{1}{\cos(\beta_0)} - \frac{\cos(\alpha)\sin(\beta_0-\theta)}{\cos(\beta_0)}\right)^{-1}$ where $\beta_0 = \text{asin}\left(\cos(\alpha)\cos(\theta)\right)$ (see Eq. (27) Chapter 3.4). Excellent agreement between the observed dispersion of the high frequency waveguide mode (black circles) and the calculated dispersion of the TM_0 waveguide mode that propagates in the WSe_2 crystal is evident in Fig.18, as we discuss in detail in the next paragraph. The air mode is inevitably mixed with the TM_0 waveguide mode in the real-space fringe profiles. Nevertheless, the air mode is well separated from the TM_0 waveguide mode in the frequency domain, which allows us to separate these two modes. Furthermore, photoexcitation is only observed to impact the wavevector of the TM_0 waveguide mode. As such, we neglect the air mode in our analysis. After extracting the values of $q_r = q_{1,r} + iq_{2,r}$ from the FT analysis (Fig. 18b) the wavevector of the TM_0 mode, q_r can be used to fit the real-space line profiles of nano-imaging data (Fig. 18a). Utilizing Eq. (19) we produce the solid red lines in Fig. 18a with the phase of the waveguide mode, φ, as the sole fit parameter. Thus, we are able fully characterize the q-vectors and phase of the TM_0 waveguide mode in equilibrium.

The imaginary part of the momentum-dependent reflectance co-efficient, $Im\{R_p\}$, governs the dispersion relationship of the WSe_2 crystal and uncovers the parameter space for light propagation within the sample/substrate system. We display calculations of $Im\{R_p\}$ in Fig. 18c obtained using the Lorentz model for the dielectric function of WSe_2 (Chapter 3.10). Defining $2\pi k=q_1$ and using the known index of refraction of the SiO_2 substrate, $n_{SiO2}=1.46$ we highlight three features, which are apparent in the calculations shown in Fig. 18: (1) A straight line with the slope $c = E/(hk)$ (green line); (2) A straight line with the slope $c/n_{SiO2} = E/(hk)$ (light blue line); (3) A third maximum is observed at still higher momenta with group velocity $(dE/d(hk))$, which is clearly dependent on the probe energy. We overlay the analytic solution for the dispersion of the TM_0 waveguide mode, Eq. (28), on the $Im\{R_p\}$ calculations (white line). The above trends in the dispersion relationship are identical between the two calculation methods. The feature (3) is, therefore, assigned to TM_0 waveguide modes that propagate through the slab of WSe_2, which are the focus of the main text.

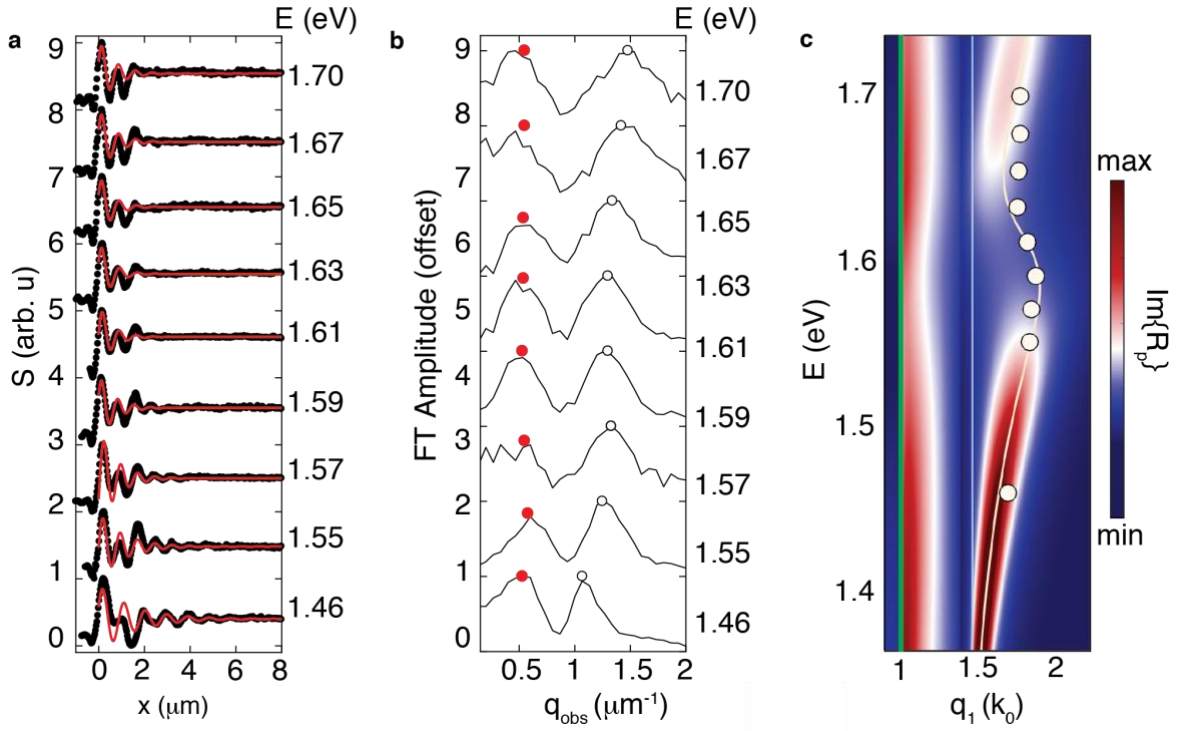

Fig. 18: Equilibrium dispersion relationship. a, Near-field amplitude at several probe energies plotted as a function of real-space position relative to the edge of the WSe_2/SiO_2 interface. The WSe_2 crystal is 90 nm thick. The solid red lines are fits to Eq. (19). b, Fourier transforms of the data shown in panel a. The curves displayed in panels a and b are vertically offset for clarity. The red dots indicate the dominant wavevector of the air mode. The black circles indicate the dominant wavevector, $q_{1,r}$, of the TM_0 waveguide mode, which propagates in WSe_2. c, The imaginary component of the p-polarized reflection coefficient is shown by the false color map as a function of frequency and momentum. The dispersion relationship calculated analytically using Eq. (28) is displayed with the white line. The calculations were produced with the Lorentz model for the dielectric function (Chapter 3.10). The green and light blue lines indicate the light cones of air and SiO_2 respectively as described above. The trend of $q_{1,r}$ vs. ω from the data (black dots with white interior) are overlaid.

The interaction of the waveguided probe radiation with excitons in the WSe_2 crystal is manifest in the frequency dependence of the group velocity of the waveguide mode (Fig. 18). We emphasize that the dielectric function of bulk WSe_2 is highly anisotropic but remains positive throughout the investigated range of the electromagnetic spectrum (*62*) (1.45-1.8 eV). In the case that the real part of the permittivity is positive, the iso-frequency surface of the anisotropic crystal is a closed ellipse. Abbe's law of diffraction applies to such a system and the q-vectors of the waveguide mode

consequentially reside within the material's light cone (*108*), which is in good agreement with our experimental results.

3.7 Transient dynamics of the complex wavevector

Raw data for the time-dependence measurements (Fig. 18 of the main text) are presented in this Section. The center frequency of the probe is red-detuned by approximately 5 meV from the center frequency of the A-exciton. In Fig. 19 we report the dynamics of the near-field amplitude in the non-equilibrium case, $S_p(\Delta t)$, where Δt is the time-delay between the pump and probe pulses. In Fig. 19a, we display the pump-probe data collected at a time delay, Δt = -70 fs, along with a reference trace (Chapter 3.6) for comparison. The minus sign indicates that the peak of the pump intensity arrives at the sample 70 fs after the maximum of the probe intensity. We emphasize that the pump-probe convolution, approximately 160 fs, is much longer than 70 fs. At the time delay Δt = -70 fs the pump-intensity is, therefore, finite but not at its maximum value. The line profiles obtained for the photo excited and reference cases both reveal characteristic oscillations. An increase of the decay length with minor changes in the period, as compared with the equilibrium data, are observed at Δt = -70 fs. At a later time delay of Δt = 330 fs, an enhancement of the decay length is no longer clearly observed. Pump-induced changes in the period of the oscillations are, however, evident. We chose to display data at these two representative time delays because the pump intensity is substantial at the former time delay (Δt = -70 fs) and negligible at the latter time delay (Δt = 330 fs). The pump-induced changes are clearly revealed in the differential signal, ΔS, which is shown in Figs. 19c, and d. Notably, a $\pi/2$ phase shift of the oscillations in ΔS is observed between the data collected at these two-time delays. These findings indicate a rapid decrease of δq_2 has occurred, which promptly recovers (see Eq's. (22) and (23)). The timescale for recovery of δq_2 is agrees with the pump-probe convolution as we emphasize in Fig. 14.

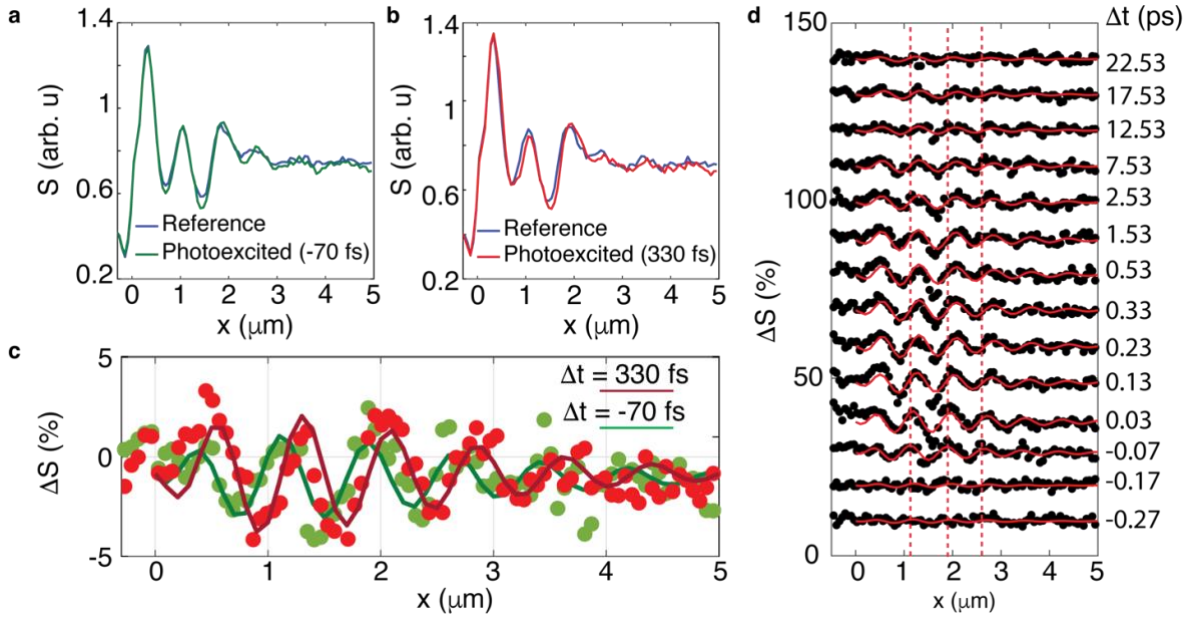

Fig. 19: Pump-probe dynamics of a WSe_2 crystal. The probe energy of E=1.61 eV is used throughout this study while a pump with energy of E=1.56 eV and power of 1.5 mW was applied to photo-excite a 90 nm thick WSe_2 crystal. a and b, Near-field amplitude as a function of real-space position relative to the edge of the WSe_2/SiO_2 interface. A reference trace of the near-field amplitude at equilibrium (blue) is shown. a, The near-field amplitude recorded with photo-excitation near pump probe overlap, while the intensity of the pump is non-zero (Δt=-70 fs), is shown in green. b, identical to panel a, except the photo-excited trace (red) is collected at Δt=330 fs – a time-delay where the probe arrives after the pump intensity has completely decayed. c, Subtracting the reference data from the photo-excited data yields the differential ΔS signal, which is normalized to the mean value of the reference data in the interior of the WSe_2 crystal. d, The differential signal, ΔS, recorded at a series of pump probe time delays are shown with the black dots. Fits constructed using Eq. (21) with the extracted values of δq_1 and δq_2 reported in Fig.'s 14a and 14b are overlaid with the solid red curves. The vertical red dashed lines indicate the locations where maxima are observed in line profiles of the waveguide mode at equilibrium, blue curves displayed in panels a and b. We emphasize that the π/2 phase shift clearly observed in panel c occurs within three hundred femtoseconds of the photo-excitation event. g The curves displayed in panel d are vertically offset for clarity.

3.8 Fluence dependence of the complex wavevector

We proceed to characterize how the photo-induced changes of WSe_2 evolve with the pump power, P, and photon energy of our pumping laser. First, we note that P = 2 mW corresponds to a 5 nJ

energy per pump pulse at our repetition rate of 377 kHz. Using the calculated area of the 9x16 μm^2 elliptical pump beam we estimate the maximum fluence applied to WSe_2, which is approximately 1 mJ/cm^2. The probe energy is fixed at approximately 1.61 eV, which is slightly red detuned from the A-exciton resonance (Table 4). At pump-probe overlap ($\Delta t = 0$) we study the pump-induced changes of the propagation length of the waveguide mode, δq_2. We find that δq_2 follows a linear trend against the pump power, P, with fixed pump-photon energy (solid lines). The measurement is repeated for two values of the detuning, Δ, defined as the energy of the pump relative to the energy of the A-exciton. The magnitude of δq_2 increases as Δ is decreased at constant P. These data collapse onto a single curve when the pump-induced change in wavevector is plotted against P/Δ (Fig. 20). The experimentally measured scaling of the pump power and energy is, therefore, consistent with the trend anticipated for the optical stark effect (*87*).

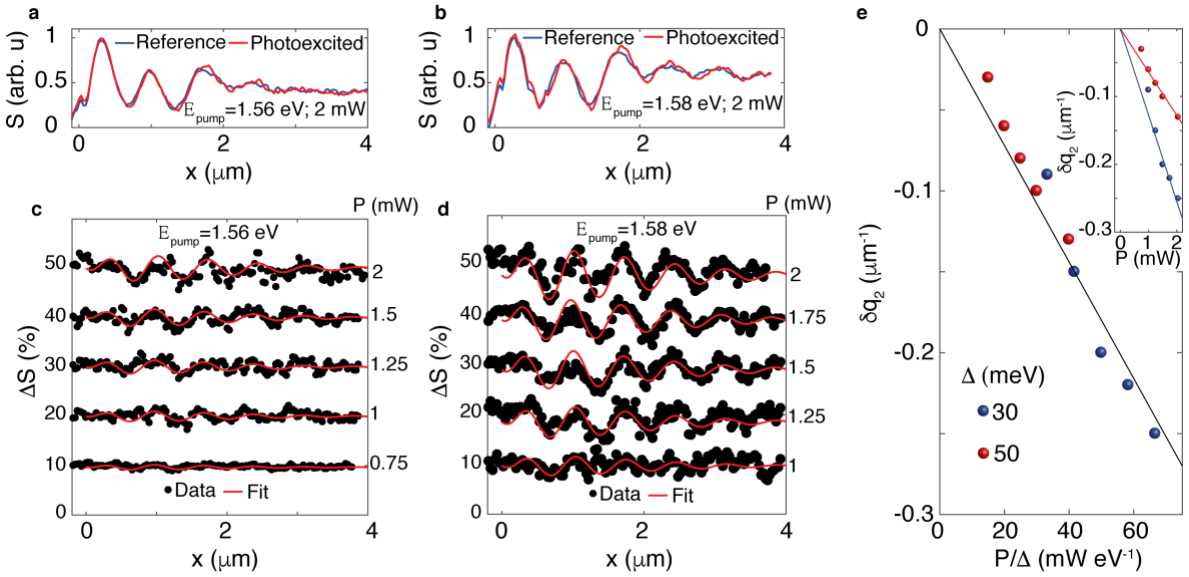

Fig. 20: Fluence dependence of the pump-probe response of WSe_2. The 90 nm thick WSe_2 crystal was investigated with a fixed probe photon energy of E=1.61 eV at pump probe overlap (Δt=0) for this study. The pump pulse has a bandwidth of approximately 15 meV. a and b, Line profiles of the near-field amplitude, S, under photoexcitation (red) are shown together with a reference trace (blue). a, Photo-excited data collected with a pump photon

energy of E_{pump}=1.56 eV and pump power of P=2 mW and b, Photo-excited data collected with a pump photon energy of E_{pump}=1.58 eV and pump power of P=2 mW. c and d, Differential change in the near-field amplitude, ΔS, at a series of pump powers. The black dots are data, while the fits, constructed using Eq. (21) with the extracted values of δq_2 shown in panel e, are overlaid with red solid lines. c, Data were collected with the pump energy of E_{pump}=1.56 eV and d, Data collected with the pump energy of E_{pump}=1.58 eV. The curves shown in panels c and d are vertically offset for clarity. e, The detuning, $\Delta=E_A-E_{pump}$, is defined as the energy difference of the pump relative to the resonant energy of the A-exciton. The extracted values of δq_2 plotted against the rescaled x-axis, defined as power over detuning P/Δ. The extracted values of δq_2 are shown against the applied pump power in the inset.

3.9 Pump-probe spectroscopy and transient nano-imaging

The raw ΔS data for the pump probe spectroscopy measurements are displayed with black dots in Fig. 21. Throughout our experiment the pump conditions were fixed (pump photon energy E=1.56 eV and pump power of 3 mW) while we the probe energy was varied. We highlight several significant features that are observed in the raw data. First, characteristic oscillations in line-profiles of ΔS are observed at all probe frequencies. The amplitude of these oscillations, *A*, is proportionate to the differential change of the wavevector (Chapter 3.3). Second, as the probe energy is increased from 1.46 eV to 1.57 eV substantial increases of the amplitude *A* are observed. The rapid increase of *A* with increasing probe energy is followed by a non-monotonic decrease of *A* when the probe energy is nearly resonant with the A-exciton, around 1.61 eV (see Table 4). Finally, differences between the differential data collected at the two-time delays, Δt = 1 ps and Δt = 0, are most apparent when the probe photon energy is nearly resonant with the A-exciton. The differential change in periodicity, δq_1, reported in Fig. 14e of the main text were extracted from the line-profiles of ΔS using Eq. (21). Our study reveals a clear dispersion anomaly in the vicinity of the A-exciton with significant sub-ps dynamics exposing photo-induced transformations of the A-exciton.

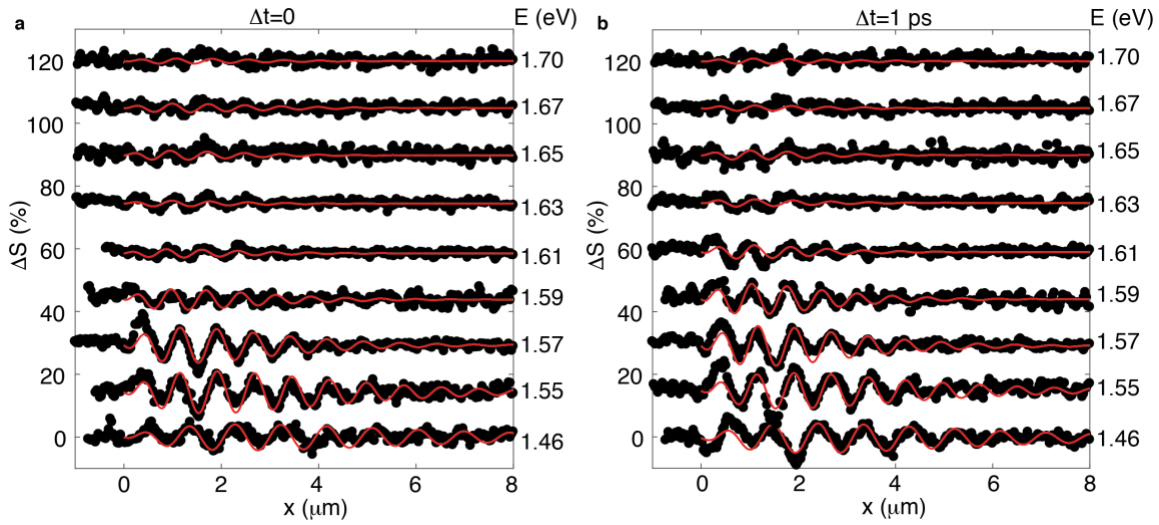

Fig. 21: Non-equilibrium spectroscopy and nano-imaging. These data were collected on a 90 nm slab of WSe_2 photo-excited with a pump energy E=1.56 eV and pump power of 3 mW a, Line profiles of the differential change in near-field amplitude ΔS at a series of probe energies collected at pump-probe overlap (Δt=0). The black dots are data while the fits constructed using Eq. (21) with the extracted values of δq_1 and δq_2 are overlaid in red. b, Identical to panel a, except with a pump probe time delay of Δt = 1 ps. The curves in panels a and b are vertically offset for clarity.

3.10 Modeling the equilibrium dielectric function

In this Section we discuss our model for the dielectric function in equilibrium. The dielectric function of WSe_2, which we used in our calculations, was determined by Li et al., in Ref. (*62*), and is displayed in Fig. 22 (dotted and solid red lines for ε_1 and ε_2 respectively). The salient features of the dielectric function are accurately re-produced with a model based on a series of Lorentzian oscillators (dotted and solid black lines for ε_1 and ε_2 respectively):

$$\varepsilon \cong \varepsilon_{stat} + \sum_{k=1}^{N} \frac{f_k}{(E_k)^2 - E^2 - iE\gamma_k} \qquad (30)$$

The parameters of the Lorentz model are reported in Table 4. The parameters ε_∞=10.5 and the out of plane dielectric function ε_c=11.2 are also used. Our measurements were conducted over a

limited range of probe energies (1.45 eV < E < 1.7 eV). Thus, only the A-exciton is directly observed in the experimental energy window. In the investigated range of energies, a further approximation is valid:

$$\varepsilon \cong \varepsilon^*_{stat} + \frac{f_1}{(E_1)^2 - E^2 - iE\gamma_1} \quad (31)$$

In Eq. 31 the offset of the real part of the dielectric function, ε^*_{stat} stands for the contributions to the static dielectric function from excitons at high energies outside the investigated energy regime. In Fig. 22 we display the dielectric computed with Eqs. (30) and (31). All significant spectral features are accurately represented in the energy scale of 1.45 - 1.8 eV where our investigation of the waveguide mode was performed. In the main text, Eq. (30) was used in our model calculations of the dispersion relationship in equilibrium (Fig. 13d), we remark that the results using Eq. (31) are nearly identical. The simpler single oscillator model Eq. (31) was used in our non-equilibrium analysis (Fig. 14). In the single oscillator model photo-induced changes to high-energy excitons, that are outside the range of energies we investigated, and are not directly measured, are accounted for with the dispersion-less offset of the dielectric function, ε^*_{stat}. Thus, we report only the specific perturbations to the A-exciton, which are directly extracted from our measurements in Table 3.

Table 4: Parameters for the equilibrium dielectric function of WSe_2:

	(k=1)	(k=2)	(k=3)	(k=4)	(k=5)	(k=6)
E_k (eV)	1.612	1.8	2.18	2.6	2.8	3
γ_k (meV)	106.8	251.9	258.4	248	1,264.8	1,248
f_k (eV^2)	1.2046	0.5337	2.081	1.0608	15.4973	20.9515

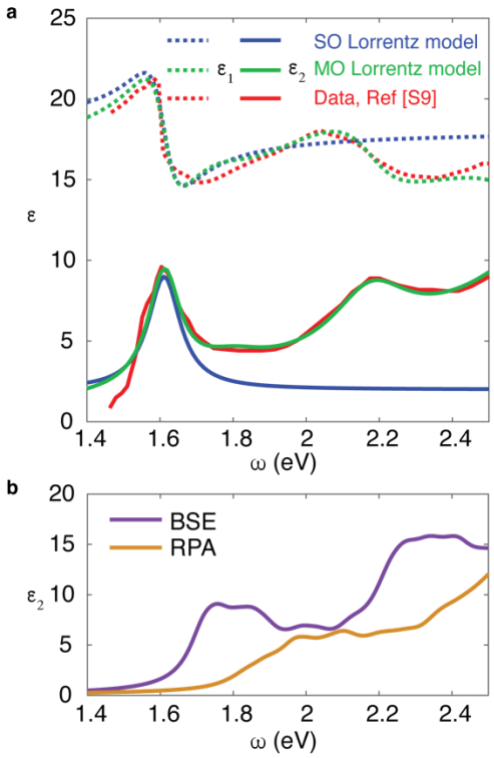

Fig. 22: The equilibrium dielectric function of WSe_2. a, All dashed curves display the real part of the permittivity, ε_1, while all solid curves display the imaginary part of the permittivity, ε_2. The dielectric function from the experimental data of Ref *(62)* are shown with the red curves. Fits using a multi-oscillator (MO) Lorentz model (Eq (30); Table 4), representing multiple excitonic transitions are shown with green curves. Fits with a single oscillator (SO) Lorentz model representing the A-exciton (Eq (31); Table 3 at equilibrium) are shown with blue curves. b, First principles calculations of the dielectric function. The values for ε_2 calculated with the Bethe-Salpeter equation (BSE) are shown in purple while the values for ε_2 calculated within the Random Phase Approximation (RPA) are shown with the orange curve.

The dielectric response of WSe_2 is also obtained from first-principles calculations based on the GPAW code (*109*, *110*) (Fig. 22b). The imaginary part of the dielectric function is obtained from Bethe-Salpeter Equation (BSE) using 2 valence and 2 conduction bands based of the LDA functional, 150 eV cut-off energy for the static screened interaction and a 45x45x3 k-point grid. The BSE results contain spectral weight from excitons in addition to spectral weight from band-to-band transitions. To estimate the spectral weight associated with excitons we also calculated the

dielectric function with the random phase approximation (RPA), which excludes excitonic effects. To obtain the excitonic portion of the dielectric function we first calculate the variation of the imaginary part of the permittivity due to the excitonic effects and then map it to the real part of the permittivity through the Kramers-Kronig relations in formulas:

$$\varepsilon_1^{corr}(\omega) = \varepsilon_1^{RPA}(\omega) + \frac{2}{\pi}\int_0^{\omega_c} d\omega' \frac{\delta\varepsilon_2(\omega)}{\omega'^2-\omega^2} \qquad (32)$$

Where $\delta\varepsilon_2(\omega) = \varepsilon_2^{BSE}(\omega) - \varepsilon_2^{RPA}(\omega)$ was defined. The integration was truncated at the frequency $\omega_c = 2.5\ eV$. The results were insensitive to our exact choice of ω_c indicating the calculation has converged. In terms of the index of refraction, $n_{BSE}(\omega) = \sqrt{\varepsilon_1^{RPA}(\omega) + \varepsilon_1^{corr}(\omega) + i\varepsilon_2^{BSE}(\omega)}$ includes excitonic contributions, while $n_{RPA}(\omega) = \sqrt{\varepsilon_1^{RPA}(\omega) + i\varepsilon_2^{RPA}(\omega)}$ does not. Finally we are able to estimate the contribution to the index of refraction from excitons as $n_{EX}(\omega) = n_{BSE}(\omega) - n_{RPA}(\omega)$ (Fig. 15b of the main text).

It is important to note that our first principles estimates are capable of separating spectral weight associated with band-to-band transitions from the spectral weight associated with excitonic transitions. The latter information, reported in Fig. 15b of the main text, augment our experimental optical data, which are affected by both excitonic and interband effects. Our approach, therefore, allows us to accurately determine the maximum possible change in the index of refraction that can be attained by targeted manipulation of excitons – a fundamental limit to bulk WSe_2 optical modulators.

3.11 Incoherent photo-induced transformations

To investigate plausible roles of free carriers in optical modulation we turn our attention to the mid-infrared spectral range. We observed the appearance of a plasma edge in WSe_2 at the pump-probe time delay Δt=2 ps (Fig. 23). Using a Drude model for the dielectric function:

$$\varepsilon = \varepsilon_{stat} + \Delta\varepsilon \cong \varepsilon_{\infty} - \frac{\omega_p^2}{\omega^2 - i\omega\Gamma} \qquad (33)$$

we employ the lightning rod model (*27, 36, 96*) to calculate the near-field amplitude (solid black curve in Fig. 23). Under nominally similar photoexcitation conditions (pump laser with 820 nm center wavelength, 80 meV bandwidth, 2 mW excitation power, 750 kHz repetition rate) we extract the un-screened plasma-frequency of ω_p = 2,500 cm^{-1}. The scattering rate $\Gamma = 350\ cm^{-1}$ is also extracted. The un-screened plasma frequency is related to the photo-excited free-carrier density as (*111*):

$$n = (0.724\ x\ 10^{21}\ cm^{-3})\left(\frac{m^*}{m_e}\right)\left(\frac{\hbar\omega_p}{8066}\right)^2 \qquad (34)$$

The extracted three dimensional free carrier density is $n=n_{3D}=1.4x10^{19}$ cm^{-3}; in this analysis we assumed the effective mass of the direct band $m^*=0.17\ m_e$ in accord with Ref. (*92*). In terms of the carrier density per atomic layer n_{2D}, we obtained $n_{2D} = n_{3D}\ d_{WSe2} = 1x10^{12}$ cm^{-2} assuming the atomic thickness of WSe_2 layers d_{WSe2}=0.7 nm (*112*). At comparable densities of itinerant carriers drastic changes in the optical spectra of monolayer and bilayer TMD systems have been reported (*85, 86, 90, 101*). These transformations were attributed to the onset of a Mott transition where the

electron-hole plasma screens the Coulomb interaction that binds excitons together causing the excitons to dissociate (*113*). Estimates for the critical Mott density have been reported in a wide range from $3x10^{12}$ cm^{-2} (*90*) to $1x10^{14}$ cm^{-2} (*86*) in mono and bilayer TMD systems. Bulk three dimensional models predict a lower Mott-threshold, with a lower bound of approximately $3x10^{18}$ cm^{-3} (*114*). In our experimental data we observe a 7% bleaching of the A-exciton, which is consistent with other experimental spectra taken near, but not significantly above, the Mott threshold (*85, 86, 90*). Finally, we remark that as one approaches the Mott-transition the binding energy of excitons decreases. An interesting follow up study, suggested by our results, would be to investigate how the optical Stark effect is impacted as the binding energy of the A-exciton approaches zero in TMDs. The suggested study could be carried out by monitoring the optical Stark shift as the carrier density is tuned to, and beyond, the Mott threshold with photo-excitation (*86, 90*) or electrostatic gating (*85*).

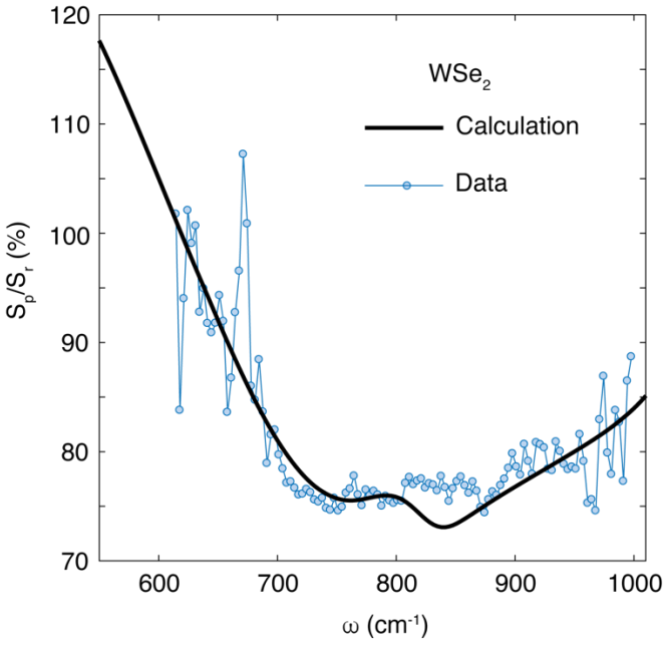

Fig. 23: Mid-IR spectroscopy. Near-field amplitude spectra recorded with the pump on, S_p, were normalized to spectra obtained with the pump off, S_r. The pump conditions are

described in the text of Chapter 3.11. Fits using the Lightning Rod Model (*36*) were used to produce the solid line as described in the text of Chapter 3.11.

Following an abrupt increase of the periodicity of the waveguide mode, which is described by δq_1, the decay process is well described by Auger equation:

$$\frac{d(\delta q_1)}{dt} = -k_q \delta q_1^2 \qquad (35)$$

Our motivation for using Eq. 35 is purely phenomenological. The fit presented as the blue line in Fig 14b of the main text yields k_q=1.2x10^{13} (10^{-5} cm)/s. The constant pre-factor k_q can be regarded the decay rate of an annihilation processes, which may include decay by collision with defect or trap states and exciton-exciton annihilation (*115, 116*).

3.12 Imaging waveguide modes with pulsed laser sources

In our experiments, we employ broadband pulsed lasers. To account for the finite bandwidth of the laser pulse we consider a wave-packet:

$$E(r,t) = \int dk\ \mathrm{M}(k) \exp\left[i(kx - \omega t)\right] \qquad (36)$$

In free space, M(k) is simply the momenta of the incident radiation. When the sharp tip of the AFM probe is illuminated by an infrared beam described by Eq. (36) the wave packet will be modified:

$$E_p(r,t) = \int dk\ B(k) \exp\left[i(kx - \omega t)\right] \qquad (37)$$

The sharp apex of the AFM probe confines radiation to a length scale, a, equal to the radius of the probe (~20 nm). In turn the momentum response function of the AFM probe, R(k), facilitates access to momenta outside of the light-cone, a well-known feature that is described in previous works (*36*). The properties of the sample, together with the response of the AFM probe, determine the distribution of momenta in the tip/sample system, B(k). In the present case, our WSe_2 samples support propagating TM_0 modes with momenta that are outside of the free-space light cone but inside the light-cone of WSe_2 (see Chapter 3.6). The broadband wave-packet launches multiple TM_0 waveguide modes simultaneously, which can interfere. Inserting a gaussian wave-packet $B(k) = v_g \exp\left[-\frac{(k-k_0)^2}{(\Delta k/v_g)^2}\right]$ into Eq. (37) we recognize general, qualitative, features that are expected when broadband light sources are employed. In the latter expression, k_0, is the momenta at the center of the wave-packet, Δk, characterizes the distribution of momenta within the wave-packet and, v_g, is the group velocity of the propagating mode. The length scale where reduced propagation length should be observed from these interference effects is given by $v_g/\Delta k$.

By varying the bandwidth of our probe channel, we experimentally investigate the theory described above. In Fig. 24 we display line-profiles of the near-field amplitude as a function of the distance to the edge of the WSe_2 flake. A bandpass filter with full-width at half maximum of about 15 meV (= 4 THz) was inserted to the beamline to narrow the bandwidth of the probe beam before it was delivered to the AFM microscope. With the latter, narrowband, illumination we recorded the red curve. When the bandpass filter was removed and the full bandwidth of the probe channel, 80 meV (= 20 THz) was employed we measured the line profile displayed with the black curve in Fig. 24. It is apparent that the observed propagation length of the waveguide mode is dependent on the bandwidth of the probe beam. The quantity $v_g/\Delta k$ defines the length scale where destructive

interference within the wave-packet dominates the propagation length. In the former case of narrowband, 15 meV, illumination $v_g/\Delta k$=25 μm and the bandwidth of the wavepacket has a negligible impact on the experimentally measured line-profile within the 12 μm field of view we investigated. In the latter case of the broadband, 80 meV, illumination the anticipated propagation length is $v_g/\Delta k$=5 μm, which is in agreement with our observations.

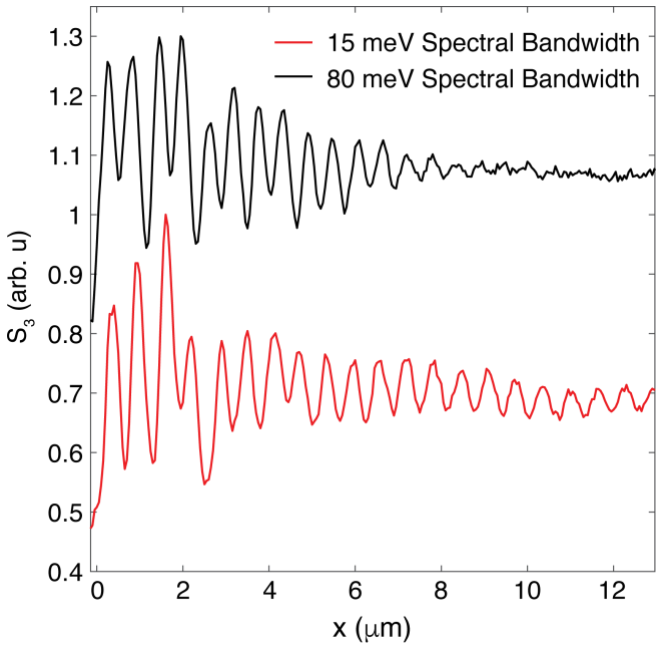

Fig. 24: Line profiles of the near-field amplitude obtained on a 210 nm thick WS_2 crystal on an SiO_2 substrate. A probe channel with energy of E = 1.46 eV was used in this study. The black curve was recorded with the full spectral bandwidth of the laser, approximately 80 meV. The red curve was recorded with a spectrally filtered 15 meV bandwidth probe beam. The curves were vertically offset for clarity.

3.13 Pump-probe dynamics of WS_2

We observed substantial photo-induced optical modulation in a closely related dichalcogenide material WS_2 (Fig. 25); the gross features of these latter pump-probe data are similar to our observations for WSe_2. At a fixed probe energy E=1.46 eV we recorded line-profiles of the near-field amplitude for a 210 nm thick WS_2 flake on the SiO_2 substrate. The oscillations that are

observed in the line-profiles are dominated by the TM_0 waveguide mode, which propagates within WS_2. We repeated the measurement with photoexcitation at a fixed pump energy, E_p=1.88 eV at a series of pump powers (Fig. 25a). We observed that the periodicity of the waveguide mode was significantly increased on photoexcitation. Pump induced changes of the decay length are, however, insignificant and remain below our detection limits at all pump powers. The pump-induced change in the periodicity, described by δq_1, increases linearly with the applied pump power with no apparent sign of saturation (Fig. 25b). At the highest pump power of 1.5 mW, δq_1 = -0.018 (10^5 cm^{-1}) is obtained, which corresponds to Δn = -0.23 (Chapter 3.5). We emphasize that the relationship between δq_1 and Δn was determined with the aid of Eq. (28). The latter relationship depends on multiple parameters, which importantly include the sample thickness and equilibrium dielectric function of the sample.

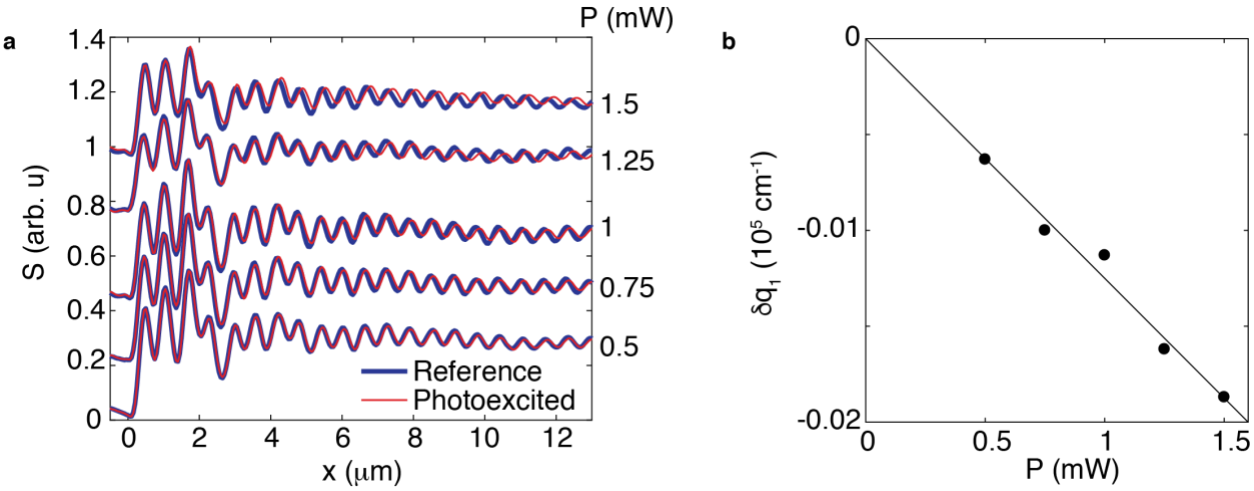

Fig. 25: Power dependence of the photo-excitation response for WS_2. A WS_2 crystal with thickness of 210 nm was investigated with a 1.46 eV probe pulse under photo-excitation with a 1.88 eV pump pulse at the time delay Δt = 0.1 ps in this study. a, Line-profiles of the near-field amplitude under photoexcitation (red) are shown together with a reference (blue) at a series of pump powers. The curves are vertically offset for clarity. b, The pump-induced change in the periodicity of the waveguide mode as a function of the pump power.

References

1. D. N. Basov, R. D. Averitt, D. van der Marel, M. Dressel, K. Haule, Electrodynamics of correlated electron materials. *Reviews of Modern Physics* **83**, 471-541 (2011).

2. R. D. Averitt, A. J. Taylor, Ultrafast optical and far-infrared quasiparticle dynamics in correlated electron materials. *Journal of Physics: Condensed Matter* **14**, R1357-R1390 (2002).

3. A. H. Zewail, Femtochemistry: Atomic-Scale Dynamics of the Chemical Bond. *The Journal of Physical Chemistry A* **104**, 5660-5694 (2000).

4. T. Kampfrath, K. Tanaka, K. A. Nelson, Resonant and nonresonant control over matter and light by intense terahertz transients. *Nature Photonics* **7**, 680-690 (2013).

5. J. Orenstein, Ultrafast spectroscopy of quantum materials. *Physics Today* **65**, 44-50 (2012).

6. M. Liu *et al.*, Terahertz-field-induced insulator-to-metal transition in vanadium dioxide metamaterial. *Nature* **487**, 345-348 (2012).

7. D. J. Hilton *et al.*, Enhanced Photosusceptibility near Tc for the Light-Induced Insulator-to-Metal Phase Transition in Vanadium Dioxide. *Physical Review Letters* **99**, 226401 (2007).

8. V. R. Morrison *et al.*, A photoinduced metal-like phase of monoclinic VO2 revealed by ultrafast electron diffraction. *Science* **346**, 445-448 (2014).

9. A. X. Gray *et al.*, Ultrafast terahertz field control of electronic and structural interactions in vanadium dioxide. *Physical Review B* **98**, 045104 (2018).

10. Z. He, A. J. Millis, Photoinduced phase transitions in narrow-gap Mott insulators: The case of VO2. *Physical Review B* **93**, 115126 (2016).

11. D. Fausti *et al.*, Light-Induced Superconductivity in a Stripe-Ordered Cuprate. *Science* **331**, 189-191 (2011).

12. J. Zhang *et al.*, Cooperative photoinduced metastable phase control in strained manganite films. *Nature Materials* **15**, 956-960 (2016).

13. E. Dagotto, Complexity in Strongly Correlated Electronic Systems. *Science* **309**, 257-262 (2005).

14. E. Dagotto, T. Hotta, A. Moreo, Colossal magnetoresistant materials: the key role of phase separation. *Physics Reports* **344**, 1-153 (2001).

15. G. Campi *et al.*, Inhomogeneity of charge-density-wave order and quenched disorder in a high-Tc superconductor. *Nature* **525**, 359-362 (2015).

16. F. Chen *et al.*, Electronic Identification of the Parental Phases and Mesoscopic Phase Separation of KxFe2-ySe2 Superconductors. *Physical Review X* **1**, 021020 (2011).

17. M. M. Qazilbash *et al.*, Mott Transition in VO2 Revealed by Infrared Spectroscopy and Nano-Imaging. *Science* **318**, 1750-1753 (2007).

18. A. S. McLeod *et al.*, Nanotextured phase coexistence in the correlated insulator V2O3. *Nature Physics* **13**, 80-86 (2017).

19. M. K. Liu *et al.*, Anisotropic Electronic State via Spontaneous Phase Separation in Strained Vanadium Dioxide Films. *Physical Review Letters* **111**, 096602 (2013).

20. Y. Zhu *et al.*, Mesoscopic structural phase progression in photo-excited VO2 revealed by time-resolved x-ray diffraction microscopy. *Scientific Reports* **6**, 21999 (2016).

21. M. Liu, A. J. Sternbach, D. N. Basov, Nanoscale electrodynamics of strongly correlated quantum materials. *Reports on Progress in Physics* **80**, 014501 (2016).

22. L. Stojchevska *et al.*, Ultrafast Switching to a Stable Hidden Quantum State in an Electronic Crystal. *Science* **344**, 177-180 (2014).

23. T. L. Cocker *et al.*, An ultrafast terahertz scanning tunnelling microscope. *Nature Photonics* **7**, 620-625 (2013).

24. J. M. Atkin, S. Berweger, A. C. Jones, M. B. Raschke, Nano-optical imaging and spectroscopy of order, phases, and domains in complex solids. *Advances in Physics* **61**, 745-842 (2012).

25. M. Wagner *et al.*, Ultrafast Dynamics of Surface Plasmons in InAs by Time-Resolved Infrared Nanospectroscopy. *Nano Letters* **14**, 4529-4534 (2014).

26. G. X. Ni *et al.*, Ultrafast optical switching of infrared plasmon polaritons in high-mobility graphene. *Nature Photonics* **10**, 244-247 (2016).

27. M. Wagner *et al.*, Ultrafast and Nanoscale Plasmonic Phenomena in Exfoliated Graphene Revealed by Infrared Pump–Probe Nanoscopy. *Nano Letters* **14**, 894-900 (2014).

28. M. Eisele *et al.*, Ultrafast multi-terahertz nano-spectroscopy with sub-cycle temporal resolution. *Nature Photonics* **8**, 841 (2014).

29. M. A. Huber *et al.*, Femtosecond photo-switching of interface polaritons in black phosphorus heterostructures. *Nature Nanotechnology* **12**, 207-211 (2017).

30. M. A. Huber *et al.*, Ultrafast Mid-Infrared Nanoscopy of Strained Vanadium Dioxide Nanobeams. *Nano Letters* **16**, 1421-1427 (2016).

31. S. A. Dönges *et al.*, Ultrafast Nanoimaging of the Photoinduced Phase Transition Dynamics in VO2. *Nano Letters* **16**, 3029-3035 (2016).

32. F. Kuschewski *et al.*, Optical nanoscopy of transient states in condensed matter. *Scientific Reports* **5**, 12582 (2015).

33. H. Wang, L. Wang, X. G. Xu, Scattering-type scanning near-field optical microscopy with low-repetition-rate pulsed light source through phase-domain sampling. *Nature Communications* **7**, 13212 (2016).

34. N. Ocelic, A. Huber, R. Hillenbrand, Pseudoheterodyne detection for background-free near-field spectroscopy. *Applied Physics Letters* **89**, 101124 (2006).

35. A. J. Sternbach *et al.*, Artifact free time resolved near-field spectroscopy. *Opt. Express* **25**, 28589-28611 (2017).

36. A. S. McLeod *et al.*, Model for quantitative tip-enhanced spectroscopy and the extraction of nanoscale-resolved optical constants. *Physical Review B* **90**, 085136 (2014).

37. R. Hillenbrand, F. Keilmann, Complex Optical Constants on a Subwavelength Scale. *Physical Review Letters* **85**, 3029-3032 (2000).

38. S. Berweger *et al.*, Nano-Chemical Infrared Imaging of Membrane Proteins in Lipid Bilayers. *Journal of the American Chemical Society* **135**, 18292-18295 (2013).

39. B. Knoll, F. Keilmann, Enhanced dielectric contrast in scattering-type scanning near-field optical microscopy. *Optics Communications* **182**, 321-328 (2000).

40. D. Richards, A. Zayats, F. Keilmann, R. Hillenbrand, Near-field microscopy by elastic light scattering from a tip. *Philosophical Transactions of the Royal Society of London. Series A: Mathematical, Physical and Engineering Sciences* **362**, 787-805 (2004).

41. K. Reimann, R. P. Smith, A. M. Weiner, T. Elsaesser, M. Woerner, Direct field-resolved detection of terahertz transients with amplitudes of megavolts per centimeter. *Optics Letters* **28**, 471-473 (2003).

42. M. Liu *et al.*, Phase transition in bulk single crystals and thin films of VO2 by nanoscale infrared spectroscopy and imaging. *Physical Review B* **91**, 245155 (2015).

43. J. H. Park *et al.*, Measurement of a solid-state triple point at the metal–insulator transition in VO2. *Nature* **500**, 431-434 (2013).

44. A. C. Jones, S. Berweger, J. Wei, D. Cobden, M. B. Raschke, Nano-optical Investigations of the Metal−Insulator Phase Behavior of Individual VO2 Microcrystals. *Nano Letters* **10**, 1574-1581 (2010).

45. S. Liu *et al.*, Random Field Driven Spatial Complexity at the Mott Transition in VO2. *Physical Review Letters* **116**, 036401 (2016).

46. B. T. O'Callahan *et al.*, Inhomogeneity of the ultrafast insulator-to-metal transition dynamics of VO2. *Nature Communications* **6**, 6849 (2015).

47. O. Nájera, M. Civelli, V. Dobrosavljević, M. J. Rozenberg, Resolving the VO2 controversy: Mott mechanism dominates the insulator-to-metal transition. *Physical Review B* **95**, 035113 (2017).

48. Z. Fei *et al.*, Gate-tuning of graphene plasmons revealed by infrared nano-imaging. *Nature* **487**, 82-85 (2012).

49. S. Lysenko, A. Rúa, V. Vikhnin, F. Fernández, H. Liu, Insulator-to-metal phase transition and recovery processes in VO2 thin films after femtosecond laser excitation. *Physical Review B* **76**, 035104 (2007).

50. M. M. Qazilbash *et al.*, Infrared spectroscopy and nano-imaging of the insulator-to-metal transition in vanadium dioxide. *Physical Review B* **79**, 075107 (2009).

51. A. Pashkin *et al.*, Ultrafast insulator-metal phase transition in VO2 studied by multiterahertz spectroscopy. *Physical Review B* **83**, 195120 (2011).

52. K. Moon *et al.*, Subsurface Nanoimaging by Broadband Terahertz Pulse Near-Field Microscopy. *Nano Letters* **15**, 549-552 (2015).

53. H. T. Stinson *et al.*, Infrared nanospectroscopy and imaging of collective superfluid excitations in anisotropic superconductors. *Physical Review B* **90**, 014502 (2014).

54. J.-S. Wu, D. N. Basov, M. M. Fogler, Topological insulators are tunable waveguides for hyperbolic polaritons. *Physical Review B* **92**, 205430 (2015).

55. W. K. Hiebert, A. Stankiewicz, M. R. Freeman, Direct Observation of Magnetic Relaxation in a Small Permalloy Disk by Time-Resolved Scanning Kerr Microscopy. *Physical Review Letters* **79**, 1134-1137 (1997).

56. T. Kampfrath *et al.*, Coherent terahertz control of antiferromagnetic spin waves. *Nature Photonics* **5**, 31-34 (2011).

57. I. Katayama *et al.*, Ferroelectric Soft Mode in a SrTiO3 Thin Film Impulsively Driven to the Anharmonic Regime Using Intense Picosecond Terahertz Pulses. *Physical Review Letters* **108**, 097401 (2012).

58. S. Fleischer, R. W. Field, K. A. Nelson, Commensurate Two-Quantum Coherences Induced by Time-Delayed THz Fields. *Physical Review Letters* **109**, 123603 (2012).

59. J. A. Gerber, S. Berweger, B. T. O'Callahan, M. B. Raschke, Phase-Resolved Surface Plasmon Interferometry of Graphene. *Physical Review Letters* **113**, 055502 (2014).

60. D. N. Basov, M. M. Fogler, F. J. García de Abajo, Polaritons in van der Waals materials. *Science* **354**, aag1992 (2016).

61. S. Dai *et al.*, Tunable Phonon Polaritons in Atomically Thin van der Waals Crystals of Boron Nitride. *Science* **343**, 1125-1129 (2014).

62. Y. Li *et al.*, Measurement of the optical dielectric function of monolayer transition-metal dichalcogenides: MoS2, MoSe2, WS2, and WSe2. *Physical Review B* **90**, 205422 (2014).

63. F. Hu *et al.*, Imaging exciton–polariton transport in MoSe2 waveguides. *Nature Photonics* **11**, 356 (2017).

64. A. M. Dubrovkin *et al.*, Visible Range Plasmonic Modes on Topological Insulator Nanostructures. *Advanced Optical Materials* **5**, 1600768 (2017).

65. D. Nicoletti, A. Cavalleri, Nonlinear light–matter interaction at terahertz frequencies. *Adv. Opt. Photon.* **8**, 401-464 (2016).

66. A. Cavalleri, T. Dekorsy, H. H. W. Chong, J. C. Kieffer, R. W. Schoenlein, Evidence for a structurally-driven insulator-to-metal transition in VO2: A view from the ultrafast timescale. *Physical Review B* **70**, 161102 (2004).

67. R. Singla *et al.*, THz-Frequency Modulation of the Hubbard U in an Organic Mott Insulator. *Physical Review Letters* **115**, 187401 (2015).

68. V. Kravtsov, R. Ulbricht, J. M. Atkin, M. B. Raschke, Plasmonic nanofocused four-wave mixing for femtosecond near-field imaging. *Nature Nanotechnology* **11**, 459-464 (2016).

69. D. K. Gramotnev, S. I. Bozhevolnyi, Nanofocusing of electromagnetic radiation. *Nature Photonics* **8**, 13-22 (2014).

70. D. N. Basov, R. D. Averitt, D. Hsieh, Towards properties on demand in quantum materials. *Nature Materials* **16**, 1077 (2017).

71. J. M. Atkin *et al.*, Strain and temperature dependence of the insulating phases of VO2 near the metal-insulator transition. *Physical Review B* **85**, 020101 (2012).

72. W. W. Peng *et al.*, Insulator–metal transition of VO2 ultrathin films on silicon: evidence for an electronic origin by infrared spectroscopy. *Journal of Physics: Condensed Matter* **25**, 445402 (2013).

73. T. J. Huffman *et al.*, Anisotropic infrared response of vanadium dioxide microcrystals. *Physical Review B* **87**, 115121 (2013).

74. N. B. Aetukuri *et al.*, Control of the metal–insulator transition in vanadium dioxide by modifying orbital occupancy. *Nature Physics* **9**, 661-666 (2013).

75. M. R. Otto *et al.*, How optical excitation controls the structure and properties of vanadium dioxide. *Proceedings of the National Academy of Sciences* **116**, 450-455 (2019).

76. J. D. Budai *et al.*, Metallization of vanadium dioxide driven by large phonon entropy. *Nature* **515**, 535-539 (2014).

77. C. N. Berglund, H. J. Guggenheim, Electronic Properties of VO2 near the Semiconductor-Metal Transition. *Physical Review* **185**, 1022-1033 (1969).

78. C. Kübler *et al.*, Coherent Structural Dynamics and Electronic Correlations during an Ultrafast Insulator-to-Metal Phase Transition in VO2. *Physical Review Letters* **99**, 116401 (2007).

79. D. Lee *et al.*, Isostructural metal-insulator transition in VO2. *Science* **362**, 1037-1040 (2018).

80. J. Laverock *et al.*, Direct Observation of Decoupled Structural and Electronic Transitions and an Ambient Pressure Monocliniclike Metallic Phase of VO2. *Physical Review Letters* **113**, 216402 (2014).

81. M. G. Evans, M. Polanyi, Some applications of the transition state method to the calculation of reaction velocities, especially in solution. *Transactions of the Faraday Society* **31**, 875-894 (1935).

82. D. Hu *et al.*, Probing optical anisotropy of nanometer-thin van der waals microcrystals by near-field imaging. *Nature Communications* **8**, 1471 (2017).

83. M. Mrejen, L. Yadgarov, A. Levanon, H. Suchowski, Transient exciton-polariton dynamics in WSe2 by ultrafast near-field imaging. *Science Advances* **5**, eaat9618 (2019).

84. T. Low *et al.*, Polaritons in layered two-dimensional materials. *Nature Materials* **16**, 182-194 (2017).

85. A. Chernikov *et al.*, Electrical Tuning of Exciton Binding Energies in Monolayer WS2. *Physical Review Letters* **115**, 126802 (2015).

86. A. Chernikov, C. Ruppert, H. M. Hill, A. F. Rigosi, T. F. Heinz, Population inversion and giant bandgap renormalization in atomically thin WS2 layers. *Nature Photonics* **9**, 466 (2015).

87. E. J. Sie *et al.*, Valley-selective optical Stark effect in monolayer WS2. *Nature Materials* **14**, 290 (2014).

88. Z. Ye, D. Sun, T. F. Heinz, Optical manipulation of valley pseudospin. *Nature Physics* **13**, 26 (2016).

89. C.-K. Yong *et al.*, Biexcitonic optical Stark effects in monolayer molybdenum diselenide. *Nature Physics* **14**, 1092-1096 (2018).

90. J. Wang *et al.*, Optical generation of high carrier densities in 2D semiconductor heterobilayers. *Science Advances* **5**, eaax0145 (2019).

91. Z. Sun, A. Martinez, F. Wang, Optical modulators with 2D layered materials. *Nature Photonics* **10**, 227 (2016).

92. S. Latini, E. Ronca, U. De Giovannini, H. Hübener, A. Rubio, Cavity Control of Excitons in Two-Dimensional Materials. *Nano Letters* **19**, 3473-3479 (2019).

93. G. Hu *et al.*, Coherent steering of nonlinear chiral valley photons with a synthetic Au–WS2 metasurface. *Nature Photonics* **13**, 467-472 (2019).

94. K. F. Mak, J. Shan, Photonics and optoelectronics of 2D semiconductor transition metal dichalcogenides. *Nature Photonics* **10**, 216 (2016).

95. G. Wang *et al.*, Colloquium: Excitons in atomically thin transition metal dichalcogenides. *Reviews of Modern Physics* **90**, 021001 (2018).

96. A. Charnukha *et al.*, Ultrafast nonlocal collective dynamics of Kane plasmon-polaritons in a narrow-gap semiconductor. *Science Advances* **5**, eaau9956 (2019).

97. D. Hu *et al.*, Tunable Modal Birefringence in a Low-Loss Van Der Waals Waveguide. *Advanced Materials* **31**, 1807788 (2019).

98. W. Ma *et al.*, In-plane anisotropic and ultra-low-loss polaritons in a natural van der Waals crystal. *Nature* **562**, 557-562 (2018).

99. U. D. Giovannini, H. Hübener, Floquet analysis of excitations in materials. *Journal of Physics: Materials* **3**, 012001 (2019).

100. M. Claassen, C. Jia, B. Moritz, T. P. Devereaux, All-optical materials design of chiral edge modes in transition-metal dichalcogenides. *Nature Communications* **7**, 13074 (2016).

101. A. Steinhoff, M. Rösner, F. Jahnke, T. O. Wehling, C. Gies, Influence of Excited Carriers on the Optical and Electronic Properties of MoS2. *Nano Letters* **14**, 3743-3748 (2014).

102. B. Chakraborty *et al.*, Control of Strong Light–Matter Interaction in Monolayer WS2 through Electric Field Gating. *Nano Letters* **18**, 6455-6460 (2018).

103. A. Raja *et al.*, Enhancement of Exciton–Phonon Scattering from Monolayer to Bilayer WS2. *Nano Letters* **18**, 6135-6143 (2018).

104. R. Soref, B. Bennett, Electrooptical effects in silicon. *IEEE Journal of Quantum Electronics* **23**, 123-129 (1987).

105. G. Scuri *et al.*, Large Excitonic Reflectivity of Monolayer MoSe2 Encapsulated in Hexagonal Boron Nitride. *Physical Review Letters* **120**, 037402 (2018).

106. D. Edelberg *et al.*, Approaching the Intrinsic Limit in Transition Metal Diselenides via Point Defect Control. *Nano Letters* **19**, 4371-4379 (2019).

107. S. Dai *et al.*, Efficiency of Launching Highly Confined Polaritons by Infrared Light Incident on a Hyperbolic Material. *Nano Letters* **17**, 5285-5290 (2017).

108. E. E. Narimanov, A. V. Kildishev, Naturally hyperbolic. *Nature Photonics* **9**, 214 (2015).

109. J. Enkovaara *et al.*, Electronic structure calculations with GPAW: a real-space implementation of the projector augmented-wave method. *Journal of Physics: Condensed Matter* **22**, 253202 (2010).

110. J. J. Mortensen, L. B. Hansen, K. W. Jacobsen, Real-space grid implementation of the projector augmented wave method. *Physical Review B* **71**, 035109 (2005).

111. D. C. Johnston, The puzzle of high temperature superconductivity in layered iron pnictides and chalcogenides. *Advances in Physics* **59**, 803-1061 (2010).

112. P. Steinleitner *et al.*, Direct Observation of Ultrafast Exciton Formation in a Monolayer of WSe2. *Nano Letters* **17**, 1455-1460 (2017).

113. A. P. Schlaus *et al.*, How lasing happens in CsPbBr3 perovskite nanowires. *Nature Communications* **10**, 265 (2019).

114. M. A. M. Versteegh, T. Kuis, H. T. C. Stoof, J. I. Dijkhuis, Ultrafast screening and carrier dynamics in ZnO: Theory and experiment. *Physical Review B* **84**, 035207 (2011).

115. D. Sun *et al.*, Observation of Rapid Exciton–Exciton Annihilation in Monolayer Molybdenum Disulfide. *Nano Letters* **14**, 5625-5629 (2014).

116. H. Wang, C. Zhang, F. Rana, Ultrafast Dynamics of Defect-Assisted Electron–Hole Recombination in Monolayer MoS2. *Nano Letters* **15**, 339-345 (2015).

117. N. Ocelic, Quantitative Near-field Phono-polariton Spectroscopy. PhD Thesis, Technische Universität, München (2007).

Appendix A

The nature of aperture-free near-field techniques provides an enhancement to the near-field contribution of the measured signal. As such it cannot be expected that the measured signal will be completely free from background radiation. It must, instead, be decided if the ratio between near-field and background information merits confidence that an arbitrary pHD signal is actually related to the material's response in the near-field. In the case of time resolved studies, experimental observables constitute a small fraction ($\Delta R/R = O(10^{-2}\text{-}10^{-6})$) of the overall signal. While the demand for adequate sensitivity in a pump probe experiment raises the bar for requirements on the signal-to-noise ratios of the near-field signal, the stringent requirement for adequate background suppression cannot be sacrificed to achieve a higher dynamic range. This section is intended to evaluate the possibility for time-resolved near-field signals to compete with time-resolved features from the background contribution.

In the inset of Fig. 5 we show a schematic layout intended to illustrate the origin of background contributions. The focal plane of the off-axis parabolic mirror, which is used to focus and collect light from the tip-sample interaction, can be brought above (black) or below (green) the plane of the sample (red). In each of these cases, radiation that interacts with the AFM probe can be back-scattered into the detector. As the AFM probe is lifted by a height ΔH, the backscattered radiation experiences a phase shift of magnitude $\delta = 2\pi\Delta H cos\vartheta/\lambda$, where ϑ is the angle of incidence and λ is the wavelength of probe radiation. Therefore, throughout the tip-tapping cycle, the phase of radiation that is backscattered directly from the probe is modulated as $\psi_{bg} = \delta cos\Omega t$, with the tip-tapping frequency of Ω. The background electric field is given by:

$$E_{BG} = |E|e^{i\delta cos\Omega t} = |E|\sum_{m=-\infty}^{\infty} J_m(\delta)\, e^{i\frac{m\pi}{2}} e^{im\Omega t} \quad (38)$$

Where we used the Jacobi-Anger expansion in the second half of Eq. (38). Eq. (38) shows immediately that background radiation will have a finite value at all harmonics of the tip tapping frequency. The background electric-field can, therefore, couple to the reference arm's electric field and produce a finite pHD signal in high harmonics of the tip-tapping frequency. While this source of background is an issue for static s-SNOM experiments, the background contribution in Eq. (38) is not affected by the pump-probe probe time delay, Δt_{ps} in Fig. 2(g). This background source is, therefore, eliminated in Tr-pHD experiments.

It is also possible to measure a finite pHD signal from a background contribution that depends on the reflection coefficient of the sample. One situation in which this is possible is shown by the green beam in the inset of Fig. 5 where the focal plane of incident radiation is brought below the plane of the sample. In this case light that is reflected off of the sample, with reflection coefficient r_{scatt}, scatters off of the AFM probe shaft and is brought to the detector. By symmetry the phase shift experience by this reflected wave will be $\psi_{bg} = \text{-}\delta cos\Omega t$ throughout the tip-tapping cycle. The background electric field in this case is given by:

$$E_{BG} = |E| r_{Scatt}(\Delta t_{ps}) e^{-i\delta cos\Omega t} = |E| \sum_{m=-\infty}^{\infty} r_{Scatt}(\Delta t_{ps}) J_m(-\delta)\, e^{i\frac{m\pi}{2}} e^{im\Omega t} \qquad (39)$$

In this case, it is possible to measure a finite Tr-pHD signal from the background contribution, since r_{Scatt} is a function of the pump-probe time delay, Δt_{ps}. We note, however, that the background contribution is strictly diffraction limited and cannot vary on a deeply sub-wavelength length scale in real space.

In the case that the incident probe radiation is brought into the focal plane of the sample (red in the inset of Fig. 5), both aforementioned background sources contribute. Together with the bona-fide scattered field associated with near-field interactions, the total electric field at high harmonics of the tip tapping frequency is given by:

$$E_m = E_{NF}+E_{BG} = \left|E_{NF}(x,\Delta t_{ps})\right|e^{i\psi_{NF}(x,\Delta t_{ps})} + |E_{BG}|[J_m(\delta) + r_{Scatt}(\Delta t_{ps})J_m(-\delta)]e^{i\frac{m\pi}{2}}$$

(40)

Where we have explicitly noted dependencies on the local spatial coordinate, x, and the pump-probe time delay Δt_{ps}. The electric field in Eq. (40), which includes both near-field and background contributions is mixed with the reference arm to generate the pHD signal in a realistic experimental setting.

In static s-SNOM experiments, a sufficiently high harmonic is taken such that the background contribution becomes negligible with respect to the near-field signal. Starting from Eq. (40) we note that the tapping amplitude, ΔH, is chosen such that $\delta = 2\pi\Delta H cos\vartheta/\lambda \ll 1$ to Taylor expand the Bessel functions to first order about zero. This gives us the total scattered electric field at the m_{th} harmonic in a typical experimental setting (*117*):

$$E_m \cong \left|E_{NF}(x,\Delta t_{ps})\right|e^{i\psi_{NF}(x,\Delta t_{ps})} + \left|E_{BG}(\Delta t_{ps})\right|\frac{(i\delta)^m}{m!}(1+(-1)^m r_{Scatt}(\Delta t_{ps})) \qquad (41)$$

It can be observed from Eq. (41) that the magnitude of the background term in a pHD signal will scale as $(\Delta H/\lambda)_m$. As the extent of the local evanescent wave that generates the near-field signal is approximately the tip-radius, ~20 nm, a tapping amplitude of ΔH ~ 60 nm is sufficient to provide a large modulation of the near-field signal at an arbitrary wavelength. However, with a constant tapping amplitude constant, the degree to which the background radiation is suppressed by the tapping motion is strongly wavelength dependent. We show the background contribution for harmonics S_1 (Red) - S_6 (Purple) as a function of wavelength in Fig. 5. The magnitude of near-field signal as a series of increasing harmonic order was calculated at a wavelength of 10 μm using the lightning rod model (*36*) and is shown by the dots on the right-hand side of the plot, with the identical color scale as the background contribution. We note that, the ratio of near-field signal to background signal should be nearly independent of wavelength, provided that the tip remains a

good electrical conductor in the frequency range of the probe and that the wavelength remains much larger than the tip radius. The magnitude of the near-field signal relative to the background was normalized by using the experimentally measured ratio for the second harmonic at the probe wavelength of 1.5 μm, used in this work. This is the ratio of s_2^{pHD} measured in when the AFM probe is in contact with the sample to the value of s_2^{pHD} when the sample is fully retracted. The ratio of background to near-field contributions will, however, depend critically on the focused spot size as well as geometric factors so there may be significant error in the absolute comparison.

Appendix B

Despite apparent complication of using a periodic train of ultrashort laser pulses, the demodulation protocols can operate in nearly identical fashion to the well-established methods commonly used in static nano-imaging. The sidebands of the laser repetition rate, of the tip-tapping, and reference arm frequencies $m\Omega +/-\mathrm{NM} +/-$ pF are proportionate to the near-field electric field as we showed in Ref. (*35*) and discussed in Chapter 1.

In the case that pulsed lasers are employed in nano-imaging and nano-spectroscopy the detector bandwidth is of critical importance. In the case that the detector bandwidth $f_D \ll F$ only the p = 0 harmonic of the lasers repetition rate is detected. The extraction pHD signal is then identical to the case that a C.W. laser is employed. If a detector with a bandwidth $f_D \gtrsim F$ is used, boxcar integration may be performed to over one cycle of the laser's repetition rate, allowing the experimentalist to make use of information contained in all of the observable harmonics of the laser pulse train. The boxcar output has maximum bandwidth $f_B = F/2 >> m\Omega +/-\mathrm{NM}$ where the last inequality is necessary to avoid aliasing of extracted near-field optical signal.

Appendix C

Consider the intensity that is backscattered by an AFM probe, which is tapped at a frequency Ω, Fig. 1(a). The electric field phasor that is backscattered from the tip and/or sample can be accurately described by a Fourier series expansion in harmonics of the tip-tapping frequency:

$$\tilde{E}_s = \left|\tilde{E}_0\right|e^{i\psi_0} + \left|\tilde{E}_1\right|e^{i(\Omega t+\psi_1)} + \left|\tilde{E}_2\right|e^{i(2\Omega t+\psi_2)} + \cdots = \sum_m \left|\tilde{E}_m\right|e^{i(m\Omega t+\psi_n)} \quad (42)$$

where $\left|\tilde{E}_m\right|$ (with m = 0, 1, 2, etc.) is the magnitude of the electric field at the mth harmonic of the tip-tapping frequency and ψ_m is the optical phase of scattered light encoded in the mth harmonic of the tip-tapping frequency. The leading term term, $\tilde{E}_0$, is largely unrelated to the tip-sample near field interaction so that this term may be accurately described as the background electric-field phasor, $\tilde{E}_{BG}$ (Chapter 1.2). With increasing harmonic order the background contribution decays rapidly while the near-field contribution does not (Appendix A, Fig. 5). Thus, when sufficiently high harmonics of the tip-tapping frequency, $\tilde{E}_m$, are accessed by demodulation of the detected intensity only terms that are proportionate to electric field phasor scattered by the near-field interaction, $\tilde{E}_{NF}$, contribute to the signal.

Apart from a select few detection methods, such as electro optic sampling and photo-conductive antenna detection, modern detectors measure the intensity of light rather than the electric field, as emphasized in Eq. (1). Since $\tilde{E}_{BG}$ dominates the high-harmonic component of signal by orders of magnitude the leading order term in the mth harmonic is:

$$u_{sHD} \propto 2\left|\tilde{E}_{BG}\right|\left|\tilde{E}_{NF}\right|cos(\Delta\psi_{BG}) \quad (43)$$

To simplify the equations, we have introduced the phase difference $\Delta\psi_{BG} = \psi_{BG} - \psi_{NF}$. In a pump-probe experiment one is exploring the difference between signals collected from the

sample's pump induced states, at a time Δt_{ps} following the pump pulse, and its static states. We, therefore, need to add an additional term to Eq. (43) to form the Tr-sHD signal:

$$\Delta u_{sHD}(x,\Delta t_{ps}) \propto \left|\tilde{E}_{BG}(\Delta t_{ps})\right|\left|\tilde{E}_{NF}(x,\Delta t_{ps})\right| cos\left(\Delta\psi_{BG}(x,\Delta t_{ps})\right)$$

$$-\left|\tilde{E}_{BG}(\Delta t_{ps}<0)\right|\left|\tilde{E}_{NF}(x,\Delta t_{ps}<0)\right| cos\left(\Delta\psi_{BG}(x,\Delta t_{ps}<0)\right) \quad (44)$$

It can immediately be appreciated that eight independent variables contribute to the Tr-sHD measurement; four of which are from the background electric field phasor. The presence of four BG variables, which all contain strictly diffraction limited information in Eq. (44) is discomforting. A cursory analysis of Eq. (44) reveals that the most troubling feature is an sHD experiment is not directly sensitive to the near-field phase. The coupled response between the, potentially, time dependent far-field phase and spatially dependent near-field phase can generate fictitious pump-induced features on the sub wavelength scale, Fig. 1(b). We note that this problem is not relevant if there are no pump-induced changes to the far-field phase.

For completeness, we consider the case that a reference arm is added, Figs. 2(b), and (e). In this case one measures:

$$\Delta u_{HD}(x,\Delta t_{ps}) \propto \left(\left|\tilde{E}_{BG}(\Delta t_{ps})\right| cos(\Delta\psi_{BG}) + \left|\tilde{E}_{ref}\right| cos\left(\Delta\psi_{ref}\right)\right)\left|\tilde{E}_{NF}(x,\Delta t_{ps})\right| -$$

$$\left(\left|\tilde{E}_{BG}(\Delta t_{ps}<0)\right| cos(\Delta\psi_{BG}) + \left|\tilde{E}_{ref}\right| cos\left(\Delta\psi_{ref}\right)\right)\left|\tilde{E}_{NF}(x,\Delta t_{ps}<0)\right| \quad (45)$$

Where we introduced, $\Delta\psi_{ref} = \psi_{ref} - \psi_{NF}$. We emphasize that the radiation in the reference arm does not interact with the sample, thus the $|\tilde{E}_{ref}|$ and $|\psi_{ref}|$ are properties that cannot depend on the temporal or spatial coordinates of the sample. Therefore, results generated with Tr-HD signal will be free of multiplicative background artifacts if the amplitude of the reference field is much stronger than that of the background field, $\left|\tilde{E}_{ref}\right| \gg |\tilde{E}_{BG}|$ (*40*). A quantitative estimate is also required to determine the possible contribution of background radiation in results generated with

the Tr-HD method. In the case of Tr-HD typical values for the magnitude electric field from the reference arm relative to that of the background yield substantial suppression of multiplicative backgrounds (*35*). In fact, if the amplitude of the reference arm is modulated in the Tr-HD scheme, complete suppression of the multiplicative background can be achieved as described in Refs. (*37, 38*). When amplitude modulated Tr-HD is combined with two-phase detection (*39, 48*) the results are free from the influence of multiplicative background radiation and can be used to extract the amplitude and phase of the near-field signal, although this has not yet been demonstrated with pulsed laser sources and has similar complications from the bandwidth of the pulsed source to those addressed in Chapter 1.5. In Tr-pHD detection modulating the phase of the reference arm, likewise, provides complete immunity from multiplicative background artifacts (*35*). Other techniques, such as EoS or detection with a photo-conductive antenna detect the electric field directly yielding results that are also immune from the multiplicative background contribution and are compatible with rapid nano-imaging in the mid-infrared and terahertz frequency ranges (*28, 52*). Thus, there is a whole arsenal of nano-optics methods that offer means and ways for multiplicative background radiation suppression.

We proceed to form an extreme, but plausible estimate of artificial signals that are permissible when Tr-sHD is used in the scenario schematically illustrated in Fig. 26. In our scenario every pixel within the field of view possesses a near-field phase of ψ_r=0 (red) except a single pixel, which has a near-field phase of ψ_b=0.86 (blue). We remark that the latter phase contrast between the red and blue pixels is approximately the near-infrared phase contrast of strain-relieved "buckled" regions relative to compressively strained regions within the VO_2/TiO_2 film studied in chapter 1. At the time $\Delta t = 0$ a photo-excitation event drives a change of the near-field phase at all red pixels given by the model function $\psi_r(\Delta t_{ps}) = (0.04\, rad)\theta(\Delta t_{ps})$ exp $(-\frac{\Delta t_{ps}}{\tau})$.

We furthermore insist that the background phase is approximately the average observed in the near-field and thus $\psi_{BG}(\Delta t_{ps}) \cong \psi_r(\Delta t_{ps})$ as nearly all locations have phase ψ_r in our model. For simplicity the magnitude of all electric fields are set to 1 and taken to be time-independent. Using Eq. (44) we compute the time-dependent change of the near-field optical signal that is detected with the self-homodyne method, Fig. 26. The anticipated results that are anticipated with various detection methods, summarized in Table 5, demonstrate that time-resolved signal that bears little to no relationship to the genuine optical constants provided are anticipated with Tr-sHD method. We therefore conclude, that the BG contribution to data gathered with Tr-sHD detection could produce the response shown in Fig. 1(b) and can generate observable artifacts in a general setting.

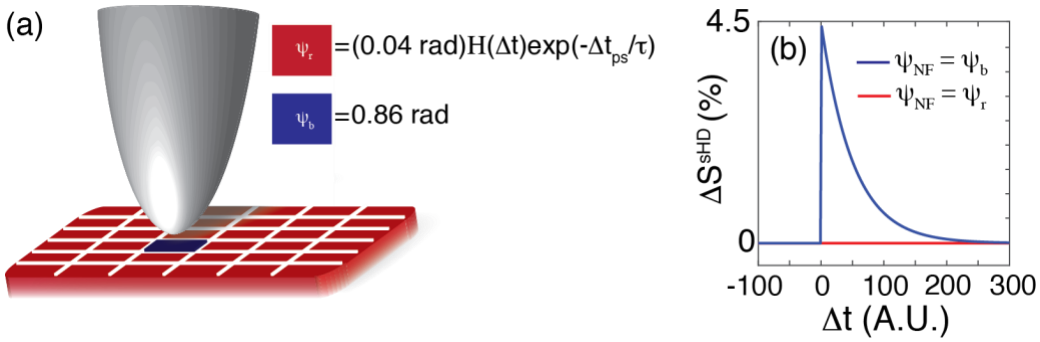

Fig. 26: Model calculations for the Tr-sHD signal. a) Schematic showing the AFM probe on a pixelated surface. The dominant area of the sample is state indicated with red, and is assigned the near-field phase ψ_r. A single pixel is blue, and is assigned the near-field phase ψ_b. The time-dependent numeric values of these phases are shown in the inset. b) Transient response of the sHD signal at a red pixel (red) and blue pixel (blue).

Table 5. Model calculations for the Tr-sHD signal. The results of Tr-sHD were calculated using Eq. 44. The values displayed for Tr-pHD can be obtained using Eq. 7-10 for a narrow bandwidth pulsed laser.

	Actual	Tr-sHD	Tr-pHD

ΔS (red)	0	0	0
$\Delta\psi$ (red)	0.04 rad	N/A	0.04 rad
ΔS (blue)	0	4.5%	0
$\Delta\psi$ (blue)	0	N/A	0